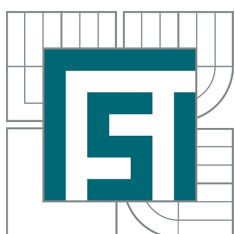


VYSOKÉ UČENÍ TECHNICKÉ V BRNĚ
BRNO UNIVERSITY OF TECHNOLOGY



FAKULTA STROJNÍHO INŽENÝRSTVÍ
ÚSTAV FYZIKÁLNÍHO INŽENÝRSTVÍ
FACULTY OF MECHANICAL ENGINEERING
INSTITUTE OF PHYSICAL ENGINEERING

INTERAKCE KOVOVÝCH NANOČÁSTIC A RYCHLÝCH ELEKTRONŮ

INTERACTION OF METALLIC NANOPARTICLES AND FAST ELECTRONS

DIPLOMOVÁ PRÁCE
MASTER'S THESIS

AUTOR PRÁCE
AUTHOR

Bc. ANDREA KONEČNÁ

VEDOUCÍ PRÁCE
SUPERVISOR

prof. RNDr. PETR DUB, CSc.

Vysoké učení technické v Brně, Fakulta strojního inženýrství

Ústav fyzikálního inženýrství
Akademický rok: 2014/2015

ZADÁNÍ DIPLOMOVÉ PRÁCE

student(ka): Bc. Andrea Konečná

který/která studuje v **magisterském navazujícím studijním programu**

obor: **Fyzikální inženýrství a nanotechnologie (3901T043)**

Ředitel ústavu Vám v souladu se zákonem č.111/1998 o vysokých školách a se Studijním a zkušebním řádem VUT v Brně určuje následující téma diplomové práce:

Interakce kovových nanočástic a rychlých elektronů

v anglickém jazyce:

Interaction of metallic nanoparticles and fast electrons

Stručná charakteristika problematiky úkolu:

Kovové nanočástice, na nichž lze excitovat lokalizované povrchové plazmony, jsou v dnešní době intenzivně studovány kvůli jejich možnému využití, např. v biodetekci, spektroskopických metodách nebo optických zařízeních. Prvním krokem předcházejícím možným aplikacím je výroba a charakterizace plazmonických struktur. V této oblasti je velmi důležitým nástrojem rastrovací prozařovací elektronový mikroskop, pomocí kterého lze získat detailní informace o vzorku zahrnující optické excitace s velkým prostorovým rozlišením, nebo jej můžeme využít pro přesnou manipulaci s nanočásticemi. Teoretické modely (buď analytické, nebo numerické) a popis těchto jevů jsou stěžejní pro hlubší porozumění problematice.

Cíle diplomové práce:

1. Rešeršní studie.
2. Popis silového působení rychlých elektronů na kovové nanočástice.
3. Numerické výpočty spekter energiových ztrát elektronů.

Seznam odborné literatury:

1. Jackson, J. D. Classical Electrodynamics, 3rd ed. John Wiley & Sons, New York, 1998.
2. García de Abajo, F. J. Relativistic energy loss and induced photon emission in the interaction of a dielectric sphere with an external electron beam. *Physical Review B* 59, 4 (1999), 3095–3107.
3. García de Abajo, F. J. Optical excitations in electron microscopy. *Reviews of Modern Physics* 82, 1 (2010), 209–275.
4. García de Abajo, F. J. Momentum transfer to small particles by passing electron beams. *Physical Review B* 70 (2004), 115422.

Vedoucí diplomové práce: prof. RNDr. Petr Dub, CSc.

Termín odevzdání diplomové práce je stanoven časovým plánem akademického roku 2014/2015.

V Brně, dne 20.11.2014

L.S.

prof. RNDr. Tomáš Šikola, CSc.
Ředitel ústavu

doc. Ing. Jaroslav Katolický, Ph.D.
Děkan fakulty

Abstrakt

Rastrovací prozařovací elektronová mikroskopie je jednou ze základních technik vhodnou nejen pro zobrazování nanostruktur, ale může být také použita pro různé druhy spektroskopí a, jak bylo nedávno ukázáno, i pro nanomanipulaci. V této práci se zabýváme interakcí rychlých elektronů a kovových sférických nanočástic, konkrétně hliníkových a zlatých nanokuliček. Nejprve prezentujeme jak analytické, tak numerické výpočty spekter energiových ztrát elektronů a jejich analýzu pro různé parametry. Hlavní část práce je věnována teoretickým výpočtům sil působících na nanokuličku díky elektronu prolétávajícímu v její těsné blízkosti. Na základě našich nových výsledků odhalujících časový vývoj mechanické síly také navrhujeme možný mechanismus stojící za rozpohybováním nanočástic v elektronovém mikroskopu.

Summary

Scanning transmission electron microscopy is one of the essential techniques suitable not only for imaging of nanostructures, but also for various kinds of spectroscopy and, as it was recently demonstrated, nanomanipulation. In this thesis, we deal with an interaction of fast electrons and metallic spherical nanoparticles, specifically aluminium and gold nanospheres. First, we present both analytical and numerical calculations of electron energy loss spectra and their analysis for different parameters. The main part of the thesis is devoted to theoretical calculations of forces acting on the nanosphere due to the electron passing in its close proximity. Based on our novel results revealing a time evolution of the mechanical force, we also propose a possible mechanism responsible for the nanoparticle movement in electron microscopes.

Klíčová slova

Spektroskopie energiových ztrát elektronů, kovové nanočástice, plasmonika.

Keywords

Electron energy loss spectroscopy, metallic nanoparticles, plasmonics.

KONEČNÁ, A. *Interaction of metallic nanoparticles and fast electrons*. Brno: Vysoké učení technické v Brně, Fakulta strojního inženýrství, 2015. 87 s. Vedoucí diplomové práce prof. RNDr. Petr Dub, CSc..

Hereby I declare that I have created this work autonomously under a scientific supervision of Prof. RNDr. Petr Dub, CSc. All sources, references and literature used or excerpted during the elaboration of this work are properly cited and listed in the complete reference.

Andrea Konečná

Acknowledgement

I would like to thank my supervisor Prof. Petr Dub for his inspiring comments, discussions not only about physics and for corrections of this thesis.

I would not probably work on such an interesting topic, which the interaction of the electrons and metallic particles definitely is, without Prof. Javier Aizpurua. I want to thank Javier for the possibility of spending my Erasmus stay in his research group in San Sebastián, for introducing me to the topic and for his valuable suggestions.

I am very grateful for the opportunity to collaborate on this project with Dr. Maureen Lagos and Prof. Philip Batson. I would like to thank Maureen for our discussions and for giving me tips how to speed-up my calculations.

Tomáš Neuman never leaves me alone with my thoughts and always provides me with excellent comments. He also deserves my words of thanks for proof-reading of this thesis. I must thank my family and Filip for love, patience and support in my studies.

Andrea Konečná

Contents

Introduction	3
1 Electromagnetic field	5
1.1 Maxwell's equations and material relationships	5
1.2 Maxwell stress tensor	7
1.3 Vector and scalar potentials	9
2 Dielectric response of metallic nanoparticles	11
2.1 Classical dielectric models	11
2.2 Non-classical response of metallic nanoparticles	15
3 Electron energy loss spectroscopy	19
3.1 Field of a moving electron	20
3.2 Classical dielectric formalism	22
3.3 Bulk losses	23
3.4 Surface modes	24
3.5 Localized modes	24
3.6 Boundary element method	26
4 Interaction of spherical particles with an electron beam	29
4.1 Multipole expansion of the field produced by fast electron	29
4.2 Multipole expansion of the induced fields outside the sphere	32
4.3 Total fields inside the sphere	34
4.4 Electron energy loss probability	37
5 Momentum transfer to a metallic sphere	43
5.1 Momentum transfer in the frequency domain	44
5.1.1 Aluminium nanosphere	48
5.1.2 Gold nanosphere	51
5.2 Calculation of the force in the time domain	53
5.2.1 Aluminium nanosphere	55
5.2.2 Gold nanosphere	63
6 Conclusions	67
Appendix A: Fourier transform	69
Appendix B: Atomic units	71
Appendix C: Multipole expansion	73
Bibliography	81

CONTENTS

Introduction

The field of electron microscopy has passed a long way since its invention in early 1930s. In the beginnings, electron microscopes were capable of magnifying samples in the order of hundred times, but nowadays, thanks to development of better electron sources, optics, detectors and vacuum devices [1, 2], they can reach even resolution of single atoms. Together with these improvements, application of many techniques employing electron microscopy has started, such as electron energy loss spectroscopy (EELS).

The first measurements by means of EELS were introduced by Ruthemann in 1941 [3] and by Hillier and Baker in 1944 [4]. EELS has been widely used for identifying the energies of various types of excitations in materials and in 1950s, it helped to discover the existence of surface plasmons, which were detected in thin metallic foils together with the already known bulk plasma oscillations. A theoretical explanation was given by Ritchie [5] in 1957 and the name of the excitation comes from Stern and Ferrell [6]. These and other works in the last years led to development of a new field of physics, nowadays called plasmonics.

Although it seems plasmonics is something completely new, people used plasmon-based devices, without knowing the origin of the effects. Naturally, it was soon discovered that the plasmon excitations are present not only in the form of the bulk electron gas oscillations or the oscillations of electron plasma confined to extended metal surfaces, but also as localized particle resonances. When we illuminate tiny particles, e.g. in colloidal solutions, we can see them shining in different colours related to their resonant frequencies which depend on size, shape or material. This effect was employed by glass-blowers, who produced beautiful colourful glass (Lycurgus cup can serve as a nice example [7]).

This phenomenon is now being intensively studied due to many potential applications derived from the confinement and enhancement of the fields associated with localized surface plasmons. The sensitivity of the localized plasmon frequency to the dielectric properties of the surrounding medium is exploited in development of plasmonic biosensors. The strong electromagnetic field enhancement close to surfaces of the plasmonic particles also strongly magnifies interaction of samples with probing radiation, which is employed e.g. in surface enhanced Raman spectroscopy (SERS), surface enhanced infrared scattering or absorption SEIRS(A). Great efforts are also invested in using such particles in near-field optical devices and in controlling optical signals [8].

For the development of new applications, it is necessary to be able to tailor particles and structures of properties on demand. A variety of manufacturing and analytical methods for plasmonic structures operating at different spectral ranges and serving different purposes has been developed. Although invented 70 years ago, EELS still remains one of the most fundamental methods to explore resonant modes of the nanoparticles [9, 10]. Due to the evanescent nature of the fields produced by the moving electrons, EELS can reveal not only bright, but also the so called dark modes (which are not excitable by light due to selection rules) [11], therefore provides very detailed information about the particles and the nanostructures.

The fields around tiny particles, generated by swift electrons, can also induce forces acting on them. This phenomenon causes the nanoparticle motion and can be employed as a tool for manipulation at nanoscale [12–14]. Because of the high resolution of electron microscopes, these "electron tweezers" can be much more accurate than conventional techniques used for this purpose [15]. However, recent investigation shows that the nature

of the forces is not only attractive with respect to the beam as one would expect intuitively, but in some cases there can exist repulsion between the electron beam and the metallic nanoparticle [12, 16, 17]. Deeper understanding of that ambiguity of the force orientation is a key to a successful application of the manipulation technique in practise. Hence, the aim of this work is to dissect the ambiguous nature of the forces acting on the plasmonic nanoparticles.

In the first chapter, we introduce fundamental quantities related to the electromagnetic field and provide a basis for the following parts of the thesis. As we will deal with the metallic nanoparticles, in the second chapter we describe their dielectric response to an external electromagnetic excitation and briefly discuss when non-classical regime of the electron-particle interaction becomes important.

The third chapter is focused on the electron energy loss spectroscopy from the theoretical point of view. We show the formalism and basic analytical solutions for the EEL probability for some canonical geometries. In the end of the chapter the most common numerical approach used for EELS calculations of various structures – a boundary element method – will be briefly introduced.

In the fourth chapter we deal with an approach leading to analytical expressions for the fields induced by electrons near and inside the spherical particles [18]. We compare these analytical results with numerical simulations and also use them for calculations of EEL probability corresponding to aluminium and gold nanospheres. The following chapter is devoted to the main goal of the thesis, evaluation of the momentum transfer to the nanospheres. We first present results in the frequency domain and then show completely new calculations of momentum transfer performed in the time domain, revealing the dynamics of the interaction between the nanoparticle and the swift electron.

We hope that our findings will help to improve the understanding of the fundamental principles leading to nanoparticle motion observed in scanning transmission electron microscopes (STEM) [12]. Unraveling of the complex dynamics induced by fast electron beams is crucial for possible future application of STEM as a powerful tool for manipulation of matter at the nanoscale.

1. Electromagnetic field

Since the theoretical work, which will be presented in this thesis, relies mainly on the classical electrodynamics framework, we start with introduction of related quantities and fundamental equations of electrodynamics. SI units are used throughout this chapter.

1.1. Maxwell's equations and material relationships

Electromagnetic fields can be expressed by means of four fundamental equations named after the Scottish mathematical physicist James Clerk Maxwell. The form of these equations we use nowadays was introduced by Oliver Heaviside.

The first equation is also called Gauss's law and it connects the electric displacement \mathbf{D} with the density of the free charge ρ_F [19, 20]:

$$\nabla \cdot \mathbf{D} = \rho_F, \quad \iint_{\partial V} \mathbf{D} \cdot d\mathbf{S} = \iiint_V \rho_F dV. \quad (1.1)$$

An equivalent equation, which holds for the magnetic field induction \mathbf{B} , establishes that there exists no magnetic monopole in nature:

$$\nabla \cdot \mathbf{B} = 0, \quad \iint_{\partial V} \mathbf{B} \cdot d\mathbf{S} = 0. \quad (1.2)$$

The third equation is Faraday's law of induction which shows that the change of the magnetic induction \mathbf{B} with time gives rise to an electric field \mathbf{E}

$$\nabla \times \mathbf{E} = -\frac{\partial \mathbf{B}}{\partial t}, \quad \oint_S \mathbf{E} \cdot d\mathbf{s} = -\frac{d}{dt} \iint_S \mathbf{B} \cdot d\mathbf{S}, \quad (1.3)$$

and similarly Ampère's law with Maxwell's displacement current shows that we can expect magnetic field \mathbf{H} in the presence of free current density \mathbf{J}_F or when the electric displacement \mathbf{D} is changing with time:

$$\nabla \times \mathbf{H} = \mathbf{J}_F + \frac{\partial \mathbf{D}}{\partial t}, \quad \oint_S \mathbf{H} \cdot d\mathbf{s} = \iint_S \mathbf{J}_F \cdot d\mathbf{S} + \frac{d}{dt} \iint_S \mathbf{D} \cdot d\mathbf{S}. \quad (1.4)$$

In the equations (1.1) – (1.4) we presented the "macroscopic" set of Maxwell's equations and showed both the differential and the integral forms which are suitable for different purposes. The equivalence of these two forms can be derived from the divergence theorem [Eqs. (1.1) and (1.2)] and Stokes' theorem [Eqs. (1.3) and (1.4)].

The relationship between \mathbf{E} and \mathbf{D} is defined by

$$\mathbf{D} = \epsilon_0 \mathbf{E} + \mathbf{P}, \quad (1.5)$$

where \mathbf{P} is the polarization of the material and ϵ_0 is the electric permittivity of vacuum, while for vectors related to magnetic fields

$$\mathbf{H} = \frac{\mathbf{B}}{\mu_0} - \mathbf{M} \quad (1.6)$$

1.1. MAXWELL'S EQUATIONS AND MATERIAL RELATIONSHIPS

holds. μ_0 is the magnetic permeability of vacuum and \mathbf{M} the magnetization of material. Both \mathbf{P} and \mathbf{M} are commonly defined as an average dipole moment per unit volume, electric in the case of the polarization or magnetic when we refer to the magnetization.

If we write the total charge density (ρ) as the sum of the free (ρ_F) and the bounded (ρ_B) charges and the current density (\mathbf{J}) as the sum of the free (\mathbf{J}_F) and the bounded (\mathbf{J}_B) current densities, respectively,

$$\rho = \rho_F + \rho_B, \quad (1.7) \quad \mathbf{J} = \mathbf{J}_F + \mathbf{J}_B \quad (1.8)$$

and plug Eqs. (1.5), (1.6), (1.7) and (1.8) into Eqs. (1.1) and (1.4), we obtain the following relationships for the bound charge and current densities:

$$\nabla \cdot \mathbf{P} = -\rho_B, \quad (1.9) \quad \mathbf{J}_B = \nabla \times \mathbf{M} + \frac{\partial \mathbf{P}}{\partial t}. \quad (1.10)$$

From the macroscopic point of view, the free charges and currents can be attributed to external sources, whereas the bounded charges and currents are confined to the dielectric bodies. The differential forms of the equations (1.1) and (1.4) can be rewritten with use of the total charges and currents as

$$\nabla \cdot \mathbf{E} = \frac{\rho}{\varepsilon_0}, \quad (1.11) \quad \nabla \times \mathbf{B} = \mu_0 \mathbf{J} + \varepsilon_0 \mu_0 \frac{\partial \mathbf{E}}{\partial t}. \quad (1.12)$$

The relation between the vectors \mathbf{E} and \mathbf{D} or \mathbf{B} and \mathbf{H} is usually expressed by means of electric permittivity $\boldsymbol{\varepsilon} = \varepsilon_0 \boldsymbol{\varepsilon}_r$ and magnetic permeability $\boldsymbol{\mu} = \mu_0 \boldsymbol{\mu}_r$, which can generally be tensors. If we assume a linear response of translationally symmetric media, we can write these relations with use of convolution:

$$\mathbf{D}(\mathbf{r}, t) = \iiint \boldsymbol{\varepsilon}(\mathbf{r} - \mathbf{r}', t - t') \mathbf{E}(\mathbf{r}', t') dt' d\mathbf{r}', \quad (1.13)$$

$$\mathbf{B}(\mathbf{r}, t) = \iiint \boldsymbol{\mu}(\mathbf{r} - \mathbf{r}', t - t') \mathbf{H}(\mathbf{r}', t') dt' d\mathbf{r}', \quad (1.14)$$

where we integrate over the whole space and at all times. Another relation between the current density and the electric field should also be mentioned

$$\mathbf{J}(\mathbf{r}, t) = \iiint \boldsymbol{\sigma}(\mathbf{r} - \mathbf{r}', t - t') \mathbf{E}(\mathbf{r}', t') dt' d\mathbf{r}', \quad (1.15)$$

where $\boldsymbol{\sigma}$ is a conductivity tensor. We can notice that Eqs. (1.13), (1.14) and (1.15) cover spatial and temporal non-locality. However, in many situations, the spatial dispersion can be neglected and the local response approximation is used.

Response of the material is often transformed in (\mathbf{k}, ω) space with use of the Fourier transform (see related part in Appendix A). Exploiting the properties of convolution (A7) and its definition (A8), Eqs. (1.13), (1.14) and (1.15) can be rewritten as:

$$\mathbf{D}(\mathbf{k}, \omega) = \boldsymbol{\varepsilon}(\mathbf{k}, \omega) \mathbf{E}(\mathbf{k}, \omega), \quad (1.16)$$

$$\mathcal{B}(\mathbf{k}, \omega) = \boldsymbol{\mu}(\mathbf{k}, \omega) \mathcal{H}(\mathbf{k}, \omega), \quad (1.17)$$

$$\mathcal{J}(\mathbf{k}, \omega) = \boldsymbol{\sigma}(\mathbf{k}, \omega) \mathcal{E}(\mathbf{k}, \omega). \quad (1.18)$$

1.2. Maxwell stress tensor

Apart from Maxwell's equations, another fundamental law has to be introduced. If a particle with charge q is moving with velocity \mathbf{v} in an electromagnetic field, we will observe a mechanical force, named after Hendrik Antoon Lorentz [19, 21],

$$\mathbf{F}_L = q(\mathbf{E} + \mathbf{v} \times \mathbf{B}) \quad (1.19)$$

acting on it. This relationship can be rewritten as the volume integral of the Lorentz force density:

$$\begin{aligned} \frac{d\mathbf{p}_{\text{mech}}}{dt} &= \iiint_V (\rho \mathbf{E} + \mathbf{J} \times \mathbf{B}) dV \\ &= \iiint_V \varepsilon_0 \left[\mathbf{E}(\nabla \cdot \mathbf{E}) + \mathbf{B} \times \frac{\partial \mathbf{E}}{\partial t} - c^2 \mathbf{B} \times (\nabla \times \mathbf{B}) \right] dV, \end{aligned} \quad (1.20)$$

where we substituted the relationships for ρ and \mathbf{J} from Eqs. (1.11) and (1.12). \mathbf{p}_{mech} is the mechanical momentum and $c = 1/\sqrt{\varepsilon_0 \mu_0}$ is the speed of light in vacuum. To continue with the treatment of the integrand in Eq. (1.20), we add there $c^2 \mathbf{B}(\nabla \cdot \mathbf{B})$ which is equal to zero [see Eq. (1.2)] and does not change the value of the integrand. Moreover, after applying the equality

$$\mathbf{B} \times \frac{\partial \mathbf{E}}{\partial t} = -\frac{\partial}{\partial t}(\mathbf{E} \times \mathbf{B}) + \mathbf{E} \times \frac{\partial \mathbf{B}}{\partial t} = -\frac{\partial}{\partial t}(\mathbf{E} \times \mathbf{B}) - \mathbf{E} \times (\nabla \times \mathbf{E}), \quad (1.21)$$

and assuming non-magnetic material, where $\mathbf{B} = \mu_0 \mathbf{H}$, we obtain

$$\begin{aligned} \frac{d\mathbf{p}_{\text{mech}}}{dt} &= -\frac{d}{dt} \varepsilon_0 \mu_0 \iiint_V (\mathbf{E} \times \mathbf{H}) dV \\ &\quad + \varepsilon_0 \iiint_V [\mathbf{E}(\nabla \cdot \mathbf{E}) - \mathbf{E} \times (\nabla \times \mathbf{E}) + c^2 \mathbf{B}(\nabla \cdot \mathbf{B}) - c^2 \mathbf{B} \times (\nabla \times \mathbf{B})] dV. \end{aligned} \quad (1.22)$$

In the first term on the right-hand side, we can recognize the Poynting's vector defined as $\mathbf{S} = \mathbf{E} \times \mathbf{H}$. Hence, Eq. (1.22) becomes

$$\begin{aligned} \frac{d\mathbf{p}_{\text{mech}}}{dt} + \frac{1}{c^2} \frac{d}{dt} \iiint_V \mathbf{S} dV \\ &= \varepsilon_0 \iiint_V [\mathbf{E}(\nabla \cdot \mathbf{E}) - \mathbf{E} \times (\nabla \times \mathbf{E}) + c^2 \mathbf{B}(\nabla \cdot \mathbf{B}) - c^2 \mathbf{B} \times (\nabla \times \mathbf{B})] dV. \end{aligned} \quad (1.23)$$

1.2. MAXWELL STRESS TENSOR

It shows up that, with use of the divergence theorem, it is possible to transform the volume integral on the right hand side into a surface integral. As the integrand of the volume integral is vectorial, the surface integral needs to contain the second rank tensor. This dyadic is called the Maxwell stress tensor and is defined as [19, 22]:

$$\overleftrightarrow{\mathbf{T}} = \epsilon_0 \left(\mathbf{EE} + c^2 \mathbf{BB} - \frac{1}{2} \overleftrightarrow{\mathbf{I}} (E^2 + c^2 B^2) \right), \quad (1.24)$$

where $\overleftrightarrow{\mathbf{I}}$ is the unit dyadic.

Now we can rewrite Eq. (1.23):

$$\begin{aligned} \frac{d}{dt} (\mathbf{p}_{\text{mech}} + \mathbf{p}_{\text{field}}) &= \iiint_V (\rho \mathbf{E} + \mathbf{J} \times \mathbf{B}) dV + \frac{1}{c^2} \frac{d}{dt} \iiint_V (\mathbf{E} \times \mathbf{H}) dV \\ &= \iiint_V \nabla \cdot \overleftrightarrow{\mathbf{T}} dV \\ &= \oint_S \overleftrightarrow{\mathbf{T}} \cdot \mathbf{n} dS, \end{aligned} \quad (1.25)$$

where we have denoted

$$\mathbf{p}_{\text{field}} = 1/c^2 \iiint_V (\mathbf{E} \times \mathbf{H}) dV \quad (1.26)$$

as the field momentum, and where \mathbf{n} is the unit vector oriented from interior to exterior of a closed surface S . Therefore, $\overleftrightarrow{\mathbf{T}} \cdot \mathbf{n}$ can be identified as the normal flow of the momentum time derivative per unit area outside of the volume enclosed by the surface S .

The Maxwell stress tensor formalism is commonly employed for calculations of the forces acting on various objects in a presence of the external electromagnetic field. In some cases, which will be discussed later, this approach is more advantageous than the direct utilization of the differential Lorentz force. Notice that in a general case, we need to know the fields inside the object's volume to calculate the mechanical force acting on it.

A simpler way how to calculate the force exerted by electromagnetic radiation is to exploit the momentum balance argument. In such a case, a field momentum density is assigned to light propagating in material media and then the momentum conservation law is applied. The change in the optical (or field) momentum has to be compensated by an equal and opposite change in the mechanical momentum [23, 24]. However, different formulations of the field momentum density, corresponding relativistic energy-momentum tensors, and four-force densities are used in ponderable media, specifically either Abraham's or Minkowski's expressions. The experimental observations support the Minkowski field momentum in some cases and the Abraham's formulation in the other ones, depending on the nature of the experiment [25, 26].

Nevertheless, if we use the fundamental formulation coming from the differential Lorentz force (1.20), we should get right results for the force acting on the material body [27–30]. For the evaluation of the mechanical force we can therefore use either expression (1.20) or (1.25) which was derived from the former one only using vector identities and rearrangements.

1.3. Vector and scalar potentials

Now we will define potentials, connected with the electric and magnetic fields, which are often used in electrodynamics as they can simplify solutions of some problems. If we look at Eq. (1.2) and realize that the divergence of the curl of any vector is zero, we can introduce the vector potential \mathbf{A} [19, 31]:

$$\mathbf{B} = \nabla \times \mathbf{A}. \quad (1.27)$$

After substituting Eq. (1.27) into Eq. (1.3) and considering the identity which says that curl of gradient of any scalar function vanishes, we can define a scalar potential Φ that fulfills:

$$\mathbf{E} + \frac{\partial \mathbf{A}}{\partial t} = -\nabla \Phi. \quad (1.28)$$

If we apply $\nabla \cdot$ to Eq. (1.28) and utilize Eq. (1.11), we can write it as

$$\nabla^2 \Phi + \frac{\partial}{\partial t} (\nabla \cdot \mathbf{A}) = -\frac{\rho}{\varepsilon_0}. \quad (1.29)$$

Now we express Eq. (1.12) by means of the potentials:

$$\nabla^2 \mathbf{A} - \frac{1}{c^2} \frac{\partial^2 \mathbf{A}}{\partial t^2} - \nabla \left(\nabla \cdot \mathbf{A} + \frac{1}{c^2} \frac{\partial \Phi}{\partial t} \right) = -\mu_0 \mathbf{J}. \quad (1.30)$$

To continue with the treatment of Eqs. (1.29) and (1.30), we realize that the definition of the vector potential in Eq. (1.27) allows us to add to the vector potential a gradient of some scalar function Λ without changing \mathbf{B} . The scalar potential must be then transformed accordingly. Explicitly:

$$\mathbf{A} \rightarrow \mathbf{A}' = \mathbf{A} + \nabla \Lambda, \quad \Phi \rightarrow \Phi' = \Phi - \frac{\partial \Lambda}{\partial t}. \quad (1.31)$$

This property enables us to choose a set of potentials satisfying the Lorenz calibration condition

$$\nabla \cdot \mathbf{A} + \frac{1}{c^2} \frac{\partial \Phi}{\partial t} = 0 \quad (1.32)$$

and to obtain two inhomogeneous decoupled wave equations for the potentials

$$\nabla^2 \Phi - \frac{1}{c^2} \frac{\partial^2 \Phi}{\partial t^2} = -\frac{\rho}{\varepsilon_0}, \quad \nabla^2 \mathbf{A} - \frac{1}{c^2} \frac{\partial^2 \mathbf{A}}{\partial t^2} = -\mu_0 \mathbf{J}. \quad (1.33)$$

It is sometimes convenient to have the wave equations (1.33) expressed in terms of the free sources. In a non-magnetic material ($\mu_r = 1$), the wave equations for the potentials can be (with modification of the Lorenz calibration condition $\nabla \cdot \mathbf{A} = -\varepsilon_r/c^2 \partial \Phi / \partial t$) rewritten as

$$\nabla^2 \Phi - \varepsilon_r \frac{1}{c^2} \frac{\partial^2 \Phi}{\partial t^2} = -\frac{\rho_F}{\varepsilon_r \varepsilon_0}, \quad \nabla^2 \mathbf{A} - \varepsilon_r \frac{1}{c^2} \frac{\partial^2 \mathbf{A}}{\partial t^2} = -\mu_0 \mathbf{J}_F. \quad (1.34)$$

1.3. VECTOR AND SCALAR POTENTIALS

If we perform the transformation of Eq. (1.34) to Fourier space, we obtain:

$$\left[k^2 - \frac{\omega^2}{c^2} \epsilon_r(\omega) \right] \phi(\mathbf{k}, \omega) = \frac{\rho_F(\mathbf{k}, \omega)}{\epsilon_r(\omega) \epsilon_0}, \quad \left[k^2 - \frac{\omega^2}{c^2} \epsilon_r(\omega) \right] \mathcal{A}(\mathbf{k}, \omega) = \mu_0 \mathcal{J}_F(\mathbf{k}, \omega). \quad (1.35)$$

The scalar and vector potentials are very useful in dealing with problems related to the electromagnetic fields. In the following chapters we are going to demonstrate their use in numerical calculations of electron energy loss spectra.

2. Dielectric response of metallic nanoparticles

Metals have always been of great interest due to their extraordinary optical properties or high electrical and thermal conductivity. A development of the first more comprehensive theoretical description of metallic materials started at the end of the 19th century, when Paul Drude proposed a classical model explaining the transport properties of electrons in materials [32, 33]. In 1905, the model was extended by Hendrik Antoon Lorentz and some elements of quantum theory were later supplemented by Arnold Sommerfeld and Hans Bethe [34].

Nowadays, first principles calculations [35] together with relativistic corrections [36] can be used when we need an accurate description of a metallic structure or a response to an external perturbation. Not only bulk material properties can be calculated – actually the most desirable approach is to include the finite size of our considered system [37]. Calculations dealing with metallic clusters with different number of atoms can serve as an appropriate example [38–40]. Unfortunately, this approach is very computationally demanding and we also have to consider some approximations in first principles calculations.

Several theoretical works offering a possibility to approximate some of the non-classical effects in the metallic nanoparticle response were introduced [41–44] as well as experimental observations of classically unexpected features [45–47]. However, in many situations the classical theory still provides sufficient description of the problem, or at least the first insight. For cases where the classical model ceases validity, more involved semi-classical models, which will be introduced in this chapter, have been developed.

2.1. Classical dielectric models

The classical Lorentz-Drude model (sometimes called only Drude model) treats the metal as an environment containing heavy positive ions sitting in a crystalline lattice and an electron gas composed of conduction electrons. We then assume heavy ions whose movement is neglected compared to the electrons which move freely but suffer instantaneous collisions. Between the collisions, they do not interact with the fields of positive ions neither with the other electrons [48].

If we apply an external electric field \mathbf{E} , the electrons will experience a force acting on them. We can write the equation of motion as:

$$m_e \ddot{\mathbf{r}} + m_e \gamma \dot{\mathbf{r}} = -e \mathbf{E}, \quad (2.1)$$

where \mathbf{r} is a displacement vector, m_e is the electron mass and γ is a probability of scattering event per unit time. If we expect a harmonically time-dependent external field [$\mathbf{E}(t) = \mathbf{E}_0 \exp(-i\omega t)$], the stationary solution will take the form

$$\mathbf{r}(t) = \frac{e}{m_e} \frac{1}{\omega^2 + i\gamma\omega} \mathbf{E}(t). \quad (2.2)$$

2.1. CLASSICAL DIELECTRIC MODELS

As the electrons are being displaced from their equilibrium positions, the matter gets polarized. The polarization vector $\mathbf{P}(t)$ is here defined as the average value of the dipole moment ($\mathbf{p} = -er$) per unit volume, therefore in this case it can be expressed as

$$\mathbf{P}(t) = -\frac{\mathcal{N}e^2}{m_e(\omega^2 + i\gamma\omega)} \mathbf{E}(t), \quad (2.3)$$

where \mathcal{N} is a number of electrons per unit volume. After comparison of Eq. (2.3) with Eq. (1.5) and considering Eq. (1.13) with local and isotropic response, we finally get the expression for the relative electric permittivity (dielectric function)

$$\varepsilon_r(\omega) = 1 - \frac{\omega_p^2}{\omega^2 + i\gamma\omega}, \quad (2.4)$$

where we have introduced the plasma frequency $\omega_p^2 = \mathcal{N}e^2/\varepsilon_0 m_e$. We can also include other non-resonant contributions to polarization (ε_∞) and modify Eq. (2.4) as

$$\varepsilon_r(\omega) = \varepsilon_\infty - \frac{\omega_p^2}{\omega^2 + i\gamma\omega}. \quad (2.5)$$

The dielectric function can be written in the terms of its real $\varepsilon_{r1}(\omega)$ and imaginary $\varepsilon_{r2}(\omega)$ parts:

$$\varepsilon_r(\omega) = \varepsilon_{r1}(\omega) + i\varepsilon_{r2}(\omega), \quad (2.6)$$

where the real and imaginary part read, respectively,

$$\varepsilon_{r1}(\omega) = \text{Re}\{\varepsilon_r(\omega)\} = \varepsilon_\infty - \frac{\omega_p^2}{\omega^2 + \gamma^2}, \quad (2.7)$$

$$\varepsilon_{r2}(\omega) = \text{Im}\{\varepsilon_r(\omega)\} = \frac{\omega_p^2}{\omega(\omega^2 + \gamma^2)}. \quad (2.8)$$

In table 2.1, the commonly used Drude parameters for three different metals (aluminium, gold and silver) are displayed. The Lorentz-Drude dielectric function (2.5) of aluminium is plotted together with the experimental data from Ref. [49] in Fig. 2.1. In this case, the model quite nicely covers the dielectric properties of aluminium, except of one spectral discrepancy around 1.5 eV which is attributed to interband transitions [50]. On the contrary, the response of gold is only hardly described by the Lorentz-Drude model as the interband transitions are very pronounced together with relativistic effects [36].

Table 2.1: Drude parameters for aluminium, gold and silver. The values for gold and silver were taken from MNPBEM software [51].

	$\hbar\omega_p$ (eV)	$\hbar\gamma$ (eV)	ε_∞
Al	15.1	0.15	1.0
Au	9.03	0.066	10.0
Ag	9.03	0.022	3.3

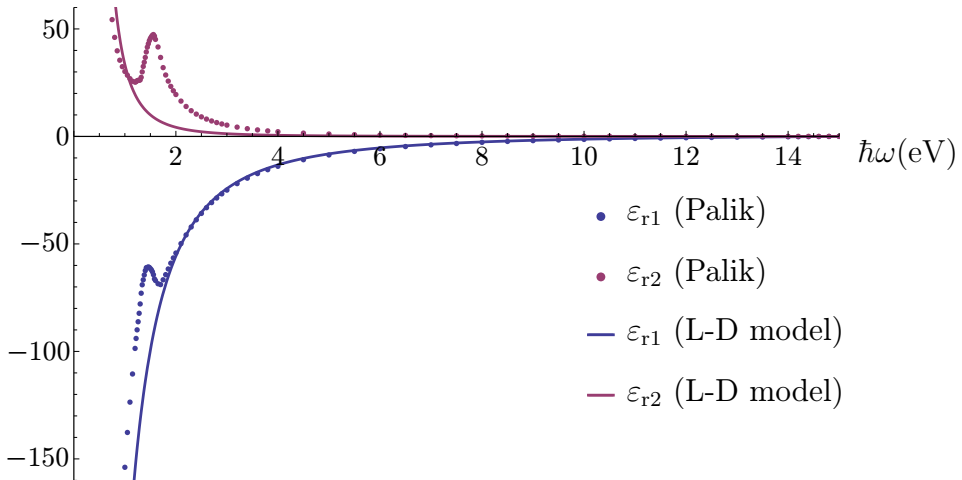


Figure 2.1: Real (blue) and imaginary (red) part of the dielectric function of aluminium. Dots represent experimental data taken from Ref. [49], while continuous curves were obtained by substituting the parameters from table 2.1 in the Lorentz-Drude model (2.5).

Within the classical framework, the contribution of the electron interband transitions to the dielectric function can be either modelled by additional Lorentz oscillators

$$\varepsilon_r(\omega) = 1 - \frac{\omega_p^2 f_0}{\omega^2 + i\gamma_0 \omega} + \sum_j \frac{\omega_p^2 f_j}{\omega_{0,j}^2 - \omega^2 - i\gamma_j \omega}, \quad (2.9)$$

where f_j is an oscillator strength, $\omega_{0,j}$ a frequency and γ_j a damping related to the Lorentz oscillator, which represents a specific transition [52, 53], or we can use more elaborated approaches [53, 54]. In the Brendel-Bormann model described in Refs. [53, 55], a Lorentz oscillator is replaced by a superposition of an infinite number of oscillators

$$\chi_j(\omega) = \frac{1}{\sqrt{2\pi}\sigma_j} \int_{-\infty}^{\infty} \exp\left[-\frac{(x - \omega_j)^2}{2\sigma_j^2}\right] \frac{\omega_p^2 f_j}{(x^2 - \omega^2) + i\gamma_j \omega} dx. \quad (2.10)$$

In Eq. (2.10), additional parameters σ_j allow for a continuous change in the line shapes from purely Lorentzian ($\sigma_j \approx 0$) to nearly Gaussian ($\gamma_j \approx 0$). The integral can be expressed in terms of the Kummer functions of the second kind $U(a, b, z)$, which are confluent hypergeometric functions, readily implemented in languages as MATLAB [56] or Mathematica [57]. The final expression for the Brendel-Bormann dielectric function then reads

$$\varepsilon_r(\omega) = \varepsilon_{\infty} - \frac{\omega_p^2}{\omega^2 + i\gamma\omega} + \sum_j \chi_j(\omega). \quad (2.11)$$

In the case of gold, accurate fits with fitting parameters can be found in literature [53, 54, 58], but mostly limited to low energies up to visible range. If we directly use the models (2.9) and (2.11) with parameters from Ref. [53], we obtain great agreement up to energy ≈ 5 eV. Above this energy, the presented fits only hardly reproduce the experimentally measured data.

2.1. CLASSICAL DIELECTRIC MODELS

Table 2.2: Parameters obtained from the fitting of the Lorentz-Drude model with contribution of Lorentz oscillators [see Eq. (2.9)] to the experimentally measured dielectric properties of gold. These parameters are used in plot 2.2, where the fit is shown over wide energy range.

j	f_j	$\hbar\omega_{0,j}$ (eV)	$\hbar\gamma_j$ (eV)
0	0.760		0.053
1	0.024	0.415	0.241
2	0.010	0.830	0.345
3	0.071	2.969	0.870
4	0.601	4.304	2.494
5	0.720	8.212	3.680
6	2.301	13.240	9.161
7	2.459	20.902	6.760
8	2.732	31.750	9.903

In order to cover much wider energy range with a good quality fit, we used the model (2.9) with seven oscillators and the plasma frequency $\hbar\omega_p = 9.03$ eV. The parameters of oscillators at lower energies were taken from Ref. [53] and supplemented by three additional oscillators, which is summarized in table 2.2. The final fit together with experimental data for gold (again taken from Ref. [49]) is plotted in Fig. 2.2.

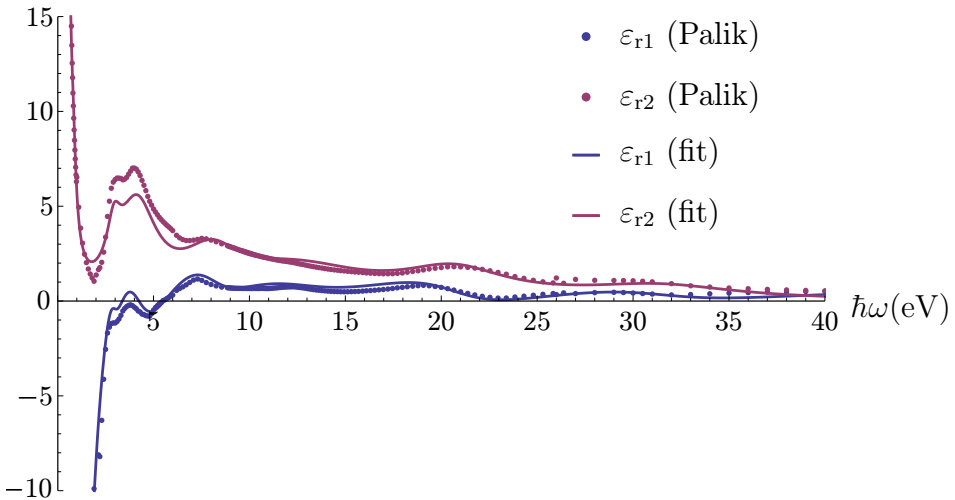


Figure 2.2: Experimental data for the dielectric function of gold (plotted with dots) taken from Ref. [49] together with the Lorentz-Drude and Lorentzian oscillator model (see Eq. (2.9) and tables 2.1 and 2.2 with parameters). The real part of dielectric function is represented by blue colour, whereas the imaginary part by red.

Importantly, all presented models (when we are assuming $\varepsilon_\infty = 1$) naturally fulfil the Kramers-Kronig relations¹ [59], expressing the condition of causal behaviour, which will be very important in the following treatment. The models are also local and neglect spatial dispersion (i.e. they exhibit only ω dependence).

2.2. Non-classical response of metallic nanoparticles

When going from bulk to nanostructured material, we have to be very careful when using the bulk dielectric properties as the most phenomena are different at nanoscale [37, 60]. We can basically consider three main features causing the possible inaccuracies when exploiting the classical theory [61]:

- The quantum-confinement causes that the electrons undergo surface collisions more often, even at a rate comparable to the intrinsic damping rate γ . This effect can be treated phenomenologically by increasing the damping parameter in Eq. (2.4) or (2.5) [37]

$$\varepsilon_r(\omega) = \varepsilon_\infty - \frac{\omega_p^2}{\omega^2 + i\gamma\omega + i\omega Av_F/a}, \quad (2.12)$$

where $A \sim 1$ is a fitting parameter, v_F is the Fermi velocity and a is the particle radius (or a characteristic dimension). A different approach was used in Ref. [47], where the electrons were assumed to move in an infinite spherical potential well.

- At a metal-dielectric interface, a step-function profile of a dielectric function is assumed, which is only approximation. In real systems, the finite quantum mechanical spill-out of the electron density appears, which contributes with tunnelling currents to the response of surfaces in close proximity [42, 62].
- In the classical local-response theories, the dielectric function in Eq. (1.13) does not exhibit the spatial dispersion and in the frequency domain, Eq. (1.13) can be rewritten as $\mathcal{D}(\mathbf{r}, \omega) = \varepsilon(\mathbf{r}, \omega)\mathcal{E}(\mathbf{r}, \omega)$. The electron density is then assumed to be constant over the whole volume of the nanoobject. When we take non-locality into account, we involve a slight deviation of the electron density. A finite penetration depth of the induced charge inside the metal is then introduced [42, 61]. Analytical expressions were derived for the bulk non-local dielectric response of the free electron gas [63], but for particular problem geometries the treatment of non-locality still remains very complex.

The last two mentioned effects are schematically depicted in Fig. 2.3. Although in general, all the mechanisms add up, in the followings we focus on non-locality, whose theoretical description was of great attention during the past decades.

One of the possibilities how to deal with the non-local effects is to use the hydrodynamic Drude model, in which the electron density $\mathcal{N}(\mathbf{r}, t)$ and the hydrodynamical

¹If we define the electric susceptibility $\chi_e = \varepsilon_r - 1$, for its real χ_1 and imaginary χ_2 parts, respectively, it holds: $\chi_1(\omega) = \frac{1}{\pi} \mathcal{P} \int_{-\infty}^{\infty} \chi_2(\omega')/(\omega' - \omega) d\omega'$ and $\chi_2(\omega) = -\frac{1}{\pi} \mathcal{P} \int_{-\infty}^{\infty} \chi_1(\omega')/(\omega' - \omega) d\omega'$, respectively, where \mathcal{P} denotes the Cauchy principal value.

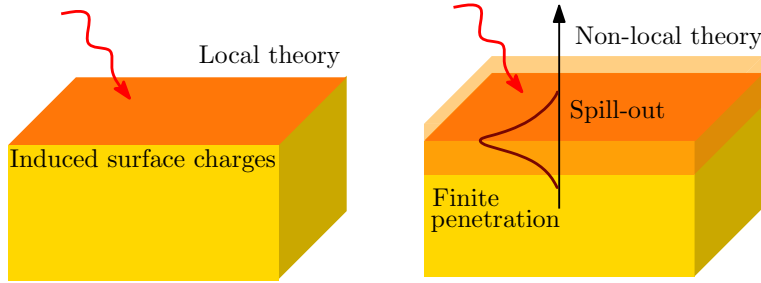


Figure 2.3: Schematics of differences between the local-response approximation, when the induced charge is confined to the interface, and the non-local theory, where the finite penetration depth of the charge in metal is taken into account. The electrons are also spilling out of the material, causing tunnelling currents. Figure was adapted from Ref. [42].

velocity $\mathbf{v}(\mathbf{r}, t)$ characterizing the collective motion of the electrons exhibit spatial and temporal variations governed by the Navier-Stokes equation [64]

$$\left(\frac{\partial}{\partial t} + \mathbf{v} \cdot \nabla \right) \mathbf{v} = -\gamma \mathbf{v} - \frac{e}{m_e} (\mathbf{E} + \mathbf{v} \times \mathbf{B}) - \frac{\beta^2}{\mathcal{N}} \nabla \mathcal{N}, \quad (2.13)$$

where the β factor, appearing in the last term expressing the internal kinetic energy of the electron gas, depends on a particular model we choose for the electron gas description. Here we assume the Thomas-Fermi model with β being proportional to the Fermi velocity: $\beta = (3/5)^{1/2} v_F$. On the right-hand side of Eq. (2.13), we can also observe the damping term containing γ , and the driving Lorentz force. Moreover, the electrons have to fulfil the continuity equation

$$\frac{\partial \mathcal{N}}{\partial t} = -\nabla \cdot (\mathcal{N} \mathbf{v}). \quad (2.14)$$

Eqs. (2.13) and (2.14) can be linearized and rewritten in the frequency domain as [42, 64, 65]

$$\frac{\beta^2}{\omega(\omega + i\gamma)} \nabla [\nabla \cdot \mathcal{J}(\mathbf{r}, \omega)] + \mathcal{J}(\mathbf{r}, \omega) = \sigma(\omega) \mathcal{E}(\mathbf{r}, \omega), \quad (2.15)$$

where $\sigma(\omega) = i\epsilon_0 \omega_p^2 / (\omega + i\gamma)$ is the conductivity of the free electron gas. If we rewrite the general non-local expression (1.15) in the local form for isotropic material as $\mathcal{J}(\mathbf{r}, \omega) = \sigma(\omega) \mathcal{E}(\mathbf{r}, \omega)$ and compare it with Eq. (2.15), the only difference is the first term which can be viewed as a non-local correction. Despite the fact that this term makes the solution more complicated, it is still better than with the general non-local relation. Besides Eq. (2.15), the electric field also has to obey Maxwell's equations from which we can derive the non-homogeneous wave equation

$$\nabla \times \nabla \times \mathcal{E}(\mathbf{r}, \omega) - \frac{\omega^2}{c^2} \epsilon_\infty \mathcal{E}(\mathbf{r}, \omega) = i\omega \mu_0 \mathcal{J}(\mathbf{r}, \omega). \quad (2.16)$$

Eqs. (2.15) and (2.16) can be now solved either analytically or numerically to obtain the field \mathcal{E} and the currents \mathcal{J} . Note that this model is semiclassical as the only quantity introducing the quantum properties of the system is the Fermi velocity. The model

2. DIELECTRIC RESPONSE OF METALLIC NANOPARTICLES

therefore does not provide fully quantum treatment. However, it can sometimes give results qualitatively agreeing with ab initio calculations [66] or experimental results [47].

Non-locality can be treated analytically for the spherical geometry [67] which will be exploited in Chapter 4. In the case of the spheres, Lindhard dielectric function [68] has also been considered instead of the hydrodynamical dielectric function [67, 69, 70], as well as specular reflection model approach [41, 42]. Recent papers show that this topic can still be extended, e.g. diffusion of the charge was taken into account [71] or the role of non-local effects in the case of different probes was examined [61].

2.2. NON-CLASSICAL RESPONSE OF METALLIC NANOPARTICLES

3. Electron energy loss spectroscopy

In transmission electron microscopy, the interaction of swift electrons with a sample gives rise to many different signals (among others the secondary electron emission, cathodoluminescence or Auger electron emission). In this chapter, we will focus on the method which is based on analysis of energy distribution of the electrons transmitted through the sample, the electron energy loss spectroscopy [72].

A basic scheme of an electron microscope using the transmitted electrons for a sample analysis can be seen in Fig. 3.1 a): the electrons extracted from an electron gun first have to be monochromated. Thereafter, the focusing onto the sample, the beam interacts with, is performed. The electrons can be either elastically scattered (in such a case they preserve the initial energy), or they can suffer energy losses related to various excitation processes in the sample. Part of the transmitted electrons is then analysed by a spectrometer which enables us to record the electron energy loss spectra.

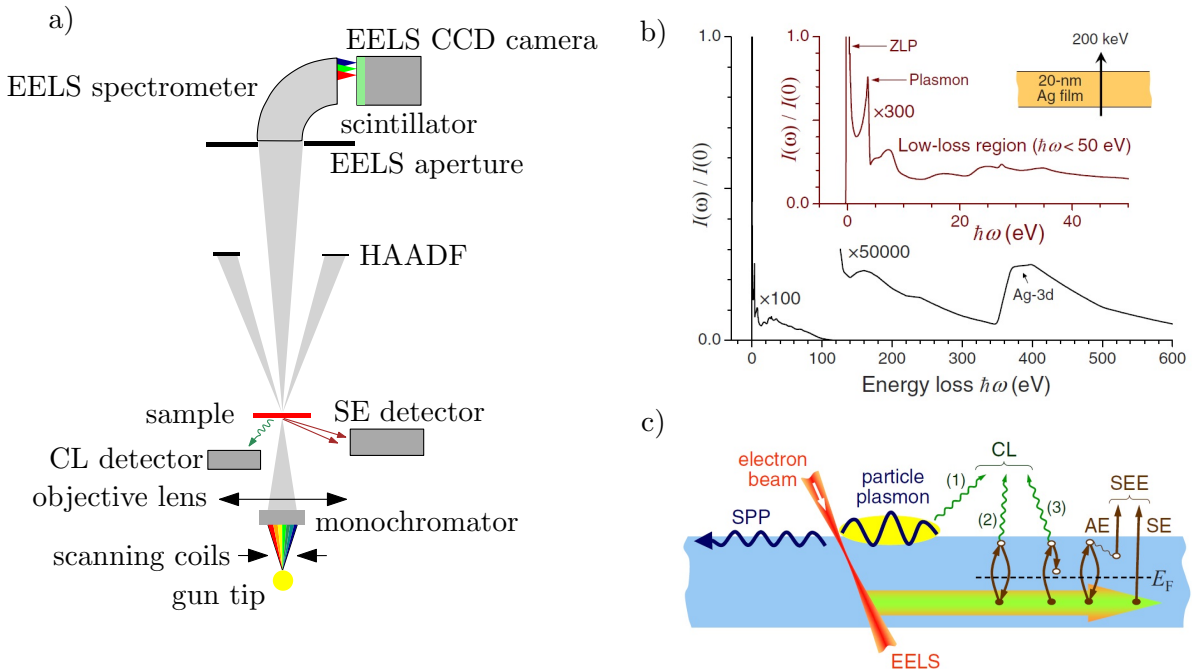


Figure 3.1: a) A brief scheme of an electron microscope with electron energy loss spectroscopy equipment. Some of other detectors are also depicted: high-angle annular dark-field (HAADF), secondary electron (SE) and cathodoluminescence (CL) detectors. Scheme inspired by Ref. [9]. b) Typical electron energy loss spectrum for a sample consisting of 20-nm thick silver film. c) Some of excitation processes and signals coming from the sample. Surface plasmon polaritons (SPP), particle plasmons or electronic excitations can arise. We can detect secondary electrons (SE), cathodoluminescence (CL) or transmitted electrons by an EELS apparatus. Pictures b) and c) taken from Ref. [72].

An example of such a spectrum corresponding to 20-nm silver film is shown in Fig. 3.1 b) [72], where we can basically distinguish the high-energy core excitations and the more intensive low-energy valence excitations which are related to the optical response of material [72, 73]. Electron energy loss spectroscopy (EELS) can therefore provide

3.1. FIELD OF A MOVING ELECTRON

information complementary to optical spectroscopies, but with substantially better spatial resolution as the optical methods are severely limited by diffraction.

Some of the excitations usually appearing in the low-loss region are depicted in Fig. 3.1 c). The impinging electrons can excite surface plasmon polaritons (SPP), particle plasmons or cause electronic excitations. These processes usually contribute to different signals as indicated in the picture: cathodoluminescence (CL), secondary electron emission (SE), Auger electrons (AE) and finally EELS [72].

However, the so called zero-loss peak corresponding to the electrons which did not suffer any energy loss is the most intensive spectral feature. As we can see, it has got a finite width which limits an energy resolution of this technique. This limit had been the only disadvantage until recently when the beam monochromator and aberration-corrected optics was significantly improved, which enabled us to probe even molecular vibrations in infrared region [2]. Nevertheless, further advances in the instrumentation are expected in future.

Unfortunately, not only the energy resolution of EELS can be problematic – the measured raw data have to be processed and deconvolved to obtain spectra which are often interpreted with considerable difficulties due to multiple inelastic scattering, Čerenkov radiation losses [74] or wide variety of loss processes that can take place [72,73]. Theoretical modeling of EEL spectra is therefore necessary for correct interpretation of experiments.

This chapter should provide a brief insight into calculations of theoretical EEL spectra. For this purpose we first introduce the field produced by moving relativistic electrons both in the time and frequency domain and discuss the swift electron probe properties. Then we present the classical dielectric formalism and analytic expressions of the energy loss probabilities for the simplest geometries: an electron moving in a bulk material, along or perpendicular to a planar surface and nearby a dielectric sphere, which allows excitations of localized modes. The last part of the chapter is devoted to an introduction of the boundary element method, which is the most commonly used numerical approach in the EELS calculations.

3.1. Field of a moving electron

The fields produced by a moving relativistic electron can be expressed in a laboratory rest frame (x, y, z) easily with use of lorentzian transform from the electron rest frame (x', y', z') . Without loss of generality we consider an electron moving in the z direction with velocity $\mathbf{v} = (0, 0, v)$ and at time $t = t' = 0$ intersecting the plane $z = 0$ in point $[b, 0, 0]$. The Cartesian components of the fields then read [19]

$$E_x^{\text{ext,out}}(x, y, z, t) = -\frac{e\gamma}{4\pi\epsilon_0} \frac{x - b}{[(x - b)^2 + y^2 + \gamma^2(z - vt)^2]^{\frac{3}{2}}}, \quad (3.1a)$$

$$E_y^{\text{ext,out}}(x, y, z, t) = -\frac{e\gamma}{4\pi\epsilon_0} \frac{y}{[(x - b)^2 + y^2 + \gamma^2(z - vt)^2]^{\frac{3}{2}}}, \quad (3.1b)$$

$$E_z^{\text{ext,out}}(x, y, z, t) = -\frac{e\gamma}{4\pi\epsilon_0} \frac{z - vt}{[(x - b)^2 + y^2 + \gamma^2(z - vt)^2]^{\frac{3}{2}}}, \quad (3.1c)$$

$$B_x^{\text{ext,out}}(x, y, z, t) = \frac{e\gamma}{4\pi\epsilon_0} \frac{\beta}{c} \frac{y}{[(x - b)^2 + y^2 + \gamma^2(z - vt)^2]^{\frac{3}{2}}}, \quad (3.2a)$$

3. ELECTRON ENERGY LOSS SPECTROSCOPY

$$B_y^{\text{ext,out}}(x, y, z, t) = -\frac{e\gamma}{4\pi\varepsilon_0 c} \frac{\beta}{[(x-b)^2 + y^2 + \gamma^2(z-vt)^2]^{\frac{3}{2}}}, \quad (3.2b)$$

$$B_z^{\text{ext,out}}(x, y, z, t) = 0, \quad (3.2c)$$

where e is the elementary charge, $\beta = v/c$ and we introduced the Lorentz factor

$$\gamma = \frac{1}{\sqrt{1 - \beta^2}}. \quad (3.3)$$

We have also used superscripts $^{\text{ext,out}}$ whose use will be enlightened in the following chapter.

To express the fields (3.1) and (3.2) in the frequency domain, we substitute them into definition (A4) and with use of the integral definition of modified Bessel functions of the second kind of order ν

$$K_\nu(\xi\zeta) = \frac{\Gamma(\nu + \frac{1}{2})(2\zeta)^\nu}{\sqrt{\pi\xi^\nu}} \int_0^\infty \frac{\cos(\xi t)}{(t^2 + \zeta^2)^{\nu + \frac{1}{2}}} dt, \quad (3.4)$$

where $\Gamma(\nu + \frac{1}{2})$ is the Euler gamma function, we can after some algebra get

$$\mathcal{E}_x^{\text{ext,out}}(x, y, z, \omega) = -\frac{2\omega(x-b)}{\gamma v^2} \frac{\exp(i\frac{\omega z}{v})}{\sqrt{(x-b)^2 + y^2}} K_1\left(\frac{\omega\sqrt{(x-b)^2 + y^2}}{\gamma v}\right), \quad (3.5a)$$

$$\mathcal{E}_y^{\text{ext,out}}(x, y, z, \omega) = -\frac{2\omega y}{\gamma v^2} \frac{\exp(i\frac{\omega z}{v})}{\sqrt{(x-b)^2 + y^2}} K_1\left(\frac{\omega\sqrt{(x-b)^2 + y^2}}{\gamma v}\right), \quad (3.5b)$$

$$\mathcal{E}_z^{\text{ext,out}}(x, y, z, \omega) = \frac{i2\omega}{\gamma^2 v^2} \exp\left(i\frac{\omega z}{v}\right) K_0\left(\frac{\omega\sqrt{(x-b)^2 + y^2}}{\gamma v}\right), \quad (3.5c)$$

$$\mathcal{B}_x^{\text{ext,out}}(x, y, z, \omega) = \frac{2\omega y}{\gamma v c} \frac{\exp(i\frac{\omega z}{v})}{\sqrt{(x-b)^2 + y^2}} K_1\left(\frac{\omega\sqrt{(x-b)^2 + y^2}}{\gamma v}\right), \quad (3.6a)$$

$$\mathcal{B}_y^{\text{ext,out}}(x, y, z, \omega) = -\frac{2\omega(x-b)}{\gamma v c} \frac{\exp(i\frac{\omega z}{v})}{\sqrt{(x-b)^2 + y^2}} K_1\left(\frac{\omega\sqrt{(x-b)^2 + y^2}}{\gamma v}\right), \quad (3.6b)$$

$$\mathcal{B}_z^{\text{ext,out}}(x, y, z, \omega) = 0. \quad (3.6c)$$

The expressions in the frequency domain (3.5) and (3.6) were derived in atomic units defined in Appendix B.

It should be remarked that in the frequency domain the electron appears as a charge distribution oscillating along z direction and furthermore, the fields are naturally evanescent as the modified Bessel functions decay exponentially for large arguments. The electromagnetic field is therefore highly localized near the electron trajectory. The distance $\approx v\gamma/\omega$, when the field approximately decays to $1/e$, is called the Bohr cutoff. However, at the points along the trajectory of the electron, a singularity appears as we can see behaviour of the modified Bessel functions illustrated in Fig. 3.2.

3.2. CLASSICAL DIELECTRIC FORMALISM

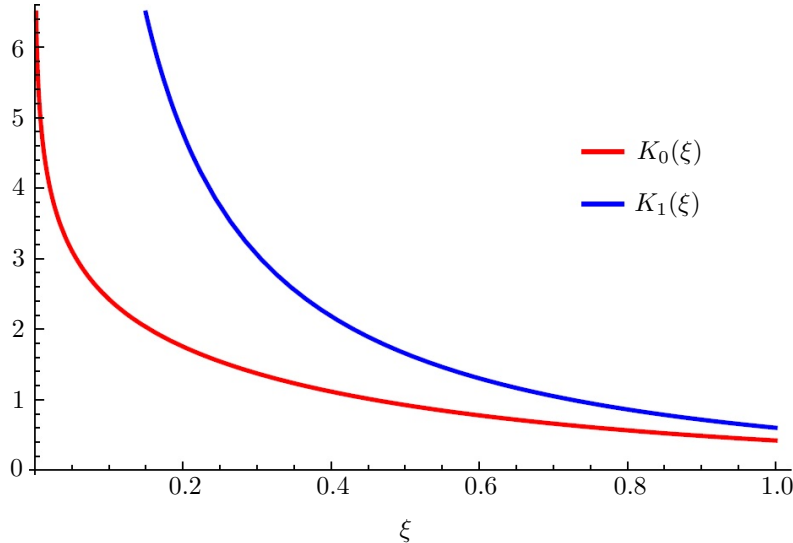


Figure 3.2: Plot of the zeroth and the first order Bessel function of the second kind. Both functions are divergent for $\xi \rightarrow 0$.

3.2. Classical dielectric formalism

In the previous section, we obtained the expressions for the electromagnetic field produced by fast electrons in infinite space, which gave us the first insight into our problem.

Calculations of the electromagnetic field in realistic geometries are much more complex because in cases of our interest, when the electron interacts with real samples, it can move near targets of different shapes and composition. When passing close to or through the sample, the fields produced by the electron polarize matter, giving rise to induced field \mathbf{E}^{ind} that acts back on the electron causing its energy loss, which can usually be treated with help of classical electrodynamics. This so-called dielectric approach was probably for the first time used by Fermi [75], who calculated stopping power for fast charges moving in different materials.

The problem of the energy loss can also be understood in a different way. From the point of view of the electrons of the target, the field produced by the moving electron can be treated as a perturbation which causes transitions from occupied to unoccupied levels. In other words, the electrons of the target gain energy and momentum to the detriment of the probe.

Using the first approach, the total energy loss ΔE can be computed by integrating the scalar product of the force stopping the electron and its unit trajectory [5, 72]

$$\Delta E = e \int_{-\infty}^{\infty} \mathbf{E}^{\text{ind,out}}(\mathbf{r}'(t), t) \cdot \frac{d\mathbf{r}'(t)}{dt} dt = e \int_{-\infty}^{\infty} \mathbf{v} \cdot \mathbf{E}^{\text{ind,out}}(\mathbf{r}'(t), t) dt. \quad (3.7)$$

Employing the Rayleigh-Parseval theorem (A11) as we deal with a real function, we can express the energy loss as [72]:

$$\Delta E = \int_0^{\infty} \hbar\omega \Gamma_{\text{EELS}}(\omega) d\omega, \quad (3.8)$$

where

$$\Gamma_{\text{EELS}}(\omega) = \frac{e}{\pi\hbar\omega} \int_{-\infty}^{\infty} \text{Re} [\mathbf{v} \cdot \mathcal{E}^{\text{ind,out}}(\mathbf{r}'(t), \omega) \exp(-i\omega t)] dt \quad (3.9)$$

is the so-called electron energy loss probability which can be directly measured in EELS experiments, and where \hbar is the reduced Planck's constant. We thus only need to compute the induced field acting back on the electron. This has been done for many different geometries in a variety of situations, e.g. for electrons going parallel or perpendicular to infinite planar interfaces, penetrating thin films or passing near isolated or supported particles of different shapes. An overview can be found in references [72] or [76]. There were also various approaches dealing with dispersive media or relativistic descriptions, which is needed for accurate computations. These corrections can play an important role especially in the cases of high initial energies of electrons, larger targets and when the trajectories of the electrons are very close to the targets.

3.3. Bulk losses

The energy loss suffered by a relativistic electron moving in bulk material is the simplest case of our consideration. The loss probability is then expressed as [72]:

$$\Gamma_{\text{bulk}}(\omega) = \frac{e^2 L}{\pi\hbar v^2} \text{Im} \left\{ \left(\frac{v^2}{c^2} - \frac{1}{\varepsilon_r(\omega)} \right) \ln \left(\frac{q_c - (\omega/c)^2 \varepsilon_r(\omega)}{(\omega/v)^2 - (\omega/c)^2 \varepsilon_r(\omega)} \right) \right\}, \quad (3.10)$$

where L is length of trajectory that electron has passed through material and where we assumed a local response represented by $\varepsilon_r(\omega)$ (independent of the wave vector). This result also contains the so-called cutoff q_c , which is included because of the momentum conservation law and is connected with the experimental setup, where this cutoff is given by the aperture of the microscope spectrometer (ϕ_{out} is the half-aperture collection angle):

$$\hbar q_c \approx \sqrt{(m_e v \phi_{\text{out}})^2 + (\hbar \omega v)^2}. \quad (3.11)$$

The retarded bulk loss probability in Eq. (3.10) can be easily modified to obtain the non-retarded equation by considering $c \rightarrow \infty$ as

$$\Gamma_{\text{bulk}}^{\text{NR}}(\omega) = \frac{2e^2 L}{\pi\hbar v^2} \text{Im} \left\{ -\frac{1}{\varepsilon_r(\omega)} \right\} \ln(q_c v / \omega). \quad (3.12)$$

From Eq. (3.12) we can directly see that the probability will be large around the maximum of $\text{Im}\{-1/\varepsilon_r\}$. This expression is also sometimes used for determination of bulk optical constants from the calibrated experimentally measured data.

If we assume a Drude-like dielectric function ε_r to describe the local response of a metal with plasma frequency ω_p (recall Section 2.1), we will find out that the peak of bulk loss is situated at $\omega = \omega_p$, which is the frequency of bulk plasma oscillations; these excitations are usually called bulk or volume plasmons. The position of the peak will be slightly modified by the logarithm dependence. The bulk loss probability per unit path length calculated for an electron of energy 120 keV travelling in aluminium is plotted by the red dashed line in Fig. 3.3.

3.4. SURFACE MODES

3.4. Surface modes

The case of an electron moving along or penetrating a planar surface also deserves our attention because of the possible surface excitations [77, 78].

When the electron is travelling in vacuum parallel to an interface with medium characterized by a dielectric function $\varepsilon_r(\omega)$, at constant distance b , the loss probability within a non-retarded approximation is found to be [79]:

$$\Gamma_{\text{planar}}^{\text{NR}}(\omega) = \frac{4e^2 L}{\pi \hbar v^2} K_0\left(\frac{2\omega b}{v}\right) \text{Im} \left[-\frac{1}{1 + \varepsilon_r(\omega)} \right], \quad (3.13)$$

We can consider the more general situation of the electron moving inside a medium with dielectric function $\varepsilon_{r,A}(\omega)$ parallel to an interface with another material described by $\varepsilon_{r,B}(\omega)$. In this case, we obtain [79]:

$$\Gamma_{\text{planar}}^{\text{NR}}(\omega) = \frac{2e^2 L}{\pi \hbar v^2} \left\{ \ln\left(\frac{q_c v}{\omega}\right) \text{Im} \left[-\frac{1}{\varepsilon_{r,A}} \right] + K_0\left(\frac{2\omega b}{v}\right) \left(\text{Im} \left[-\frac{2}{\varepsilon_{r,A} + \varepsilon_{r,B}} \right] - \text{Im} \left[-\frac{1}{\varepsilon_{r,A}} \right] \right) \right\}. \quad (3.14)$$

The first term in the curly brackets is nothing but the bulk loss corresponding to the media where the electron is moving, while the second term is related to the interface. We can recognize there a modification of Eq. (3.13) and an additional term, which is responsible for the so-called "Begrenzung-Effekt", related to the bulk oscillation reduction caused by the excitation of surface modes. This can be clearly resolved in Fig. 3.3, where we plot the direct bulk term and the second "surface" term (marked as $\Gamma_{\text{Begrenzung}}/L$) separately for the case of an electron travelling in aluminium near the interface with vacuum. In the plot, two peaks can be seen: the first one situated very close to a value of $\hbar\omega_p/\sqrt{2}$ corresponds to the surface plasmon excited at the aluminium-vacuum interface, while the second one with approximate energy of $\hbar\omega_p$ is related to the bulk plasmon, as we saw in previous section. If we reduced the distance of the electron trajectory from the interface, we would observe an increase of the surface peak intensity at the expense of the bulk peak.

3.5. Localized modes

From the experimental point of view, both the bulk and surface losses are important because we can utilize them to determine properties of our sample and its composition. However, in reality, materials can show a more complex structure and samples can consist of many material components or can have quite complicated shapes. If we deal with metallic particles, we can observe the excitation of the so-called localized surface plasmon modes representing natural oscillations of the electron gas localized at the object [7, 80].

Small particles can be of different shapes, but the spherical geometry provides a good canonical example. The complete non-retarded solution including a possibility of higher-order mode excitations was firstly published by Ferrell and Echenique [81]. After solving Poisson's equation and matching boundary conditions with the Fourier components of the

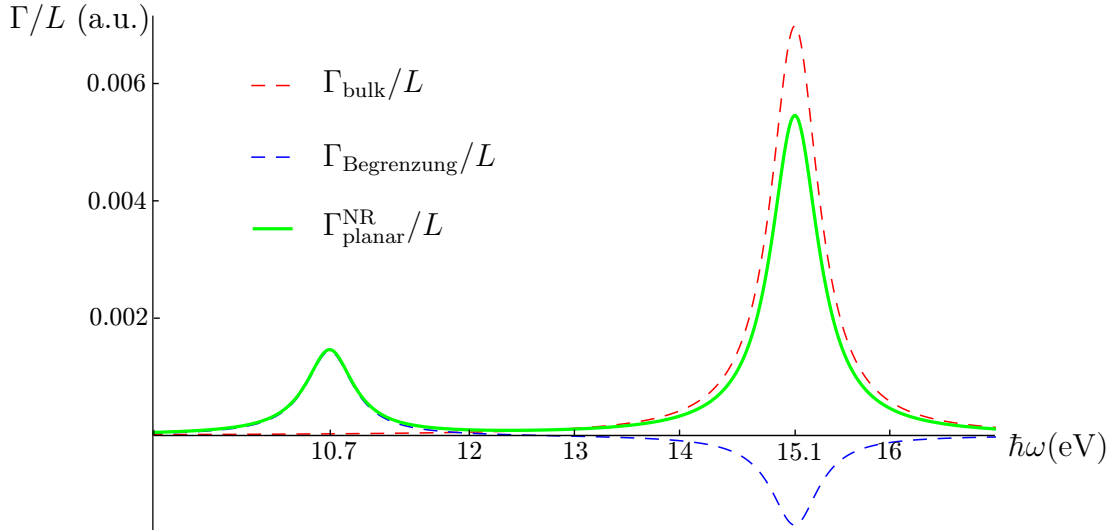


Figure 3.3: Energy loss probability per unit path length Γ/L with a split of the terms contained in Eq. (3.14) (Γ is expressed in atomic units, where $e = m_e = \hbar = 1$). Γ_{bulk}/L represents the first term in the curly brackets (red dashed line), $\Gamma_{\text{Begrenzung}}/L$ is related to the second term (blue dashed line) and the total loss probability per unit length is denoted as $\Gamma_{\text{planar}}^{\text{NR}}/L$ (green solid line). This plot corresponds to an electron of energy 120 keV travelling in aluminium at a distance $b = 2$ nm from the interface. $\varepsilon_{r,A}(\omega)$ is represented by a Drude dielectric function with parameters from table 2.1, except for the damping ($\hbar\gamma = 0.55$ eV was considered). $\varepsilon_{r,B} = 1$ is assumed to be vacuum and we considered a cutoff $q_c = 0.4$ a.u..

fields, they were able to calculate the induced field and obtained the following expression for the energy loss probability:

$$\Gamma_{\text{EELS}}^{\text{NR}}(\omega) = \frac{4e^2}{\pi\hbar v^2} \sum_{l=1}^{\infty} \sum_{m=-l}^l \frac{(\omega/v)^{2l}}{(l-m)!(l+m)!} K_m^2 \left(\frac{\omega b}{v} \right) \text{Im} \left[a^{2l+1} \frac{l\varepsilon_r(\omega) - l}{l\varepsilon_r(\omega) + l + 1} \right], \quad (3.15)$$

which holds for the sphere situated in vacuum and where $v/c \ll 1$ and $ka \ll 1$ was assumed. b is the distance of the electron trajectory from the center of the sphere with a radius a and a dielectric function $\varepsilon_r(\omega)$. The expression in square brackets is the non-retarded multipolar polarizability. If we further assume ε_r being the Drude dielectric function (2.4), from putting the denominator of the polarizability equal to zero, we get the resonance condition:

$$\omega_l \approx \omega_p \sqrt{\frac{l}{1+2l}}, \quad (3.16)$$

where ω_l is a frequency of the l^{th} mode, denoting positions of the peaks in EEL spectra.

For the case when $\omega a/v \ll 1$, the most significant contribution comes from the $l = 1$ term and we can then use the dipole approximation:

$$\Gamma_{\text{EELS}}^{\text{NR,dip}}(\omega) = \frac{4e^2\omega^2}{\pi\hbar v^4} \text{Im} \left[a^3 \frac{\varepsilon_r(\omega) - 1}{\varepsilon_r(\omega) + 2} \right] \left[K_0^2 \left(\frac{\omega b}{v} \right) + K_1^2 \left(\frac{\omega b}{v} \right) \right]. \quad (3.17)$$

3.6. BOUNDARY ELEMENT METHOD

Although Eq. (3.15) can often give a good agreement with experimental data, the effects of retardation play an important role when we consider larger spheres. In Chapter 4 we are going to introduce the fully retarded analytical approach developed by García de Abajo [18].

3.6. Boundary element method in the calculations of the loss spectra

Before we proceed to the analytical solution for the interaction between the swift electron and the sphere, we focus on a numerical approach that can be used in calculations for arbitrary problem geometries and which will be utilized for a comparison with the analytical results.

The boundary element (or charge) method (BEM) is widely used in EELS calculations as we can incorporate there naturally the fields produced by the moving electrons represented by their vector and scalar potentials [82]. This approach can be used in the non-retarded limit, where Poisson's equation [83] is numerically solved, or a fully retarded computation can also be performed using the whole set of Maxwell's equations [84].

The core of this method consists in solving self-consistently the surface integrals involving charges and currents, situated on the arbitrarily shaped interface between different dielectrics, for a given external source. To introduce the retarded approach, we will start with the wave equations for the scalar and vector potentials in Eq. (1.33), which represent the full set of Maxwell's equations. If we consider these equations in ω -space, for nonmagnetic materials we obtain

$$(\nabla^2 + k^2 \varepsilon_r) \phi = - \left(\frac{\rho_F}{\varepsilon_r \varepsilon_0} + \mathbf{D} \cdot \nabla \frac{1}{\varepsilon_r \varepsilon_0} \right), \quad (\nabla^2 + k^2 \varepsilon_r) \mathbf{A} = -\mu_0 (\mathbf{J}_F - i\omega \phi \varepsilon_0 \nabla \varepsilon_r), \quad (3.18)$$

where in addition to the terms corresponding to external charges and currents, other contributions related to the gradient of the dielectric function appear. As the discontinuity of the dielectric function arises at the interface between two media, these terms are nonzero only at the interface and represent additional boundary surface charges and currents. However, they can not be related to real interface charges and currents in a general case [84].

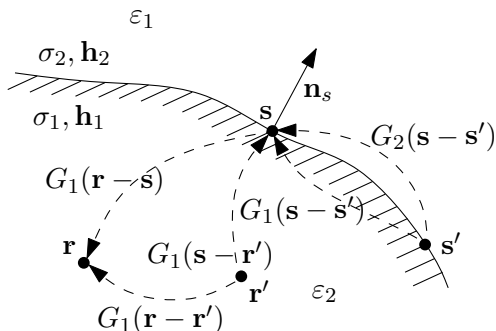


Figure 3.4: Geometric representation of an arbitrarily shaped interface separating medium 1 and 2. Scheme reproduced from [84].

3. ELECTRON ENERGY LOSS SPECTROSCOPY

If we adopt the geometry, which is depicted in Fig. 3.4 [84], we can employ the Green's function $G_j = \exp(i k_j r)/r$ of the wave equation to write the solutions of Eq. (3.18) that vanish in positions far away from the source as

$$\left\{ \begin{array}{l} \phi(\mathbf{r}) \\ \mathbf{A}(\mathbf{r}) \end{array} \right\} = \int d\mathbf{r}' G_j(|\mathbf{r} - \mathbf{r}'|) \left\{ \begin{array}{l} \rho_F(\mathbf{r}')/\varepsilon_j \\ \mu_0 \mathbf{J}_F(\mathbf{r}') \end{array} \right\} + \int d\mathbf{s} G_j(|\mathbf{r} - \mathbf{s}|) \left\{ \begin{array}{l} \sigma_j(\mathbf{s}) \\ \mathbf{h}_j(\mathbf{s}) \end{array} \right\}. \quad (3.19)$$

When we examine the form of Eq. (3.19), we find out that the first integral on the right-hand side represents the solutions everywhere in the space except at the interface. At the interface, the second integral becomes important since it both compensates the discontinuity of the Green's function and includes the effects of boundary charges σ_j and currents \mathbf{h}_j . We then apply boundary conditions requiring continuity of potentials at the interfaces between two media ($j = 1$ and $j = 2$) and obtain

$$G_1\sigma_1 - G_2\sigma_2 = -(\phi_1^e - \phi_2^e) \quad \text{and} \quad G_1\mathbf{h}_1 - G_2\mathbf{h}_2 = -(\mathbf{A}_1^e - \mathbf{A}_2^e), \quad (3.20)$$

where equivalent boundary sources read

$$\phi_j^e(\mathbf{s}) = \frac{1}{\varepsilon_j} \int d\mathbf{r}' G_j(|\mathbf{s} - \mathbf{r}'|) \rho_F(\mathbf{r}') \quad (3.21)$$

and

$$\mathbf{A}_j^e(\mathbf{s}) = \mu_0 \int d\mathbf{r}' G_j(|\mathbf{s} - \mathbf{r}'|) \mathbf{J}_F(\mathbf{r}'). \quad (3.22)$$

Now we employ the condition of continuity of both the normal derivative of the tangential vector potential and the tangential derivatives of all components of the vector potential, which holds for nonmagnetic materials. This leads to another set of equations:

$$H_1\mathbf{h}_1 - H_2\mathbf{h}_2 - ik\mathbf{n}_s(G_1\varepsilon_1\sigma_1 - G_2\varepsilon_2\sigma_2) = \alpha, \quad (3.23)$$

$$H_1\varepsilon_1\sigma_1 - H_2\varepsilon_2\sigma_2 - ik\mathbf{n}_s \cdot (G_1\varepsilon_1\mathbf{h}_1 - G_2\varepsilon_2\mathbf{h}_2) = D^e, \quad (3.24)$$

where H_j is the normal derivative of G_j and where

$$\alpha = (\mathbf{n}_s \cdot \nabla_s)(\mathbf{A}_2^e - \mathbf{A}_1^e) + ik\mathbf{n}_s(\varepsilon_1\phi_1^e - \varepsilon_2\phi_2^e), \quad (3.25)$$

$$D^e = \mathbf{n}_s \cdot [\varepsilon_1(ik\mathbf{A}_1^e - \nabla_s\phi_1^e) - \varepsilon_2(ik\mathbf{A}_2^e - \nabla_s\phi_2^e)]. \quad (3.26)$$

We can see that D^e has the meaning of the difference of the normal displacement, which would be induced by the external source at the position of the interface in the case of homogeneous space filled either with medium $j = 1$ or $j = 2$ [84].

From these four boundary conditions, four unknown quantities – the auxiliary boundary charges and currents – can be calculated and then used for evaluating the potentials. This leads to the problem of solving a system of eight linear surface-integral equations. If we want to solve it numerically, the next step consists of discretizing the surface integral in N points to obtain a set of $8N$ linear equations.

3.6. BOUNDARY ELEMENT METHOD

Calculated EEL spectra can quite nicely reproduce experimental data and help to interpret them [85, 86]. Such a comparison of experimental EEL spectra with data obtained from BEM simulation can be found in Fig. 3.5. It is apparent that the numerically calculated spectra b) do not overlap the experimental data a) perfectly. In real systems we have to deal with shape irregularities of measured particles and constraints given by the resolution of the experimental technique. However, with this approach we can at least approximately reproduce the energies of the main peaks and reveal possible modes that can be excited.

In the following chapter, MNPBEM toolbox exploiting the BEM approach will be used for the comparison with the analytically computed fields and spectra. Particularly the implementation of EELS calculations will be exploited [51, 87]. This toolbox is used within the MATLAB software [56].

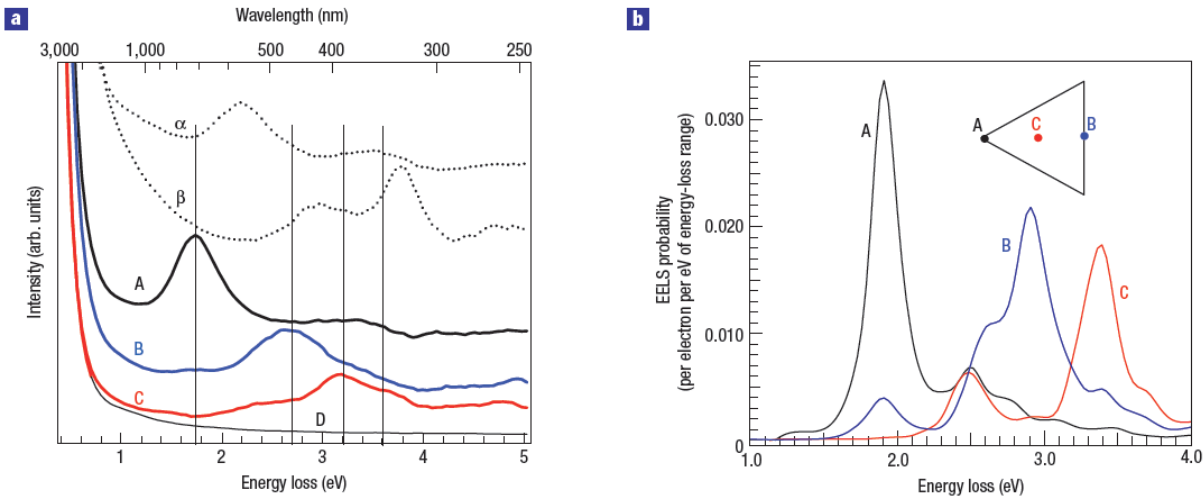


Figure 3.5: Comparison of experimental deconvoluted EEL spectra in a) with BEM calculations in b) reproduced from [85]. Measured structure had a shape of equilateral silver nanoprisms with 78-nm-long sides and spectra were measured for three different positions of the electron beam (A, B, C) as we can see in the inset of part b). In part a) containing the measured data it is possible to observe spectra D corresponding to energy loss of the mica substrate that was proven to have almost no influence on the EEL spectra of the particle. Energies of the peaks correspond to excitation of different modes in the nanoparticle and are quite well reproduced by the simulated spectra in b).

4. Interaction of spherical particles with an electron beam

The beginning of this chapter is devoted to the presentation of analytical expressions for the electromagnetic field outside and inside the spherical particle arising due to the interaction with fast electrons [18] from which the fully retarded expression for the electron energy loss probability is derived. We will also provide a comparison of the fields and EEL spectra calculated analytically and numerically using the MNPBEM toolbox [51]. In the end of this chapter, we analyse calculated EEL probabilities for different parameters and include non-locality to the EELS calculations, too.

The analytical expressions for the fields inside and outside the sphere are very important for us since they will be used for calculations of the forces in the following chapter.

4.1. Multipole expansion of the field produced by fast electron

We already know the analytical expressions for the electromagnetic field produced by a bare electron in infinite space both in the frequency and time domain [recall Eqs. (3.1)–(3.6)], but solution of the induced field produced as a response of a spherical particle is rather difficult to obtain. For this purpose it is necessary to express the incident external field brought by the electron in a way suitable to the spherical geometry of our problem.

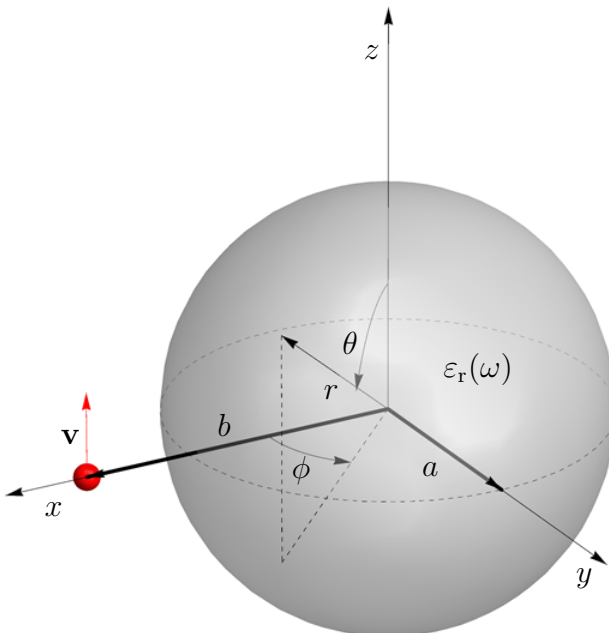


Figure 4.1: Scheme of a metallic sphere with radius a characterized by a relative permittivity $\varepsilon_r(\omega)$ and an electron with velocity v (plotted as a small red sphere) moving nearby. Current position of the depicted electron is $\mathbf{r}_t = (b, 0, 0)$ with respect to the sphere centered at the origin of the coordinate system. Spherical coordinates (r, θ, ϕ) , which will be utilized, are also specified.

García de Abajo [18] exploited the multipole expansion and by matching the field components on the sphere boundary obtained closed expressions for induced scalar functions from which the fields outside and inside the sphere can be derived. We present here only

4.1. MULTIPOLE EXPANSION OF THE FIELD PRODUCED BY FAST ELECTRON

the main results, details of the derivation can be found in Appendix C. In the following, we use atomic units (see Appendix B).

Without loss of generality, we assume the sphere of radius a and the electron moving in the positive z direction [expression for its velocity vector reads $\mathbf{v} = (0, 0, v)$] at the impact parameter $\mathbf{r}_0 = (b, \phi_0 = 0, z_0 = 0)$, here expressed in cylindrical coordinates, as sketched in Fig. 4.1. The trajectory is assumed to be a straight line as a deflection experienced by the electron is negligible [17, 88].

The external electric and magnetic fields produced by the fast electron can be in a spherical shell domain $a < r < b$ with use of the expansion written as

$$\begin{aligned}
\mathbf{E}^{\text{ext,out}}(\mathbf{r}, \omega) = & \mathbf{e}_r \frac{-2\pi i\omega}{c^2\gamma} \sum_{l=1}^{\infty} \sum_{m=-l}^l \frac{j_l(kr)}{kr} B_{l,m} K_m \left(\frac{\omega b}{v\gamma} \right) Y_{l,m}(\theta, \phi) \\
& + \mathbf{e}_\theta \left\{ \frac{4\pi i\omega v}{c^3} \sum_{l=1}^{\infty} \sum_{m=-l}^l \frac{m^2}{l(l+1)\sin\theta} j_l(kr) A_{l,m}^+ K_m \left(\frac{\omega b}{v\gamma} \right) Y_{l,m}(\theta, \phi) \right. \\
& + \frac{2\pi i\omega}{c^2\gamma} \sum_{l=1}^{\infty} \sum_{m=-l}^l \frac{B_{l,m}}{l(l+1)} K_m \left(\frac{\omega b}{v\gamma} \right) \left[(l+1) \frac{j_l(kr)}{kr} - j_{l+1}(kr) \right] \\
& \times \left[\frac{(l+1)\cos\theta}{\sin\theta} Y_{l,m}(\theta, \phi) - \frac{(l-m+1)}{\sin\theta} \frac{\alpha_{l,m}}{\alpha_{l+1,m}} Y_{l+1,m}(\theta, \phi) \right] \Big\} \\
& + \mathbf{e}_\phi \left\{ \frac{4\pi\omega v}{c^3} \sum_{l=1}^{\infty} \sum_{m=-l}^l \frac{m}{l(l+1)} j_l(kr) A_{l,m}^+ K_m \left(\frac{\omega b}{v\gamma} \right) \right. \\
& \times \left[\frac{(l+1)\cos\theta}{\sin\theta} Y_{l,m}(\theta, \phi) - \frac{(l-m+1)}{\sin\theta} \frac{\alpha_{l,m}}{\alpha_{l+1,m}} Y_{l+1,m}(\theta, \phi) \right] \\
& + \frac{2\pi\omega}{c^2\gamma} \sum_{l=1}^{\infty} \sum_{m=-l}^l \frac{m}{l(l+1)\sin\theta} B_{l,m} K_m \left(\frac{\omega b}{v\gamma} \right) Y_{l,m}(\theta, \phi) \\
& \times \left. \left[(l+1) \frac{j_l(kr)}{kr} - j_{l+1}(kr) \right] \right\} \tag{4.1}
\end{aligned}$$

and

$$\begin{aligned}
\mathbf{B}^{\text{ext,out}}(\mathbf{r}, \omega) = & \mathbf{e}_r \frac{-4\pi i\omega v}{c^3} \sum_{l=1}^{\infty} \sum_{m=-l}^l m \frac{j_l(kr)}{kr} A_{l,m}^+ K_m \left(\frac{\omega b}{v\gamma} \right) Y_{l,m}(\theta, \phi) \\
& + \mathbf{e}_\theta \left\{ \frac{-2\pi i\omega}{c^2\gamma} \sum_{l=1}^{\infty} \sum_{m=-l}^l \frac{m}{l(l+1)\sin\theta} j_l(kr) B_{l,m} K_m \left(\frac{\omega b}{v\gamma} \right) Y_{l,m}(\theta, \phi) \right. \\
& + \frac{4\pi i\omega v}{c^3} \sum_{l=1}^{\infty} \sum_{m=-l}^l \frac{m}{l(l+1)} A_{l,m}^+ K_m \left(\frac{\omega b}{v\gamma} \right) \left[(l+1) \frac{j_l(kr)}{kr} - j_{l+1}(kr) \right] \\
& \times \left[\frac{(l+1)\cos\theta}{\sin\theta} Y_{l,m}(\theta, \phi) - \frac{(l-m+1)}{\sin\theta} \frac{\alpha_{l,m}}{\alpha_{l+1,m}} Y_{l+1,m}(\theta, \phi) \right] \Big\} \\
& - \mathbf{e}_\phi \left\{ \frac{2\pi\omega}{c^2\gamma} \sum_{l=1}^{\infty} \sum_{m=-l}^l \frac{B_{l,m}}{l(l+1)} j_l(kr) K_m \left(\frac{\omega b}{v\gamma} \right) \right. \tag{4.2}
\end{aligned}$$

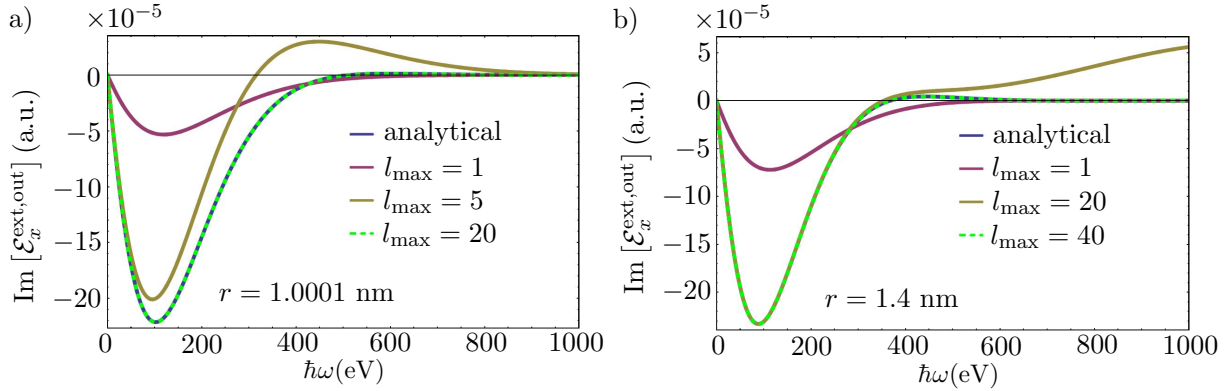


Figure 4.2: Comparison of the imaginary part of the external electric field component $\mathcal{E}_x^{\text{ext,out}}$ calculated analytically and from the multipole expansion with different number of considered multipoles l_{\max} . The electron is passing at the impact parameter $b = 1.5$ nm. In a) the calculation is made for point ($r = 1.0001$ nm, $\theta = 135^\circ$, $\phi = 90^\circ$), in b) point closer to the electron trajectory ($r = 1.4$ nm, $\theta = 135^\circ$, $\phi = 90^\circ$) was used. The blue line marking the analytical solution is indistinguishable from the green dashed line which corresponds to the expansion using 20 multipoles in the case of the point further from the electron trajectory, and 40 multipoles when we are closer. Red curves denote calculations including only dipolar contribution, yellow curves are for 5 a) or 20 b) multipoles.

$$\begin{aligned}
 & \times \left[\frac{(l+1)\cos\theta}{\sin\theta} Y_{l,m}(\theta, \phi) - \frac{(l-m+1)}{\sin\theta} \frac{\alpha_{l,m}}{\alpha_{l+1,m}} Y_{l+1,m}(\theta, \phi) \right] \\
 & - \frac{4\pi\omega v}{c^3} \sum_{l=1}^{\infty} \sum_{m=-l}^l \frac{m^2}{l(l+1)\sin\theta} A_{l,m}^+ K_m \left(\frac{\omega b}{v\gamma} \right) Y_{l,m}(\theta, \phi) \\
 & \times \left[(l+1) \frac{j_l(kr)}{kr} - j_{l+1}(kr) \right] \Big\} ,
 \end{aligned}$$

where we exploit spherical Bessel functions $j_l(kr)$, modified Bessel functions of the second kind $K_m(\xi)$, spherical harmonics $Y_{l,m}(\theta, \phi)$, and expansion coefficients $A_{l,m}^+$ and $B_{l,m}$ [see Eqs. (C25) and (C34)]. The coefficients $\alpha_{l,m}$ are defined in Eq. (C6), γ is again the Lorentz factor. Notice that the spatial modulation of the fields is mostly given by the spherical Bessel functions which scale with radial distance from the spherical surface, whereas the angular dependence is contained in the spherical harmonics and goniometric functions. The impact parameter b is included in the modified Bessel functions, which are for the zeroth and the first order plotted in Fig. 3.2.

The expansion coefficients $A_{l,m}^+$ and $B_{l,m}$ depend exclusively on the electron velocity and together with the functions $K_m(\xi)$ act as weights for excitation of different modes, which is intimately related to the velocity and the impact parameter of the impinging electron.

It should be remarked that the expanded fields in Eqs. (4.1) and (4.2) contain infinite summations, however, in real calculations the summation is restricted to a finite number l_{\max} . To obtain reliable results, the number of multipoles has to be sufficiently large. This can be tested on an illustrative example: we assume the electron passing at the impact parameter $b = 1.5$ nm with respect to the origin. We calculate the external fields, the electron is carrying, at two points: the first one is situated further from the electron

4.2. MULTIPOLE EXPANSION OF THE INDUCED FIELDS OUTSIDE THE SPHERE

at coordinates ($r = 1.0001$ nm, $\theta = 135^\circ$, $\phi = 90^\circ$), and the second one closer to the trajectory at ($r = 1.4$ nm, $\theta = 135^\circ$, $\phi = 90^\circ$). We can then directly compare the fields calculated from the multipole expansion with the analytical expressions (3.5) and (3.6). In Fig. 4.2 we plot such a comparison for x component of the imaginary part of the electric field $\mathcal{E}_x^{\text{ext,out}}$.

We can notice that for points further from the trajectory, which means closer to the origin, excellent agreement is achieved for quite small number of multipoles over all energies (with $l_{\max} = 20$ the results obtained from the expansions are indistinguishable from the analytical ones). If we consider points that are located very close to the trajectory we have to employ much more multipoles, in this case $l_{\max} = 40$ was used to get excellent agreement at the selected frequency range. For even higher energies than we considered, more multipoles have to be employed in the case of the point closer to the trajectory.

4.2. Multipole expansion of the induced fields outside the sphere

The complete expressions for the induced fields outside the sphere are found to be (for complete derivation see Appendix C)

$$\begin{aligned}
\mathcal{E}^{\text{ind,out}}(\mathbf{r}, \omega) = & \mathbf{e}_r \frac{2\pi\omega}{c^2\gamma} \sum_{l=1}^{\infty} \sum_{m=-l}^l t_l^E \frac{h_l^{(1)}(kr)}{kr} B_{l,m} K_m \left(\frac{\omega b}{v\gamma} \right) Y_{l,m}(\theta, \phi) \\
& - \mathbf{e}_\theta \left\{ \frac{4\pi\omega v}{c^3} \sum_{l=1}^{\infty} \sum_{m=-l}^l \frac{t_l^M m^2}{l(l+1)\sin\theta} h_l^{(1)}(kr) A_{l,m}^+ K_m \left(\frac{\omega b}{v\gamma} \right) Y_{l,m}(\theta, \phi) \right. \\
& + \frac{2\pi\omega}{c^2\gamma} \sum_{l=1}^{\infty} \sum_{m=-l}^l \frac{t_l^E}{l(l+1)} B_{l,m} K_m \left(\frac{\omega b}{v\gamma} \right) \left[(l+1) \frac{h_l^{(1)}(kr)}{kr} - h_{l+1}^{(1)}(kr) \right] \\
& \times \left. \left[\frac{(l+1)\cos\theta}{\sin\theta} Y_{l,m}(\theta, \phi) - \frac{(l-m+1)}{\sin\theta} \frac{\alpha_{l,m}}{\alpha_{l+1,m}} Y_{l+1,m}(\theta, \phi) \right] \right\} \quad (4.3) \\
& + \mathbf{e}_\phi \left\{ \frac{4\pi i\omega v}{c^3} \sum_{l=1}^{\infty} \sum_{m=-l}^l \frac{t_l^M m}{l(l+1)} h_l^{(1)}(kr) A_{l,m}^+ K_m \left(\frac{\omega b}{v\gamma} \right) \right. \\
& \times \left. \left[\frac{(l+1)\cos\theta}{\sin\theta} Y_{l,m}(\theta, \phi) - \frac{(l-m+1)}{\sin\theta} \frac{\alpha_{l,m}}{\alpha_{l+1,m}} Y_{l+1,m}(\theta, \phi) \right] \right\} \\
& + \frac{2\pi i\omega}{c^2\gamma} \sum_{l=1}^{\infty} \sum_{m=-l}^l \frac{t_l^E m}{l(l+1)\sin\theta} B_{l,m} K_m \left(\frac{\omega b}{v\gamma} \right) Y_{l,m}(\theta, \phi) \\
& \times \left. \left[(l+1) \frac{h_l^{(1)}(kr)}{kr} - h_{l+1}^{(1)}(kr) \right] \right\},
\end{aligned}$$

and

$$\mathcal{B}^{\text{ind,out}}(\mathbf{r}, \omega) = \mathbf{e}_r \frac{4\pi\omega v}{c^3} \sum_{l=1}^{\infty} \sum_{m=-l}^l t_l^M m \frac{h_l^{(1)}(kr)}{kr} A_{l,m}^+ K_m \left(\frac{\omega b}{v\gamma} \right) Y_{l,m}(\theta, \phi)$$

4. INTERACTION OF SPHERICAL PARTICLES WITH AN ELECTRON BEAM

$$\begin{aligned}
& + \mathbf{e}_\theta \left\{ \frac{2\pi\omega}{c^2\gamma} \sum_{l=1}^{\infty} \sum_{m=-l}^l \frac{t_l^E m}{l(l+1)\sin\theta} h_l^{(1)}(kr) B_{l,m} K_m \left(\frac{\omega b}{v\gamma} \right) Y_{l,m}(\theta, \phi) \right. \\
& - \frac{4\pi\omega v}{c^3} \sum_{l=1}^{\infty} \sum_{m=-l}^l \frac{t_l^M m}{l(l+1)} A_{l,m}^+ K_m \left(\frac{\omega b}{v\gamma} \right) \left[(l+1) \frac{h_l^{(1)}(kr)}{kr} - h_{l+1}^{(1)}(kr) \right] \\
& \times \left. \left[\frac{(l+1)\cos\theta}{\sin\theta} Y_{l,m}(\theta, \phi) - \frac{(l-m+1)}{\sin\theta} \frac{\alpha_{l,m}}{\alpha_{l+1,m}} Y_{l+1,m}(\theta, \phi) \right] \right\} \quad (4.4) \\
& - \mathbf{e}_\phi \left\{ \frac{2\pi i\omega}{c^2\gamma} \sum_{l=1}^{\infty} \sum_{m=-l}^l \frac{t_l^E}{l(l+1)} h_l^{(1)}(kr) B_{l,m} K_m \left(\frac{\omega b}{v\gamma} \right) \right. \\
& \times \left. \left[\frac{(l+1)\cos\theta}{\sin\theta} Y_{l,m}(\theta, \phi) - \frac{(l-m+1)}{\sin\theta} \frac{\alpha_{l,m}}{\alpha_{l+1,m}} Y_{l+1,m}(\theta, \phi) \right] \right\} \\
& - \frac{4\pi i\omega v}{c^3} \sum_{l=1}^{\infty} \sum_{m=-l}^l \frac{t_l^M m^2}{l(l+1)\sin\theta} A_{l,m}^+ K_m \left(\frac{\omega b}{v\gamma} \right) Y_{l,m}(\theta, \phi) \\
& \times \left. \left[(l+1) \frac{h_l^{(1)}(kr)}{kr} - h_{l+1}^{(1)}(kr) \right] \right\}.
\end{aligned}$$

The expanded induced fields are very similar to the external fields (4.1) and (4.2) except for spherical Bessel functions which are now replaced by spherical Hankel functions due to the change from incoming to outgoing waves, and appearance of the scattering coefficients $t_l^{M,E}$. For the case of a non-magnetic sphere (when $\mu_{in} = \mu = \mu_0$) they are expressed as

$$t_l^M = (-i) \frac{-j_l(ka)[k_{in} a j_l(k_{in} a)]' + j_l(k_{in} a)[k a j_l(ka)]'}{h_l^{(1)}(ka)[k_{in} a j_l(k_{in} a)]' - j_l(k_{in} a)[k a h_l^{(1)}(ka)]'}, \quad (4.5)$$

$$t_l^E = (-i) \frac{-j_l(ka)[k_{in} a j_l(k_{in} a)]' + \varepsilon_r(\omega) j_l(k_{in} a)[k a j_l(ka)]'}{h_l^{(1)}(ka)[k_{in} a j_l(k_{in} a)]' - \varepsilon_r(\omega) j_l(k_{in} a)[k a h_l^{(1)}(ka)]'}, \quad (4.6)$$

where $k_{in}(\omega) = \sqrt{\varepsilon_r(\omega)}\omega/c$ is a magnitude of the wave vector inside the sphere.

The total fields outside the sphere are then expressed as a superposition of the external fields brought by the moving electron and the fields induced as the response of the sphere to the external perturbation:

$$\mathbf{E}^{out} = \mathbf{E}^{ext,out} + \mathbf{E}^{ind,out} \quad \text{and} \quad \mathbf{B}^{out} = \mathbf{B}^{ext,out} + \mathbf{B}^{ind,out}, \quad (4.7)$$

which holds both in the frequency and the time domain.

Now, we compare the induced fields outside the sphere with the numerical calculation. We assumed an aluminium sphere with radius $a = 1$ nm, 120 keV electron passing at an impact parameter $b = 1.5$ nm, and a point ($r = 1.0001$ nm, $\theta = 27^\circ$, $\phi = 60^\circ$) where the field was evaluated. In the multipole expansion, the convergence was obtained $l_{max} = 20$ multipoles. The numerical computation was performed within the MNPBEM toolbox, where we used a fully retarded BEM solver and considered different numbers of vertices corresponding to triangular elements which discretize the spherical surface, specifically 144 and 1225 vertices as shown in Fig. 4.3 a).

The results we have obtained for the chosen parameters are plotted in Figs. 4.3 b) and c). To illustrate behaviour of the numerical solution we have taken the real part of the

4.3. TOTAL FIELDS INSIDE THE SPHERE

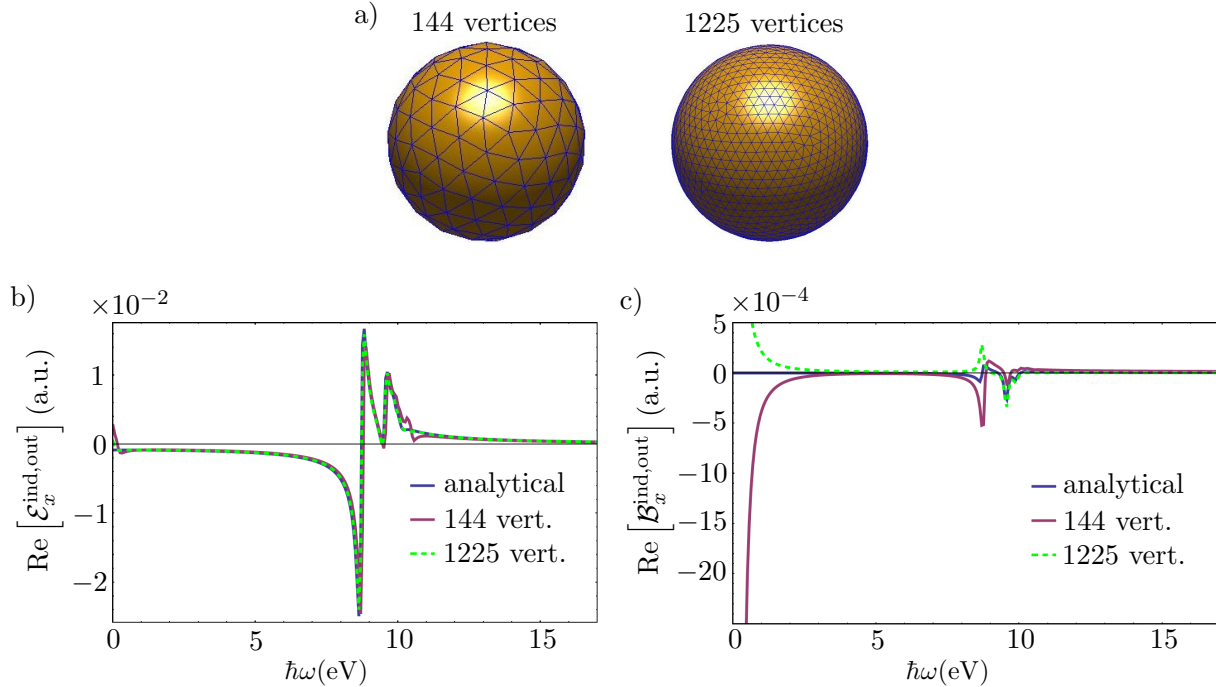


Figure 4.3: a) Illustration of the surface discretization used in the numerical calculations. Comparison of the induced electric field outside the aluminium sphere b) and the magnetic field c) calculated from the analytical expressions (4.3) and (4.4) (blue line), with the numerical results obtained from MNPBEM toolbox with use of different number of vertices (red and green dashed lines). Only the real part of x component is plotted. We used parameters $a = 1$ nm, $b = 1.5$ nm, 120 keV electron, and the point of the field evaluation ($r = 1.0001$ nm, $\theta = 27^\circ$, $\phi = 60^\circ$).

electric and magnetic field x component. In the case of the electric field plotted in part 4.3 b) it seems that with increasing number of the vertices, we obtain better agreement with the analytical solution – the green dashed line corresponding to the numerical results is overlapping the blue line representing the analytical solution. Unfortunately, this holds particularly for the field components $\mathcal{E}_x^{\text{ind,out}}$, $\mathcal{B}_y^{\text{ind,out}}$ and $\mathcal{B}_z^{\text{ind,out}}$. In Fig. 4.3 c) we can see that for the component $\mathcal{B}_x^{\text{ind,out}}$ the numerical results are not converged, even for quite large number of vertices.

Such a troublesome convergence is related especially to the point we have chosen for the field evaluation. As it is extremely close to the surface of the sphere, we would need much higher number of vertices to get reliable numerical results. This is probably also the reason of the artefacts that can be observed at very low energies, which is best observable in the case of $\text{Re} [\mathcal{B}_x^{\text{ind,out}}]$. We can therefore conclude that the boundary element method is not a suitable method for calculation of the electromagnetic field in the vicinity of the discretized particles and the convergence has to be checked carefully.

4.3. Total fields inside the sphere

The explicit expression for the electric field inside the sphere expanded in the vector spherical functions reads

$$\begin{aligned}
 \mathcal{E}^{\text{in}}(\mathbf{r}, \omega) = & \mathbf{e}_r \frac{-2\pi i \omega}{c^2 \gamma} \sum_{l=1}^{\infty} \sum_{m=-l}^l s_l^{\text{E}} \frac{j_l(k_{\text{in}} r)}{k_{\text{in}} r} B_{l,m} K_m \left(\frac{\omega b}{v \gamma} \right) Y_{l,m}(\theta, \phi) \\
 & + \mathbf{e}_\theta \left\{ \frac{4\pi i \omega v}{c^3} \sum_{l=1}^{\infty} \sum_{m=-l}^l \frac{s_l^{\text{M}} m^2}{l(l+1)\sin\theta} j_l(k_{\text{in}} r) A_{l,m}^+ K_m \left(\frac{\omega b}{v \gamma} \right) Y_{l,m}(\theta, \phi) \right. \\
 & + \frac{2\pi i \omega}{c^2 \gamma} \sum_{l=1}^{\infty} \sum_{m=-l}^l \frac{s_l^{\text{E}}}{l(l+1)} B_{l,m} K_m \left(\frac{\omega b}{v \gamma} \right) \left[(l+1) \frac{j_l(k_{\text{in}} r)}{k_{\text{in}} r} - j_{l+1}(k_{\text{in}} r) \right] \\
 & \times \left. \left[\frac{(l+1)\cos\theta}{\sin\theta} Y_{l,m}(\theta, \phi) - \frac{(l-m+1)}{\sin\theta} \frac{\alpha_{l,m}}{\alpha_{l+1,m}} Y_{l+1,m}(\theta, \phi) \right] \right\} \quad (4.8) \\
 & + \mathbf{e}_\phi \left\{ \frac{4\pi \omega v}{c^3} \sum_{l=1}^{\infty} \sum_{m=-l}^l \frac{s_l^{\text{M}} m}{l(l+1)} j_l(k_{\text{in}} r) A_{l,m}^+ K_m \left(\frac{\omega b}{v \gamma} \right) \right. \\
 & \times \left. \left[\frac{(l+1)\cos\theta}{\sin\theta} Y_{l,m}(\theta, \phi) - \frac{(l-m+1)}{\sin\theta} \frac{\alpha_{l,m}}{\alpha_{l+1,m}} Y_{l+1,m}(\theta, \phi) \right] \right. \\
 & + \frac{2\pi \omega}{c^2 \gamma} \sum_{l=1}^{\infty} \sum_{m=-l}^l \frac{s_l^{\text{M}} m}{l(l+1)\sin\theta} B_{l,m} K_m \left(\frac{\omega b}{v \gamma} \right) Y_{l,m}(\theta, \phi) \\
 & \times \left. \left[(l+1) \frac{j_l(k_{\text{in}} r)}{k_{\text{in}} r} - j_{l+1}(k_{\text{in}} r) \right] \right\},
 \end{aligned}$$

while the magnetic field inside the sphere is found to be

$$\begin{aligned}
 \mathcal{B}^{\text{in}}(\mathbf{r}, \omega) = & \mathbf{e}_r \frac{-4\pi i \omega v \sqrt{\varepsilon_r}}{c^3} \sum_{l=1}^{\infty} \sum_{m=-l}^l s_l^{\text{M}} \frac{j_l(k_{\text{in}} r)}{k_{\text{in}} r} A_{l,m}^+ K_m \left(\frac{\omega b}{v \gamma} \right) Y_{l,m}(\theta, \phi) \\
 & + \mathbf{e}_\theta \left\{ \frac{-2\pi i \omega \sqrt{\varepsilon_r}}{c^2 \gamma} \sum_{l=1}^{\infty} \sum_{m=-l}^l \frac{s_l^{\text{E}} m}{l(l+1)\sin\theta} j_l(k_{\text{in}} r) B_{l,m} K_m \left(\frac{\omega b}{v \gamma} \right) Y_{l,m}(\theta, \phi) \right. \\
 & + \frac{4\pi i \omega v \sqrt{\varepsilon_r}}{c^3} \sum_{l=1}^{\infty} \sum_{m=-l}^l \frac{s_l^{\text{M}} m}{l(l+1)} A_{l,m}^+ K_m \left(\frac{\omega b}{v \gamma} \right) \left[(l+1) \frac{j_l(k_{\text{in}} r)}{k_{\text{in}} r} - j_{l+1}(k_{\text{in}} r) \right] \\
 & \times \left. \left[\frac{(l+1)\cos\theta}{\sin\theta} Y_{l,m}(\theta, \phi) - \frac{(n-m+1)}{\sin\theta} \frac{\alpha_{l,m}}{\alpha_{l+1,m}} Y_{l+1,m}(\theta, \phi) \right] \right\} \quad (4.9) \\
 & - \mathbf{e}_\phi \left\{ \frac{2\pi \omega \sqrt{\varepsilon_r}}{c^2 \gamma} \sum_{l=1}^{\infty} \sum_{m=-l}^l s_l^{\text{E}} \frac{B_{l,m}}{l(l+1)} j_l(k_{\text{in}} r) K_m \left(\frac{\omega b}{v \gamma} \right) \right. \\
 & \times \left. \left[\frac{(l+1)\cos\theta}{\sin\theta} Y_{l,m}(\theta, \phi) - \frac{(l-m+1)}{\sin\theta} \frac{\alpha_{l,m}}{\alpha_{l+1,m}} Y_{l+1,m}(\theta, \phi) \right] \right. \\
 & - \frac{4\pi \omega v \sqrt{\varepsilon_r}}{c^3} \sum_{l=1}^{\infty} \sum_{m=-l}^l \frac{s_l^{\text{M}} m^2}{l(l+1)\sin\theta} A_{l,m}^+ K_m \left(\frac{\omega b}{v \gamma} \right) Y_{l,m}(\theta, \phi) \\
 & \times \left. \left[(l+1) \frac{j_l(k_{\text{in}} r)}{k_{\text{in}} r} - j_{l+1}(k_{\text{in}} r) \right] \right\},
 \end{aligned}$$

4.3. TOTAL FIELDS INSIDE THE SPHERE

where the scattering coefficients for the field inside are expressed as:

$$s_l^M = \frac{-j_l(ka)[kah_l^{(1)}(ka)]' + h_l^{(1)}(ka)[kaj_l(ka)]'}{h_l^{(1)}(ka)[k_{\text{in}}aj_l(k_{\text{in}}a)]' - j_l(k_{\text{in}}a)[kah_l^{(1)}(ka)]'}, \quad (4.10)$$

$$s_l^E = \sqrt{\varepsilon_r(\omega)} \frac{-j_l(ka)[kah_l^{(1)}(ka)]' + h_l^{(1)}(ka)[kaj_l(ka)]'}{h_l^{(1)}(ka)[k_{\text{in}}aj_l(k_{\text{in}}a)]' - \varepsilon_r(\omega)j_l(k_{\text{in}}a)[kah_l^{(1)}(ka)]'}. \quad (4.11)$$

We should remark that spherical Hankel functions are now again replaced with spherical Bessel functions. Furthermore, in the expressions (4.8) and (4.9) the wave vector inside the sphere appears.

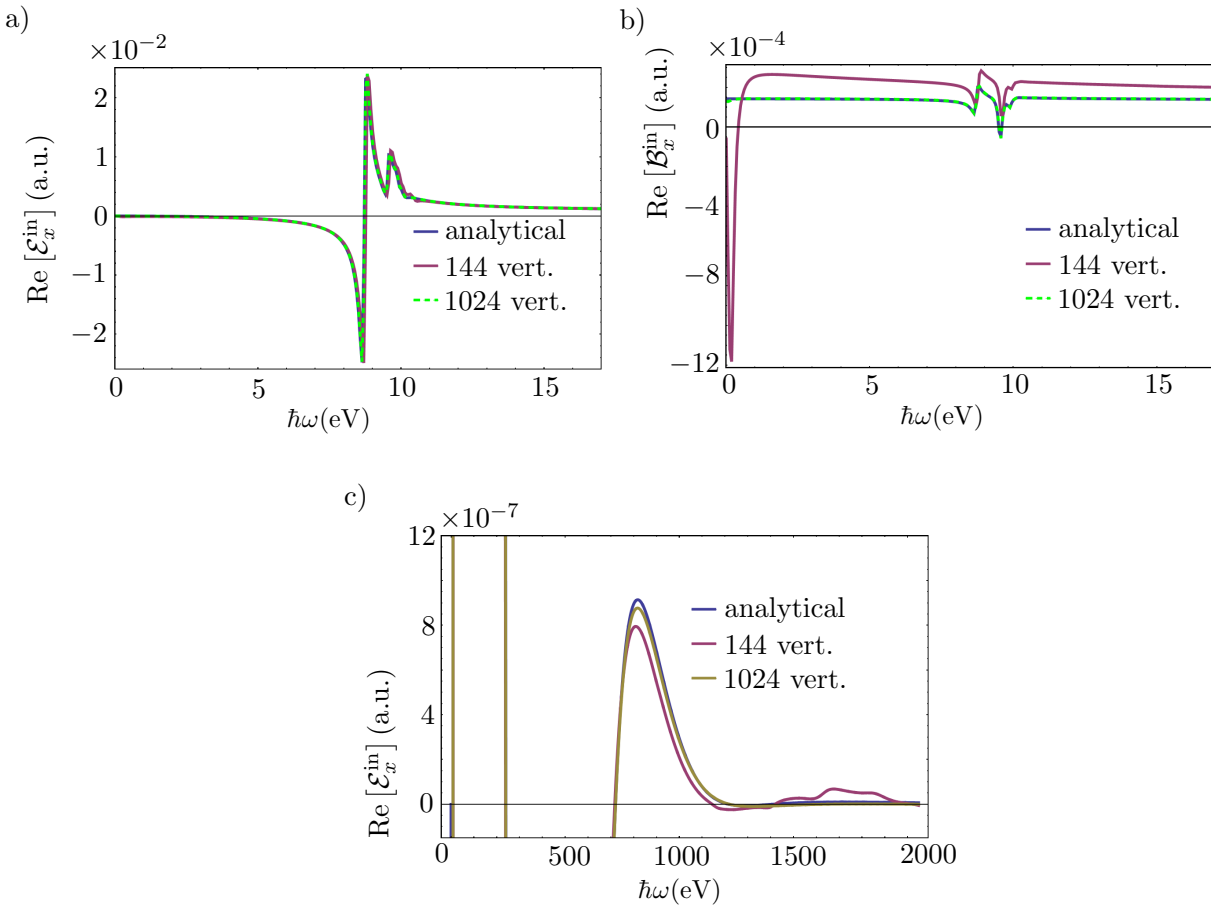


Figure 4.4: Comparison of the total electric field inside the aluminium sphere a) and the magnetic field b), respectively, calculated from the analytical expressions (4.8) and (4.9) (blue lines), with the numerical results obtained from the MNPBEM toolbox with use of a different number of vertices (red and green dashed lines). Only the real part of x component is plotted. We used parameters $a = 1$ nm, $b = 1.5$ nm, 120 keV electron, and the point of the field evaluation ($r = 0.85$ nm, $\theta = 27^\circ$, $\phi = 60^\circ$). In c) we plot the $\text{Re} [\mathcal{E}_x^{\text{in}}]$ for the whole considered energy range.

Similarly as in the case of the induced field outside the sphere we compare the analytical results [Eqs. (4.8) and (4.9)] with the numerical boundary element method calculations.

4. INTERACTION OF SPHERICAL PARTICLES WITH AN ELECTRON BEAM

In Fig. 4.4 a) and b) we again plot the frequency dependence of the components $\text{Re}[\mathcal{E}_x^{\text{in}}]$ and $\text{Re}[\mathcal{B}_x^{\text{in}}]$, respectively, in this case for the point ($r = 0.85$ nm, $\theta = 27^\circ$, $\phi = 60^\circ$). Since now we are further from the aluminium sphere-vacuum boundary and the convergence is clearly reached for all the components. For more than 1000 vertices, we have obtained almost perfect match with the analytical result.

In part 4.4 c), the $\text{Re}[\mathcal{E}_x^{\text{in}}]$ component is plotted over a wider energy range, where we see some discrepancies, but several orders of magnitude smaller than the features appearing around 10 eV. We should also note that at these lower frequencies, localized surface plasmons are excited as we will discuss more detail in the following section.

We have proven that the numerical calculations can be used quite safely when we are dealing with the points further from boundaries of the sphere. However, we still have to be sure we are using a sufficient number of the vertices and other disadvantage is that the numerical calculations are much more time consuming than use of the analytical solution.

4.4. Electron energy loss probability

Since we know the induced fields acting back on the moving electron, it is possible to calculate the loss probability Γ_{EELS} according to Eq. (3.9). When we substitute there the induced field, we can split the loss probability related to the magnetic modes (expressed in atomic units):

$$\Gamma_{\text{EELS}}^{\text{M}}(\omega) = \sum_{l=1}^{\infty} \sum_{m=-l}^l \frac{mv}{\pi\omega^2} K_m \left(\frac{\omega b}{v\gamma} \right) \text{Re} \left[(A_{l,m}^+)^* i^{-l} \psi_{l,m}^{\text{M,ind,out}} \right], \quad (4.12)$$

and the loss probability due to the electric modes

$$\Gamma_{\text{EELS}}^{\text{E}}(\omega) = \sum_{l=1}^{\infty} \sum_{m=-l}^l \frac{c}{2\pi\omega^2\gamma} K_m \left(\frac{\omega b}{v\gamma} \right) \text{Re} \left[(B_{l,m}^+)^* i^{-l} \psi_{l,m}^{\text{E,ind,out}} \right], \quad (4.13)$$

where the scalar magnetic and electric functions $\psi_{l,m}^{\nu,\text{ind,out}}$, respectively, can be found in Appendix C, see Eqs. (C40) and (C41). Now we can write down the total loss probability characterizing the retarded spectral response of a dielectric sphere in SI units as a sum of the electric and magnetic contribution:

$$\Gamma_{\text{EELS}} = \Gamma_{\text{EELS}}^{\text{M}} + \Gamma_{\text{EELS}}^{\text{E}} = \frac{e^2}{c\hbar\omega} \sum_{l=1}^{\infty} \sum_{m=-l}^l K_m^2 \left(\frac{\omega b}{v\gamma} \right) [C_{l,m}^{\text{M}} \text{Im}[t_l^{\text{M}}] + C_{l,m}^{\text{E}} \text{Im}[t_l^{\text{E}}]], \quad (4.14)$$

where we define the coefficients

$$C_{l,m}^{\text{M}} = \frac{1}{l(l+1)} \left| \frac{2mv}{c} A_{l,m}^+ \right|^2 \quad C_{l,m}^{\text{E}} = \frac{1}{l(l+1)} \left| \frac{1}{\gamma} B_{l,m} \right|^2. \quad (4.15)$$

We can notice that the loss probability is dependent on all the input parameters: the sphere radius a is included in the scattering coefficients t_l^{E} and t_l^{M} , the impact parameter b is contained in an argument of the modified Bessel functions, and the magnitude of the velocity v appears both in the coefficients $C_{l,m}^{\text{E}}$, $C_{l,m}^{\text{M}}$ and in the Bessel functions. The spectral dependence is obviously in a denominator of the prefactor and in the argument

4.4. ELECTRON ENERGY LOSS PROBABILITY

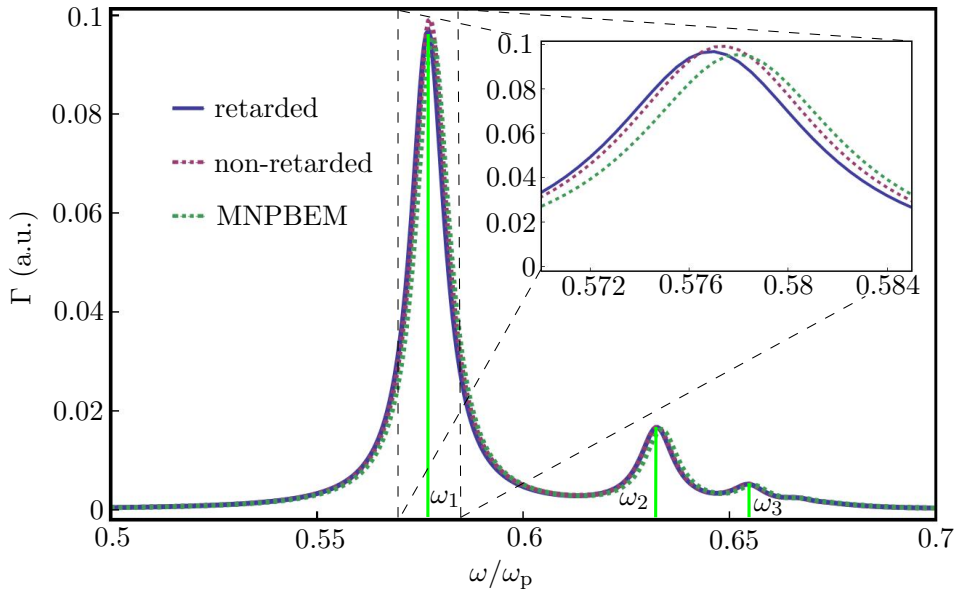


Figure 4.5: The electron energy loss spectra for an aluminium sphere with radius $a = 1$ nm and 120 keV electron passing at $b = 1.5$ nm calculated analytically by a retarded (blue line) and non-retarded (red dashed line) approach. Spectrum obtained numerically by the BEM approach is also plotted (green dashed line). We also highlight the first three resonance frequencies. In the inset we can see the detail of the first peak, where a slight mismatch between the spectra is apparent.

of modified Bessel functions. However, peaks that can arise in the energy loss spectra are coming from poles of the complex coefficients t_l^E and t_l^M , where the wave vector k_{in} dependent on a dielectric function characterizing the material response is contained in arguments of the special functions.

In the nonrelativistic limit, the quasi-static Eq. (3.15) is recovered after some algebra. We can easily compare the loss probability calculated using the fully retarded expression (4.14), the non-retarded loss probability (3.15) and results calculated numerically by boundary element approach utilizing the MNPBEM toolbox [51].

Fig. 4.5 shows the electron energy loss spectra for an electron with energy 120 keV ($v = 0.587 c$) passing by an aluminium sphere with radius $a = 1$ nm at the impact parameter $b = 1.5$ nm. Aluminium is characterized by the Drude dielectric function with parameters taken from table 2.1. We can distinguish the most intensive peak at energy $\approx 1/\sqrt{3} \hbar\omega_p = 8.72$ eV, which corresponds to the dipole mode energy (see Eq. (3.16) and assume $l = 1$). Then we see the quadrupole located at $\approx \sqrt{2/5} \hbar\omega_p = 9.55$ eV, the hexapole at $\approx \sqrt{3/7} \hbar\omega_p = 9.89$ eV and then mostly indistinguishable higher order modes forming the small "shoulder" above $0.66 \hbar\omega_p$.

The induced field magnitudes corresponding to these energies denoted in Fig. 4.5 by the green lines are plotted in Fig. 4.6, where we can directly see visualization of different modes just above the surface of our aluminium sphere. The electric field is shown in the upper row, whereas the magnetic field is underneath. The trajectory of the electron is schematically depicted by thin red lines. We can clearly resolve not only the symmetry of each mode, but the decreasing strength as well.

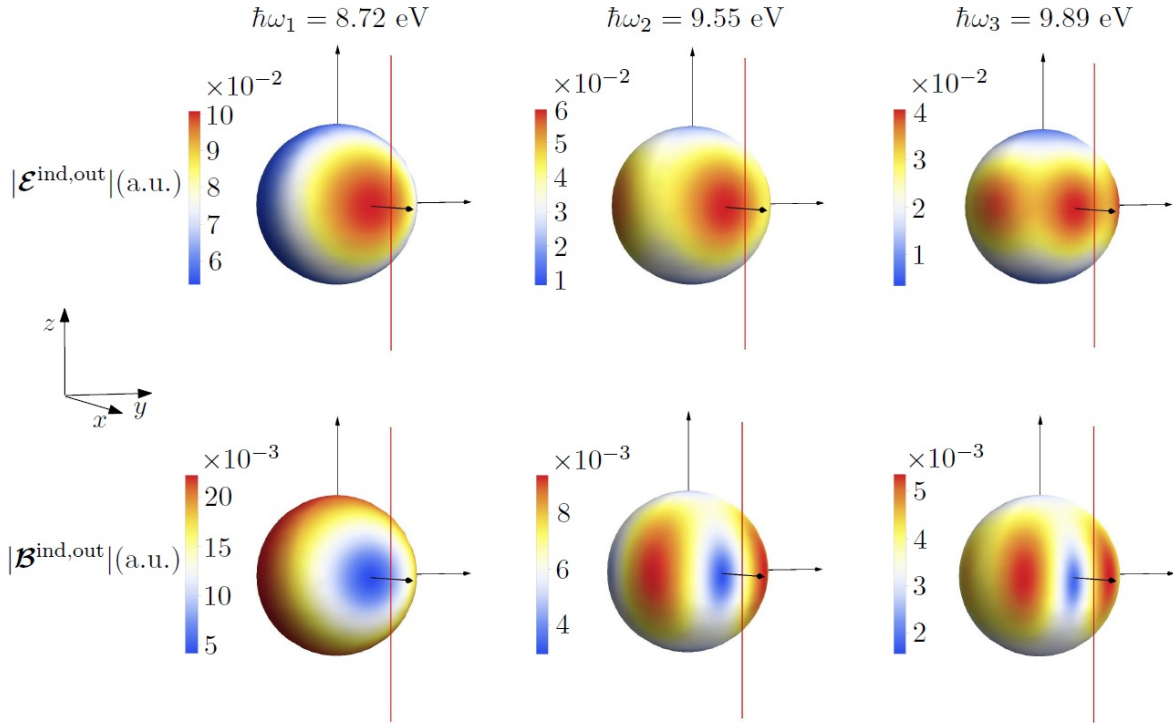


Figure 4.6: Visualization of the induced fields at the radial distance $r = 1.0001$ nm just above the surface of the aluminium sphere with radius $a = 1$ nm. The fields are plotted in the frequency domain for three different energies corresponding to the peaks in spectrum 4.5. Dipole, quadrupole and hexapole mode patterns are clearly resolved, in the upper row we show the magnitude of the electric field and in the lower row, the magnetic field magnitude is plotted. The electron trajectory is denoted by red lines. We also recall that the fields are evaluated using atomic units defined in Appendix B.

Notice that the analytically calculated retarded and non-retarded spectra 4.5 are almost equal for the chosen parameters – the sphere is very small and the electron velocity is not extremely relativistic, thus retardation effects are not so important. Within the numerical calculation in the MNPBEM toolbox, we discretized the sphere by 1444 triangular elements and used the retarded BEM solver. This gave us well agreeing results, but in the detail we can see that more elements should be added to obtain a perfect match with the analytically calculated retarded spectra.

In section 2.2, we have also discussed the non-classical effects which can appear e.g. when we deal with very small objects or when the probe electrons are closely approaching the nanostructures. The nanosphere can serve as a good demonstration of the hydrodynamic non-local model since it is possible to obtain an analytical solution for the non-local loss probability only by modifying the scattering coefficients (4.5) and (4.6) as presented in Ref. [61].

The comparison of the local and non-local loss probabilities for the same parameters as in the previous case ($a = 1$ nm, energy of electrons 120 keV) and the Fermi velocity 1.95×10^6 m/s [61] is plotted in Fig. 4.7, where we show 2D maps representing spectra for different impact parameters b . In part a) the local approximation was used and as we can

4.4. ELECTRON ENERGY LOSS PROBABILITY

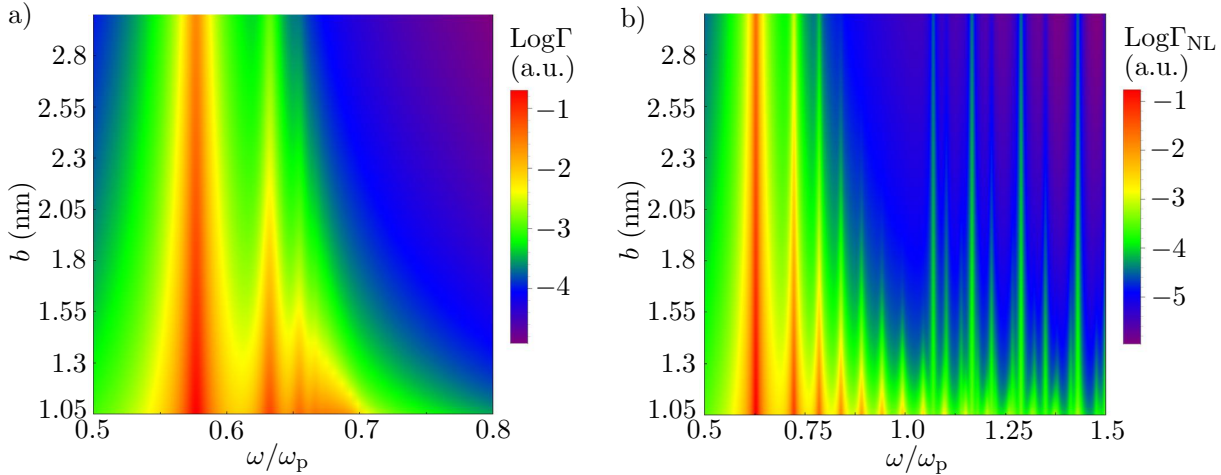


Figure 4.7: Local a) versus non-local b) electron energy loss probability spectra for an aluminium sphere characterized by Drude dielectric function (parameters were taken from table 2.1) with radius $a = 1$ nm, 120 keV electrons and range of impact parameters from 1.05 nm to 3 nm.

see, the peaks appear only below the plasma frequency and for mode index $l \rightarrow \infty$ their energies approach the planar limit represented by the surface plasmon frequency $\sqrt{2} \omega_p$.

It is intuitive that with the increasing impact parameter, the loss probability is decreasing, but it is more interesting to explore how the ratio of the excited modes strengths is evolving. In Fig. 4.7 we see that when the electron is closer, the ratio of the losses caused by excitation of the higher order modes to the lower modes is higher than for the electron trajectory further from the sphere. This is connected to large field gradients appearing at close trajectories, when the higher multipoles have larger weights in the expansion. On the contrary, when the electron is far, the external field is not varying so dramatically within volume of the sphere, thus lower order modes are preferentially excited.

The non-local loss probability corresponding to the hydrodynamic response is plotted in Fig. 4.7 b), again for varying impact parameters. In this case, the spectra look completely different than those for the local response even for quite large impact parameters. This is not so astonishing as very small dimensions of the sphere were considered in the calculations. The peaks are much better resolvable and even for higher order modes they do not overlap since the non-local resonance energies are more separated.

The most surprising in the non-local results is an appearance of the further peaks at frequencies higher than ω_p . This is caused by presence of the longitudinal fields which emerge inside of the non-local material of the sphere. As illustrated in picture 2.3, the charges are thus not situated only at the boundaries of the metal, but they start to penetrate inside, and the bulk plasmons resonances therefore appear above the plasma frequency.

So far, we were dealing with aluminium, which is nicely described by the Drude model. However, behaviour of other metals is more complicated. In the case of gold we have to be aware of interband transitions and collective modes of d -electrons, which significantly contribute to the response at high energies [89]. If we consider the fitted experimental

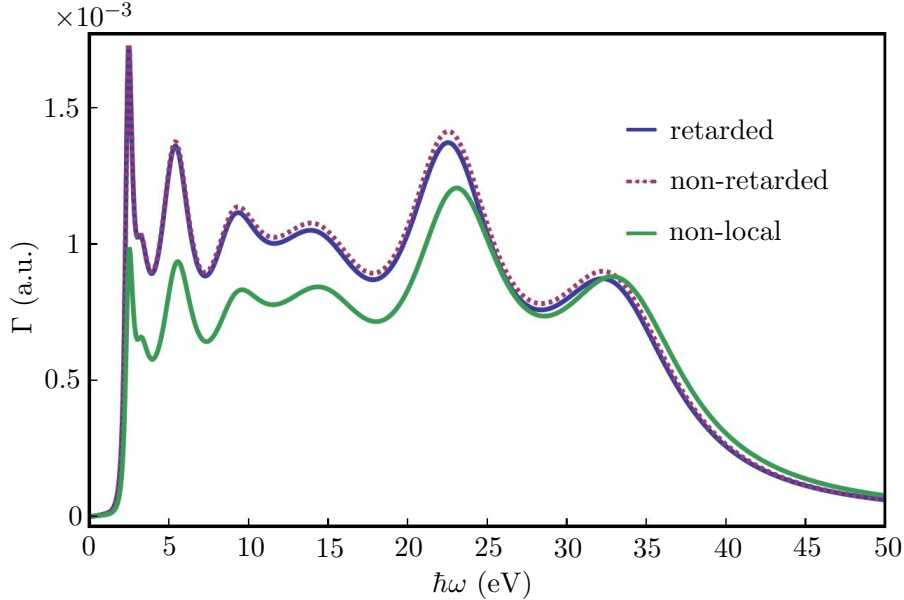


Figure 4.8: The electron energy loss spectra for a gold sphere with radius $a = 1$ nm and the 120 keV electron (velocity is $0.587 c$) passing at $b = 1.5$ nm calculated analytically by the retarded (blue line) and non-retarded (red dashed line) approach. The result obtained from the non-local calculation is plotted by the green line.

dielectric function of gold (see Fig. 2.2), it is not surprising that compared to aluminium, qualitatively different EEL spectra were obtained.

In Fig. 4.8 we show calculated retarded, non-retarded and non-local loss spectra corresponding to the parameters $a = 1$ nm, $b = 1.5$ nm and 120 keV electrons ($v = 0.587 c$). As we can see, all the spectra possess various peaks, where the most pronounced one situated at 2.5 eV is related to the excitations of localized surface plasmon modes. Since energies of the modes are very close to each other, it is not possible to resolve them as in the case of the aluminium nanosphere. Peaks at higher energies are associated with the mentioned interband transitions and the collective modes of d -electrons. Importantly, these excitations could be responsible for ejection of secondary electrons as their energies are sufficient to overcome the work function barrier [90].

If we compare the retarded and non-retarded results, they again match very well especially due to the small size of our object. The non-local spectrum is slightly blue-shifted, which was also observed for aluminium. Since the localized surface plasmon peak includes various modes with close energies, we cannot observe their separation as in the previous case of the non-local aluminium sphere, only reduced intensity and lower ratio with respect to high-energy peaks. However, more elaborate analysis on behaviour connected to the non-locality should be made.

We have also calculated retarded spectra for a bigger gold sphere with radius $a = 10$ nm for three different energies of the impinging electrons corresponding to velocities $v = 0.3/0.6/0.9 c$. The electrons are passing at the impact parameter $b = 11$ nm. We directly observe two main features with increasing velocity: the loss probability is reduced, and the ratio between intensity of the high-energy peaks and the peaks in lower energy region is higher. This can be readily understood when we realize that for electrons with larger velocities, interaction volume is reduced and high field gradients arise in their

4.4. ELECTRON ENERGY LOSS PROBABILITY

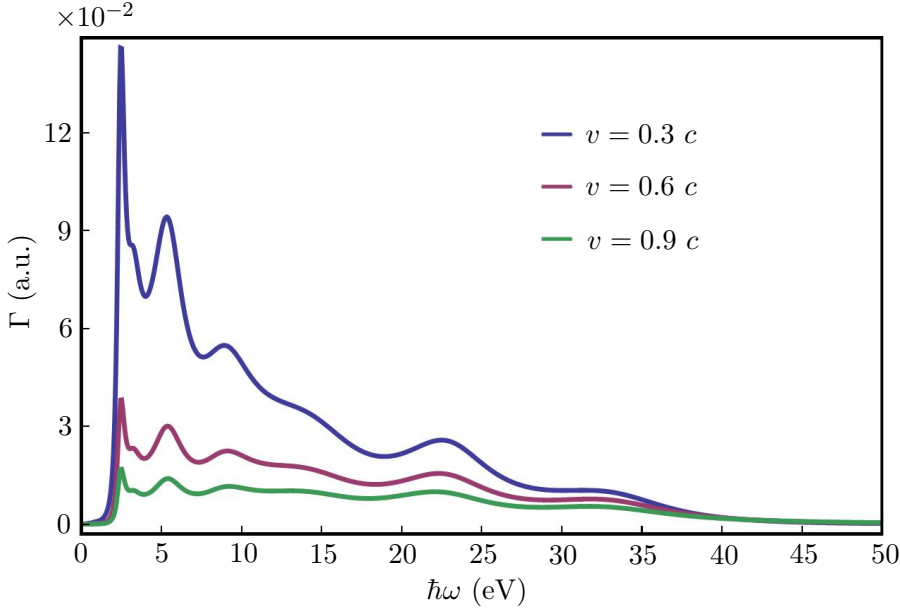


Figure 4.9: The electron energy loss spectra for a gold sphere with radius $a = 10$ nm and the impact parameter $b = 11$ nm calculated analytically from the retarded analytical expression. Spectra for three different velocities of incoming electrons are plotted.

vicinity. Similar effects were observed when we were changing the impact parameters of the electrons passing by the aluminium sphere.

In this section, we have analyzed how the spectral response of metallic nanospheres behaves. Besides other parameters, EEL spectrum strongly depends on the dielectric response of material: for aluminium, which is characterized only by the Drude term with small damping, we could nicely resolve peaks corresponding to the individual plasmonic modes (dipolar, quadrupolar,...). On the contrary, the response of gold is more complicated and the spectra contained not only the peak corresponding to the unresolvable localized surface plasmon modes, but also the strong high-energy contributions were observed.

Importantly, the energy losses we were calculating within this section correspond to a stopping of the electron along its trajectory which was considered to be a straight line. The EEL probability is thus directly related to a transfer of a longitudinal component of the mechanical momentum. Despite the fact that the influence of the transverse momentum component was neglected in the energy transfer, it cannot be neglected itself, as we will see in the next chapter.

5. Momentum transfer to a metallic sphere

The motivation of our study is connected with the phenomenon of nanoparticle repulsion/attraction by an electron beam illustrated in Fig. 5.1. In part a) we see a scheme of the experiment performed in a scanning transmission electron microscope (STEM) [12]. The 120 keV electron beam was scanned over a larger area on a sample containing gold particles sitting on a carbon membrane commonly used as a STEM sample substrate. When some smaller particle (1 – 2 nm in diameter), which is marked by the yellow circle, was observed, the scanning was periodically delayed for 20 % of the line scanning time at the left edge of the scanned area. Such a manipulation with the beam caused a movement of small gold nanoparticles as depicted in a sequence of images in Fig. 5.1 b). In the following, the distance of the beam from the center of the particle will be again denoted as the impact parameter.

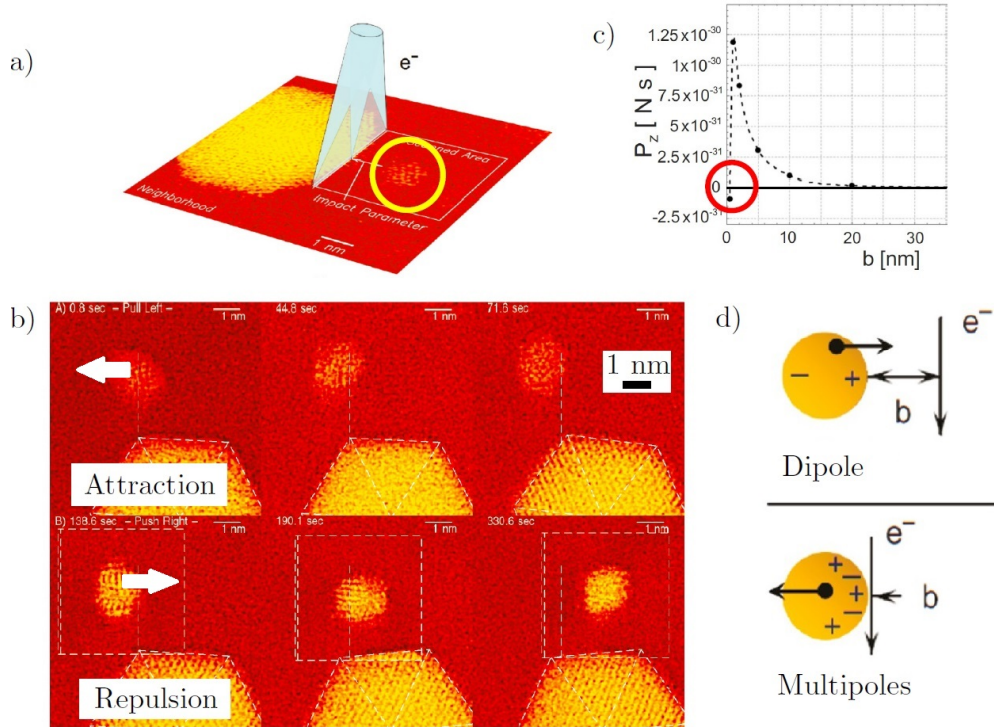


Figure 5.1: a) A scheme of an experiment in a scanning transmission electron microscope (STEM), where an electron beam is scanned over a larger area and delayed at the left edge of a sample consisting of a carbon membrane with gold nanoparticles evaporated on top of it. b) Demonstration of manipulation with a small gold nanoparticle of diameter 1.5 nm: in the upper row a "pulling" mechanism is recorded, whereas in the lower row "pushing" of the particle is shown, which takes place when small impact parameters are used. White arrows indicate the direction of motion. c) Calculation made for a Drude-type aluminium sphere ($a = 1$ nm and $b = 1.5$ nm) showing a dependence of the transverse component of a total momentum transfer on the impact parameter, reproduced from Ref. [16]. d) A scheme showing a possible explanation of the phenomenon. Pictures a), b) and d) were reproduced from Ref. [12] and modified.

5.1. MOMENTUM TRANSFER IN THE FREQUENCY DOMAIN

Surprisingly, two different regimes of the movement of the small spherical nanoparticle were observed. In the upper row, the sphere is pulled by the electron beam which is stopped at a moderate impact parameter ($b \approx 5$ nm) left from the particle. The direction of the small particle displacement is obvious from comparison with the previous image, where the larger sphere serves as a reference. The movement recorded in the lower row is completely reversed – the particle is repelled when the impact parameter $b \approx 1.5$ nm is used [12]. This ambiguous behaviour is not so easy to explain because according to the basic image charge concept the particle should always be attracted towards the electron.

A possible explanation of this effect was proposed by Reyes-Coronado *et al.* in Ref. [16], where the repulsion is claimed to be connected with more effective excitation of higher order modes when the electron impact parameter is very small. On the contrary, the attractive force acts on the particle in the case of the larger impact parameters. The authors support this claim by a calculation of the transverse momentum transfer to the spherical particle which is depicted in Fig. 5.1 c). The repulsion, observed as a negative value of the transferred transverse momentum, was obtained for a Drude-type nanosphere with radius $a = 1$ nm and the impact parameter $b = 1.5$ nm (following the notation used throughout this thesis). The qualitatively similar dependence was also achieved for gold nanoparticles characterized by experimental dielectric data. In Fig. 5.1 d) we can see a scheme showing the possible excitation of the higher order modes for the small impact parameter. For the electron passing further from the nanosphere, the dipolar mode particularly responsible for the attraction should dominate.

In this chapter, we first calculate and analyze the momentum transfer in the frequency domain as presented in Refs. [16, 17]. However, as we will show, these calculations represent only average effects of the complex dynamics of the particle in the time domain. Hence, our goal is to transform the fields into the time domain and to unravel the time dependent dynamical effects imposed by the passing electron on the nanoparticle. We briefly describe how the transformation to the time domain is performed and finally, we show and discuss the time dependence of the force exerted by the swift electron on the aluminium and gold sphere at different time scales. We will first explore, what is happening during the closest approach of the electron to the nanosphere which corresponds to units of attoseconds. Then we will analyze the forces associated to the localized surface plasmon decay appearing at femtoseconds after the electron flyby.

5.1. Momentum transfer in the frequency domain

The total momentum transfer can be obtained by integration of Eq. (1.25) over time which yields [16]

$$\mathbf{p} = \int_{-\infty}^{\infty} \frac{d}{dt} [\mathbf{p}_{\text{mech}}(t) + \mathbf{p}_{\text{field}}(t)] dt = \int_{-\infty}^{\infty} \frac{d\mathbf{p}_{\text{mech}}(t)}{dt} dt = \int_{-\infty}^{\infty} \iint_S \overleftrightarrow{\mathbf{T}}(\mathbf{r}, t) \cdot \mathbf{n} dS dt. \quad (5.1)$$

It should be emphasized that the field momentum contribution in Eq. (5.1) disappeared due to the integration over all times which can be understood as an averaging process. This is frequently exploited in the calculations of optical forces in the frequency domain dealing with a time-harmonic dependence of the applied external field [22, 91–94]. For

for this reason the subscript _{mech} is redundant and we will not use it within this section. The disappearance of the field momentum also simplifies the calculations as we have to perform only the surface integrals instead of the volume integration (i.e. the numerical calculations are much faster).

Considering the definition of the inverse Fourier transform (A5), delta distribution and changing the order of integration, the relation for the total momentum transfer can be further rewritten as

$$\begin{aligned} \mathbf{p} &= \int_{-\infty}^{\infty} \frac{1}{2\pi} \left[\int_{-\infty}^{\infty} \mathcal{F}_{\text{mech}}(\omega) \text{ext}(-i\omega t) d\omega \right] dt = \int_{-\infty}^{\infty} \mathcal{F}_{\text{mech}}(\omega) \int_{-\infty}^{\infty} \exp(-i\omega t) dt \frac{d\omega}{2\pi} \quad (5.2) \\ &= \int_{-\infty}^{\infty} \mathcal{F}_{\text{mech}}(\omega) \delta(\omega) d\omega = \mathcal{F}_{\text{mech}}(\omega = 0). \quad (5.3) \end{aligned}$$

The total momentum transfer will be now expressed with use of the Maxwell stress tensor formalism which can be modified similarly as in the previous case:

$$\mathbf{p} = \int_{-\infty}^{\infty} \left[\oint \overleftrightarrow{\mathbf{T}}(\mathbf{r}, t) \cdot \mathbf{n} dS \right] dt = \oint \left[\int_{-\infty}^{\infty} \overleftrightarrow{\mathbf{T}}(\mathbf{r}, t) dt \right] \cdot \mathbf{n} dS = \oint \overleftrightarrow{\mathbf{T}}(\mathbf{r}, \omega = 0) \cdot \mathbf{n} dS, \quad (5.4)$$

where the $\omega = 0$ component of the Maxwell stress tensor after substituting the definition (1.24) and exploiting the Rayleigh-Parseval theorem (A11) reads

$$\overleftrightarrow{\mathbf{T}}(\mathbf{r}, \omega = 0) = \frac{1}{\pi} \int_0^{\infty} \overleftrightarrow{\mathbf{T}}(\mathbf{r}, \omega) d\omega. \quad (5.5)$$

Moreover, the total momentum transfer can be calculated by integrating the differential momentum transfer in the frequency domain

$$\mathbf{p} = \int_0^{\infty} \frac{d\mathbf{p}}{d\omega} d\omega, \quad (5.6)$$

for which we have [after exploiting Eqs. (5.4) and (5.5)]

$$\begin{aligned} \frac{d\mathbf{p}}{d\omega} &= \frac{1}{\pi} \text{Re} \left[\oint \varepsilon_0 \left[\mathbf{\mathcal{E}}(\mathbf{r}, \omega) \mathbf{\mathcal{E}}^*(\mathbf{r}, \omega) + c^2 \mathbf{\mathcal{B}}(\mathbf{r}, \omega) \mathbf{\mathcal{B}}^*(\mathbf{r}, \omega) \right. \right. \\ &\quad \left. \left. - \frac{1}{2} \overleftrightarrow{\mathbf{I}} \mathbf{\mathcal{E}}(\mathbf{r}, \omega) \cdot \mathbf{\mathcal{E}}^*(\mathbf{r}, \omega) - c^2 \frac{1}{2} \overleftrightarrow{\mathbf{I}} \mathbf{\mathcal{B}}(\mathbf{r}, \omega) \cdot \mathbf{\mathcal{B}}^*(\mathbf{r}, \omega) \right] \cdot \mathbf{n} dS \right]. \quad (5.7) \end{aligned}$$

If we want to utilize the last expression (5.7) for calculations of the momentum transfer to the spherical nanoparticle in the frequency domain, we have to integrate over the surface enclosing the sphere. Exploiting the symmetry of our problem, a spherical surface will be advantageously chosen.

5.1. MOMENTUM TRANSFER IN THE FREQUENCY DOMAIN

Notice that the electric and magnetic field contributions to the momentum transfer are separated in the surface integral in Eq. (5.7). Hence, the Maxwell stress tensor is naturally split into the electric and magnetic part, respectively. We will denote them in the following way:

$$\begin{aligned}\overleftrightarrow{\mathcal{T}}_{\mathcal{E}} &= \varepsilon_0 \left[\mathcal{E}(\mathbf{r}, \omega) \mathcal{E}^*(\mathbf{r}, \omega) - \frac{1}{2} \overleftrightarrow{\mathbf{I}} \mathcal{E}(\mathbf{r}, \omega) \cdot \mathcal{E}^*(\mathbf{r}, \omega) \right], \\ \overleftrightarrow{\mathcal{T}}_{\mathcal{B}} &= \varepsilon_0 c^2 \left[\mathcal{B}(\mathbf{r}, \omega) \mathcal{B}^*(\mathbf{r}, \omega) - \frac{1}{2} \overleftrightarrow{\mathbf{I}} \mathcal{B}(\mathbf{r}, \omega) \cdot \mathcal{B}^*(\mathbf{r}, \omega) \right].\end{aligned}\quad (5.8)$$

Also, we have to realize that the total field outside the particle has to be substituted in Eqs. (5.8), i.e. $(\mathcal{E}, \mathcal{B}) \rightarrow (\mathcal{E}^{\text{out}}, \mathcal{B}^{\text{out}})$. Since the expressions for the induced fields (4.3) and (4.4) are quite complicated as they contain many special functions, the surface integral will be calculated numerically. The evaluation of the total field is therefore performed only at particular points lying on the spherical surface enclosing our nanoparticle. The integrand multiplied by the surface element from Eq. (5.7) is in the terms of the electric and magnetic contribution, respectively, expressed as

$$\begin{aligned}\overleftrightarrow{\mathcal{T}}_{\mathcal{E}} \cdot \mathbf{n} \Delta S &= \\ \Delta S \frac{\varepsilon_0}{2} \begin{pmatrix} \mathcal{E}_x \mathcal{E}_x^* - \mathcal{E}_y \mathcal{E}_y^* - \mathcal{E}_z \mathcal{E}_z^* & 2\mathcal{E}_x \mathcal{E}_y^* & 2\mathcal{E}_x \mathcal{E}_z^* \\ 2\mathcal{E}_y \mathcal{E}_x^* & \mathcal{E}_y \mathcal{E}_y^* - \mathcal{E}_x \mathcal{E}_x^* - \mathcal{E}_z \mathcal{E}_z^* & 2\mathcal{E}_y \mathcal{E}_z^* \\ 2\mathcal{E}_z \mathcal{E}_x^* & 2\mathcal{E}_z \mathcal{E}_y^* & \mathcal{E}_z \mathcal{E}_z^* - \mathcal{E}_x \mathcal{E}_x^* - \mathcal{E}_y \mathcal{E}_y^* \end{pmatrix} &\cdot \mathbf{n},\end{aligned}\quad (5.9)$$

and

$$\begin{aligned}\overleftrightarrow{\mathcal{T}}_{\mathcal{B}} \cdot \mathbf{n} \Delta S &= \\ \Delta S \frac{\varepsilon_0 c^2}{2} \begin{pmatrix} \mathcal{B}_x \mathcal{B}_x^* - \mathcal{B}_y \mathcal{B}_y^* - \mathcal{B}_z \mathcal{B}_z^* & 2\mathcal{B}_x \mathcal{B}_y^* & 2\mathcal{B}_x \mathcal{B}_z^* \\ 2\mathcal{B}_y \mathcal{B}_x^* & \mathcal{B}_y \mathcal{B}_y^* - \mathcal{B}_x \mathcal{B}_x^* - \mathcal{B}_z \mathcal{B}_z^* & 2\mathcal{B}_y \mathcal{B}_z^* \\ 2\mathcal{B}_z \mathcal{B}_x^* & 2\mathcal{B}_z \mathcal{B}_y^* & \mathcal{B}_z \mathcal{B}_z^* - \mathcal{B}_x \mathcal{B}_x^* - \mathcal{B}_y \mathcal{B}_y^* \end{pmatrix} &\cdot \mathbf{n},\end{aligned}\quad (5.10)$$

where the surface element and the column vector of the surface normal in the case of our geometry read, respectively,

$$\Delta S = r^2 \sin(\theta) \Delta\theta \Delta\phi, \quad \mathbf{n} = \begin{pmatrix} \sin(\theta) \cos(\phi) \\ \sin(\theta) \sin(\phi) \\ \cos(\phi) \end{pmatrix}, \quad (5.11)$$

and where $\Delta\theta$ and $\Delta\phi$ are angular steps between the points of evaluation (r, θ, ϕ) . We should specify that in the previous expressions, we substituted the Cartesian vectors¹ dependent on spherical coordinates of the particular point, where the field is evaluated, i.e.

$$\begin{aligned}\mathcal{E}(\mathbf{r}, \omega) &= \{\mathcal{E}_x(r, \theta, \phi, \omega), \mathcal{E}_y(r, \theta, \phi, \omega), \mathcal{E}_z(r, \theta, \phi, \omega)\}, \\ \mathcal{B}(\mathbf{r}, \omega) &= \{\mathcal{B}_x(r, \theta, \phi, \omega), \mathcal{B}_y(r, \theta, \phi, \omega), \mathcal{B}_z(r, \theta, \phi, \omega)\}.\end{aligned}\quad (5.12)$$

¹The transformation of the vector field $\mathbf{V} = (V_r, V_\theta, V_\phi)$ from spherical to Cartesian basis reads $V_x = V_r \sin(\theta) \cos(\phi) + V_\theta \cos(\theta) \cos(\phi) - V_\phi \sin(\phi)$, $V_y = V_r \sin(\theta) \sin(\phi) + V_\theta \cos(\theta) \sin(\phi) + V_\phi \cos(\phi)$, $V_z = V_r \cos(\theta) - V_\theta \sin(\theta)$.

Now we have prepared everything to replace the surface integral with a desired discrete summation:

$$\iint_S \vec{\mathcal{T}} \cdot \mathbf{n} \, dS \approx \sum_N \vec{\mathcal{T}}_{\varepsilon} \cdot \mathbf{n} \Delta S + \sum_N \vec{\mathcal{T}}_{\mathbf{B}} \cdot \mathbf{n} \Delta S, \quad (5.13)$$

where we sum over N elements, in which the spherical surface is discretized. From the form of Eqs. (5.9) and (5.10) we directly see that for the momentum transfer we get three components as we have expected (it has to be a vectorial quantity). We are mostly interested in the transverse x component, which shows us whether the sphere is attracted or repelled in the perpendicular direction. From Fig. 5.2 visualizing orientation of the x axis, we see that positive values of the transferred transverse momentum are associated with the attraction, negative values refer to the repulsion.

We can also calculate the longitudinal z component, which is parallel with the trajectory of the electron. We do not consider a substrate in our model, but the longitudinal component would refer to a possible lifting of the particle with respect to the substrate plane. The momentum transfer in the y direction gives zero due to the symmetry of the problem (and thus the symmetry of the fields). In our particular case we obtain negligible values coming from the numerical treatment of the problem and associated errors.

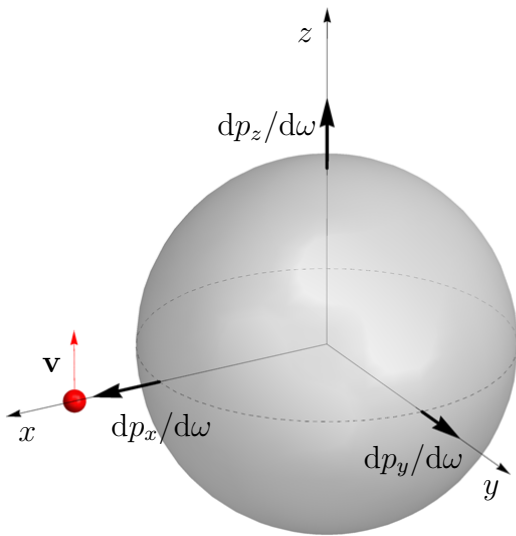


Figure 5.2: Orientation of the transferred momentum components. The x axis, associated with the transverse momentum transfer component, is oriented towards the electron. The longitudinal component is parallel with the z axis, which has the same direction as the electron velocity. The y component disappears due to the symmetry of the problem.

To evaluate the momentum transfer in the frequency domain, we use the analytical expressions for the external electromagnetic field produced by a bare electron (3.5) and (3.6), and the induced field is obtained from the multipole expansions (4.3), (4.4). The external field can be evaluated in the same manner, but of course utilization of the closed-form expressions is much faster than use of the expansions.

In our calculations we have considered a very small sphere with radius $a = 1$ nm and the impact parameter $b = 1.5$ nm, which corresponds to the performed experiments. Although a classical approach we are using enables a possibility to assume an electron passing infinitely close to the surface of the particle, we are aware of such a scenario as the quantum effects mentioned in section 2.2 will start to play an important role. Actually, they are probably already present even for larger impact parameters and influence the

5.1. MOMENTUM TRANSFER IN THE FREQUENCY DOMAIN

experimental results because of the small size of the sphere and the nature of the probe. This was partly mentioned in the discussion of non-locality in section 4.4, which was apparent even for the electrons passing further from the sphere.

Our assumption of the electron as a classical point-like and localized particle could also be seen as an oversimplification, but we believe that even with this classical treatment, we can still get a good insight into the problem which is the main purpose of our work.

5.1.1. Aluminium nanosphere

As we have shown in Chapter 2, the response of aluminium is quite well expressed by the Lorentz-Drude dielectric function (2.5), where we substitute the parameters from table 2.1.

Convergence of numerical evaluation of the momentum transfer was tested for a different number of the discretization points as well as for increasing number of multipoles l_{\max} . We have found out that considering $l_{\max} = 20$ and a following mesh containing 1836 points:

$$\begin{aligned}\theta_{\min} &= 2.5^\circ & \theta_{\max} &= 177.5^\circ & \Delta\theta &= 3.5^\circ \\ \phi_{\min} &= 0^\circ & \phi_{\max} &= 170^\circ & \Delta\phi &= 10^\circ\end{aligned}$$

is sufficient to obtain results with a good accuracy (see Fig. 4.1 for the definition of the spherical coordinates we use).

We have considered an energy range 0.01 – 2048 eV with a step 62.5 meV which gives us a grid containing 32 768 points in the frequency space. Despite the fact that the most pronounced spectral features will appear at quite low energies (units of eV), we need to use such a wide range especially for a subsequent transformation to the time domain.

The results we have obtained for two non-vanishing components of the differential momentum transfer and three different energies of the impinging electron are plotted in Fig. 5.3. In 5.3 a) we show the transverse component possessing an oscillatory-like behaviour in the region where the localized surface plasmon modes are excited (compare with Fig. 4.5). The most pronounced peak corresponds to the excitation of the dipolar mode. We can notice that the higher-order modes contribute more negatively and according to Refs. [12, 16] can cause a negative sign of the total momentum transfer.

It seems that for higher frequencies the contribution to the transferred transverse momentum is only negative, slowly approaching zero. However, the inset of Fig. 5.3 a) shows a zoomed spectrum covering all the spectral range we have investigated. At very high frequencies we observe a sign reversal and a wide positive peak for each of three energies of the electron. If we realize that such wide-spectral features have to correspond to short-time events in the time domain, we can conclude that it has to be associated with the closest approach of the electron to the nanosphere and strongly connected with the ultra-fast action of the external fields brought by the electron. Width of the peak is also increasing for higher electron energies, as well as its position, which supports our hypothesis, because the flyby of the electrons with higher velocities is shorter.

The longitudinal component of the differential momentum transfer plotted in 5.3 b) is only positive. Importantly, the spectral dependence is very similar to the loss spectrum in Fig. 4.5 which is not so big surprise when we realize that the energy loss corresponds

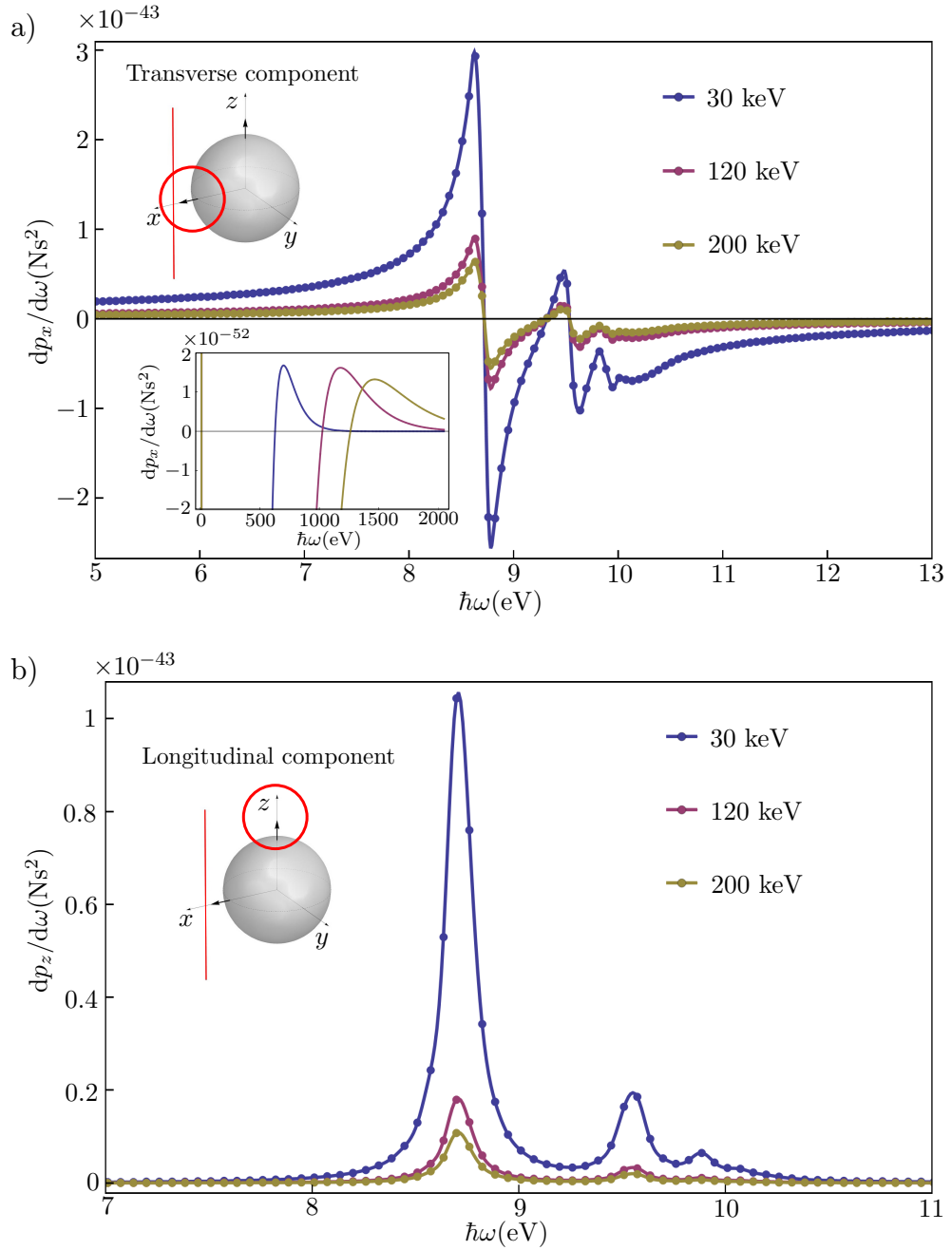


Figure 5.3: The momentum transfer to an aluminium sphere with radius $a = 1$ nm from an electron passing at the impact parameter $b = 1.5$ nm with three different energies: 30, 120 and 200 keV. The x component is plotted in part a), while the longitudinal z component is shown in b). The inset visualizes the crossing of the x component from negative to positive values at high energies. The momentum transfer was calculated at discrete energy values plotted as dots, the continuous lines are splines, that should guide our eyes.

to the stopping of the electron along its trajectory and therefore is directly related to the momentum transfer in this direction. On the contrary, the transverse momentum transfer causes only negligible energy loss of the electron and deflection of its trajectory [88].

5.1. MOMENTUM TRANSFER IN THE FREQUENCY DOMAIN

Notice that the differential momentum transfer is decreasing for higher electron velocities for both components. This is again caused by the lower interaction volume as we have discussed in section 4.4 related to the loss probability. For higher energies, the external field also couples more effectively with the higher-order modes.

When we integrate the differential momentum transfer over all the frequency range, according to Eq. (5.6) we obtain the total momentum transfer. In our case we have to change the integration to a discrete summation over the frequency grid where we calculated the differential contributions. Results for both the transverse and longitudinal components and three electron energies are summarized in table 5.1. For all the initial energies we observe here only positive values which is in the case of the transverse component in disagreement with results presented in Ref. [16].

Table 5.1: The mechanical momentum transfer to an aluminium nanosphere with radius $a = 1$ nm and the electron passing at $b = 1.5$ nm with three different initial energies. We split here the electric and the magnetic contributions.

	30 keV	120 keV	200 keV
$\Delta p_{x,\mathcal{E}} (\times 10^{-30} \text{ Ns})$	36.3	53.6	70.4
$\Delta p_{x,\mathcal{B}} (\times 10^{-30} \text{ Ns})$	-23.4	-51.2	-68.8
$\Delta p_x = \Delta p_{x,\mathcal{E}} + \Delta p_{x,\mathcal{B}} (\times 10^{-30} \text{ Ns})$	12.9	2.4	1.6
$\Delta p_{z,\mathcal{E}} (\times 10^{-30} \text{ Ns})$	44.9	6.5	3.4
$\Delta p_{z,\mathcal{B}} (\times 10^{-30} \text{ Ns})$	2.9	1.7	1.5
$\Delta p_z = \Delta p_{z,\mathcal{E}} + \Delta p_{z,\mathcal{B}} (\times 10^{-30} \text{ Ns})$	47.8	8.2	4.9

Moreover, if we separate the electric and magnetic part in the Maxwell stress tensor as shown in Eqs. (5.9) and (5.10), we can evaluate the electric and magnetic contribution to the total momentum transfer separately. These two contributions are also listed in table 5.1 and interestingly, in the case of the transverse component they go against each other. Hence, if the magnetic part prevails, we could obtain the negative value of the total momentum transfer – the repulsion with respect to the electron beam.

As we mentioned, the total momentum transfer is obtained from the summation of the differential contributions over the finite frequency range. For this purpose we tested convergence of the total transverse momentum transfer with respect to the maximal frequency taken into account. Such a dependence is plotted in Fig. 5.4 a) where we illustrate that the value becomes safely converged above the energy $\hbar\omega \approx 500$ eV. We have also found out that for the lower energy of the electron, convergence is achieved slightly faster.

In Fig. 5.4 b) we selected the dependence related to the 120 keV electron and observe the mentioned competition between the positive electric and negative magnetic contribution to the transverse component, whereas the electric one prevails (the sum of both contributions is plotted by the solid red line). Here we can conclude that despite the fact that the main spectral peaks associated with the localized surface plasmons appear only in a narrow energy range of units of eV, we have to sum up to quite high energies. However, if we recall the high-energy spectral features, it is not so surprising – we have to

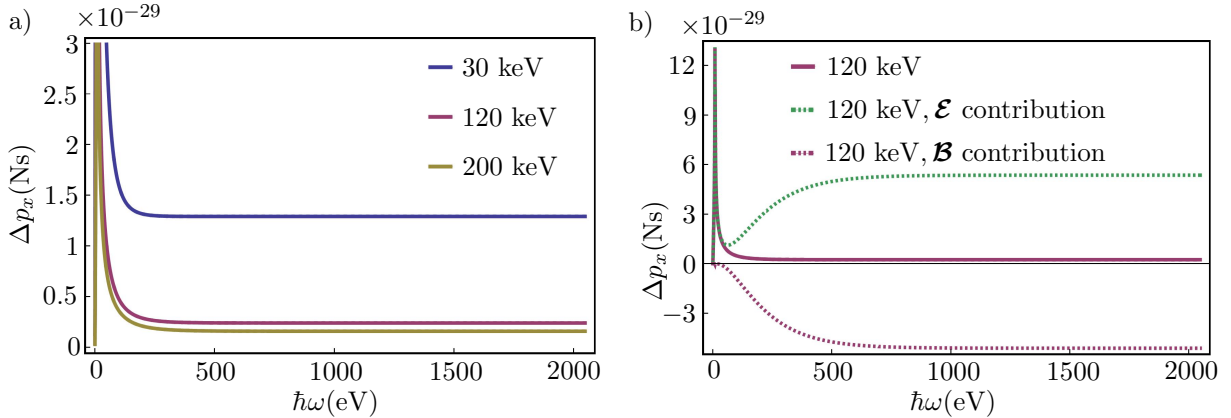


Figure 5.4: a) Test of convergence of the total transverse momentum transfer to the aluminium sphere with respect to the maximal frequency taken into account for three different energies of the impinging electron. b) Convergence of the total transverse momentum transfer corresponding to the 120 keV electron (solid red line) where the electric and magnetic contribution are plotted separately by green and red dashed lines.

realize that the attributed short-time events appear at a very broad spectral range. Other thing is, that the sign reversal apparently does not significantly influence convergence.

5.1.2. Gold nanosphere

Similar calculations as in the case of the aluminium nanosphere were also performed for a gold nanosphere with the same size and the impact parameter ($a = 1 \text{ nm}$, $b = 1.5 \text{ nm}$). The dielectric response of gold was modeled by the Kramers-Kronig consistent fit given by the Drude-Lorentz term supplemented by the additional Lorentz oscillators as shown in Eq. (2.9) with parameters taken from tables 2.1 and 2.2.

In Fig. 5.5 we plot the differential momentum transfer to the gold nanosphere for three different energies of the impinging electron. Analogously to the EELS spectra, we can observe completely different spectral behaviour than in the case of aluminium, which is caused by the more complex dielectric response of gold used in our calculations.

The transverse component visualized in Fig. 5.5 a) possesses a pronounced peak around 2.5 eV which, as we have already discussed in Section 4.4, corresponds to the localized surface plasmons excitation. Then we observe several smaller features and importantly, around 23 eV we get a sign reversal. The positive high-energy peaks, which were discovered in previous subsection, are again revealed, see the zoomed spectrum in the inset of Fig. 5.5 a). Notice that compared to aluminium, these features appear at even higher energies which implies that the gold nanosphere will respond earlier as the oscillators at higher frequencies contribute more significantly than in the case of a Drude-type material.

The longitudinal component plotted in part 5.5 b) is again only positive. Furthermore, it spectrally perfectly corresponds to the loss probability multiplied by ω [see the loss probability definition in Eq. (3.8)]. We also observe qualitatively same behaviour for changing electron energy as in the previous case: with increasing energy we obtain the smaller differential momentum transfer as we expect.

The electric and magnetic contributions to the transferred mechanical momentum are summarized in table 5.2. We still get only positive values for the transverse component,

5.1. MOMENTUM TRANSFER IN THE FREQUENCY DOMAIN

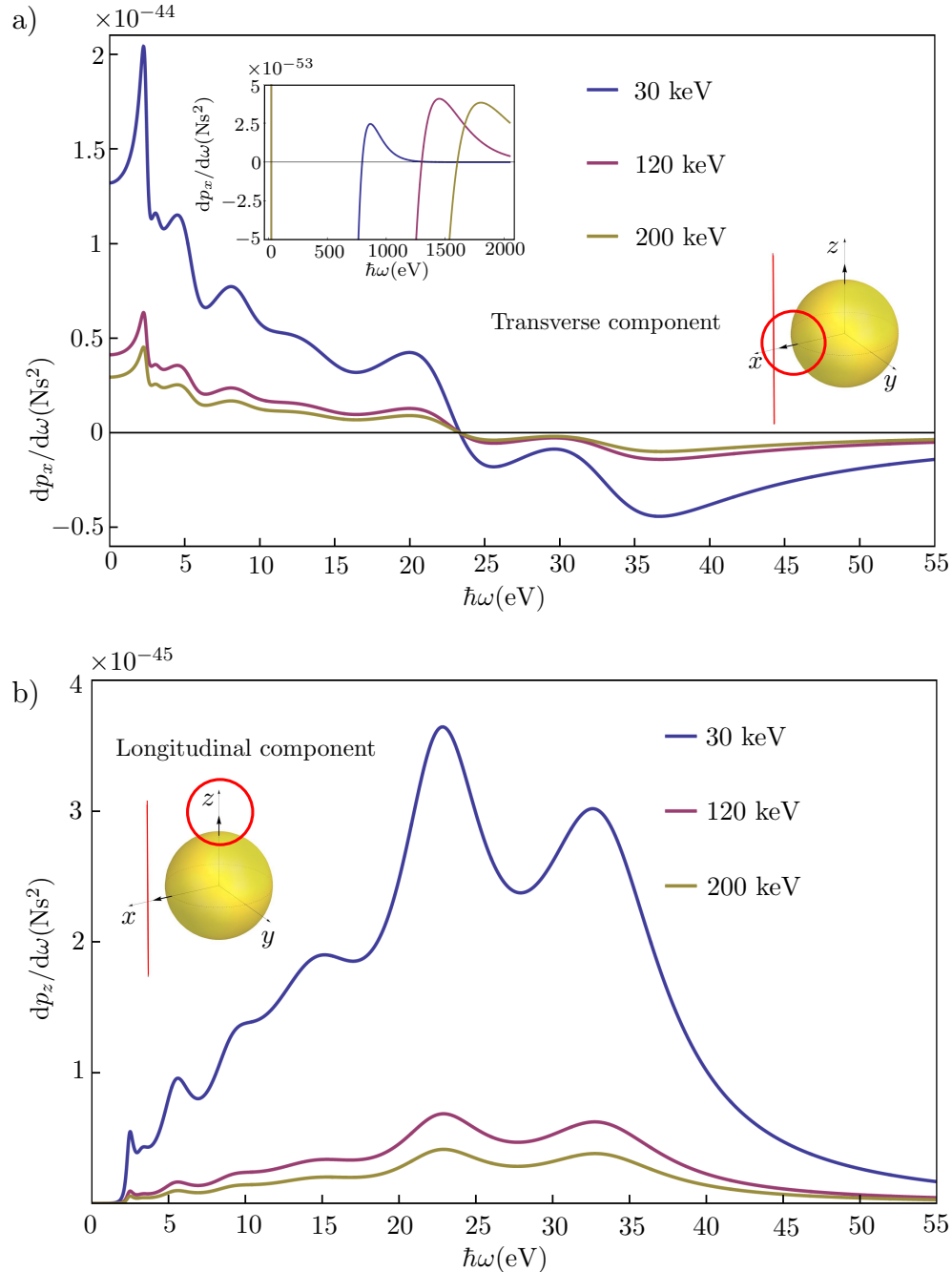


Figure 5.5: The differential momentum transfer to the gold sphere with radius $a = 1$ nm from an electron passing at the impact parameter $b = 1.5$ nm with three different energies: 30, 120 and 200 keV. The x component is plotted in part a), while the longitudinal z component is shown in b). The inset visualizes the crossing of the x component from negative to positive values at high energies.

which agrees with results from Ref. [16], where a positive value was also obtained for the same impact parameter and 100 keV electrons. However, the plots of the differential momentum transfer published in Ref. [16] with the discrepancies around 28 eV coming from a mismatch of different sets of experimental data reveal that Kramers-Kroning con-

sistent fit was not used and the dielectric function was probably only splined. We would like to point out that such an approach can lead to unphysical results [95]. The momentum transfer will depend on the dielectric response very strongly – the realistic (but still physical) models are therefore highly desirable. We are aware that our approach still contains a significant level of approximation and that further theoretical investigation considering model refinements is necessary. The best feasible approach could e.g. rely on the nanosphere response derived from the first-principles calculations [96].

Table 5.2: The mechanical momentum with split of the electric and magnetic contributions transferred to the gold nanosphere with the radius $a = 1$ nm and an electron passing at $b = 1.5$ nm with three different energies.

	30 keV	120 keV	200 keV
$\Delta p_{x,\mathcal{E}}$ ($\times 10^{-30}$ Ns)	91.3	60.0	73.4
$\Delta p_{x,\mathcal{B}}$ ($\times 10^{-30}$ Ns)	-22.6	-49.8	-67.5
$\Delta p_x = \Delta p_{x,\mathcal{E}} + \Delta p_{x,\mathcal{B}}$ ($\times 10^{-30}$ Ns)	68.7	10.2	5.9
$\Delta p_{z,\mathcal{E}}$ ($\times 10^{-30}$ Ns)	122.3	20.8	11.3
$\Delta p_{x,\mathcal{B}}$ ($\times 10^{-30}$ Ns)	7.1	5.2	4.6
$\Delta p_z = \Delta p_{z,\mathcal{E}} + \Delta p_{z,\mathcal{B}}$ ($\times 10^{-30}$ Ns)	129.4	26.0	15.9

5.2. Calculation of the force in the time domain

Once we start to calculate the instantaneous mechanical momentum transfer in the time domain it is not possible to simply remove the field momentum as we did in the frequency domain. There are basically two possibilities how the time-dependent Lorentz force (or the mechanical momentum time derivative) can be calculated. The first one is to continue using the Maxwell stress tensor formalism, but with the subtraction of the field momentum rate of change:

$$\mathbf{F}_{\text{mech}} = \frac{d\mathbf{p}_{\text{mech}}}{dt} = \iint_S \overleftrightarrow{\mathbf{T}} \cdot \mathbf{n} dS - \frac{1}{c^2} \frac{d}{dt} \iiint_V (\mathbf{E}^{\text{in}} \times \mathbf{H}^{\text{in}}) dV, \quad (5.14)$$

or the second option is to use the differential Lorentz force formulation as discussed in Section 1.2 with direct substitution from Maxwell's equations

$$\begin{aligned} \mathbf{F}_{\text{mech}} &= \iiint_V (\rho \mathbf{E}^{\text{in}} + \mathbf{J} \times \mathbf{B}^{\text{in}}) dV \\ &= \iiint_V \varepsilon_0 \left[\mathbf{E}^{\text{in}} (\nabla \cdot \mathbf{E}^{\text{in}}) + \mathbf{B}^{\text{in}} \times \frac{\partial \mathbf{E}^{\text{in}}}{\partial t} - c^2 \mathbf{B}^{\text{in}} \times (\nabla \times \mathbf{B}^{\text{in}}) \right] dV. \end{aligned} \quad (5.15)$$

The previous equation can be in some cases further simplified to avoid evaluation of the divergence and curl, see e.g. Ref. [30].

5.2. CALCULATION OF THE FORCE IN THE TIME DOMAIN

Both presented approaches include volume integration, therefore they should be similarly computationally demanding. However, all the results presented within this section were calculated from the first approach utilizing Eq. (5.14).

Notice that to calculate the time dependent mechanical force, we have to know the electromagnetic field both inside and outside the sphere in the time domain. It can be obtained using the following strategy: the analytical expressions in the frequency domain (4.3), (4.4), (4.8), and (4.9) are evaluated in particular space points for a chosen frequency grid and then with use of the inverse discrete Fourier transform algorithm transformed in the time domain. The frequency grid has to be determined carefully since its width (or the highest frequency taken into account) is related to a step in the time grid. Reversely, the frequency step corresponds to the width of the time grid.

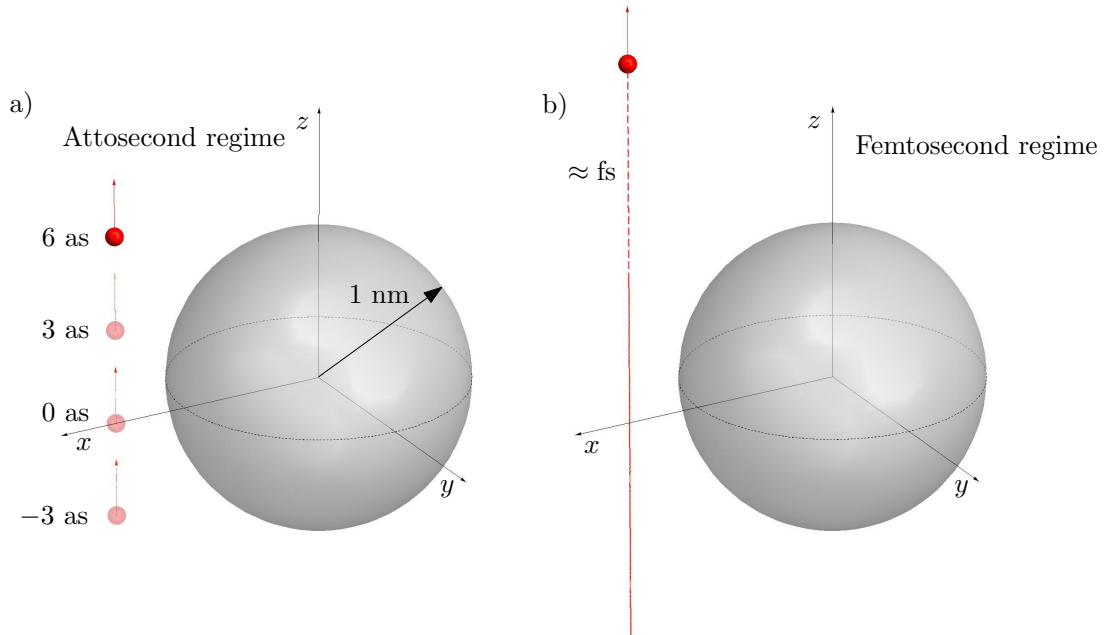


Figure 5.6: A scheme of two different regimes observed in the time domain. At attoseconds the 120 keV electron represented by the small red sphere is very close to the metallic sphere, in part a) it is depicted for a few attosecond times in the rest frame of the nanosphere. Notice that at negative times, the electron is in the lower half-space and conversely. In part b) representing the femtosecond regime, the electron is already far from the nanoparticle.

In this work we have utilized the discrete Fourier transform implemented in Mathematica software [57, 97]. In order to capture both an ultra-fast phenomena when the closest approach of the electron to the nanosphere is observed (units of attoseconds) and the localized surface plasmon decay, which happens at a time range in order of femtoseconds², the already mentioned frequency grid was chosen:

$$\hbar\omega_{\min} = 10 \text{ meV} \quad \hbar\omega_{\max} = 2048 \text{ eV} \quad \Delta\hbar\omega = 62.5 \text{ meV},$$

whereas the corresponding time grid then reads

²1 as = 10^{-18} s; 1 fs = 10^{-15} s

$$t_{\min} = -\frac{\pi}{\Delta\omega} = -33.1 \text{ fs} \quad t_{\max} = \frac{\pi}{\Delta\omega} = 33.1 \text{ fs} \quad \Delta t = \frac{\pi}{\omega_{\max} - \omega_{\min}} = 1 \text{ as.}$$

It should be mentioned that for the inverse transform we have again utilized properties of the Fourier transform of real function and the Rayleigh-Parseval theorem presented in Appendix A. Number of the points in the time grid is thus doubled compared to the frequency grid.

We should add that the spatial discretization regarding the spherical angles is preserved from the frequency domain calculations. However, in this case we also have to discretize the volume inside the sphere. For this purpose, we used ten equidistantly spaced concentric spherical shells: $r_{\min} = 0.05 a$, $r_{\max} = 0.95 a$, $\Delta r = 0.1 a$.

We will continue in the split of results corresponding to the aluminium and gold nanosphere. Two different regimes, depicted in Fig. 5.6 will also be distinguished as we have already suggested. The ultra-fast forces arise during the closest electron flyby at attoseconds and slowly decaying plasmon-induced oscillatory fields and forces persist at femtoseconds after the electron passage.

5.2.1. Aluminium nanosphere

First we are going to introduce all the parts of the calculation step by step. For this purpose we will again take the parameters $a = 1 \text{ nm}$, $b = 1.5 \text{ nm}$ and the energy of the impinging electron 120 keV . Before we proceed directly to the evaluation of the momentum rate of change, we show the transformed electromagnetic field as it will be important for further discussion and understanding.

The total electric and magnetic field magnitude just above the nanoparticle boundary ($r = 1.0001 \text{ nm}$) at three specific attosecond times is visualized in Fig. 5.7. Notice that the field is very intense, strongly localized, and the produced pattern clearly follows the moving electron, whose position in the rest frame of the nanoparticle is schematically represented by the small red sphere with the arrow denoting the direction of its motion. Recall that outside the particle the total field is a sum of the induced and the external field – it seems that at such short times the latter is prevailing. The patterns are of an elliptic shape, which is caused by the Lorentz contraction in the z direction along which the electron is moving.

To see if there is any response of the nanoparticle, the induced field magnitude is plotted separately in Fig. 5.8. Despite the fact that such an ultra-fast phenomena corresponds to very high frequencies, where the material response is extremely weak and it is becoming almost transparent for the external electromagnetic field ($\text{Re}\{\varepsilon_r\} \approx 1$, $\text{Im}\{\varepsilon_r\} \approx 0$), there is still some induced field produced as the reaction of the nanoparticle to the very strong external perturbation.

We can observe much weaker field than the external one (compare the magnitude with the total field in Fig. 5.7) related to a slowly forming induced charge density corresponding to the electric field magnitude; the highest magnitude of the magnetic field corresponds to the places with the highest current density. A small fraction of electrons within the nanoparticle is repelled and positive holes are thus with some delay following the position of the swift electron. As the electron is passing by the sphere, the response is increasing and at later times we expect a formation of the decaying oscillating field of the similar magnitude assigned to the localized surface plasmons.

5.2. CALCULATION OF THE FORCE IN THE TIME DOMAIN

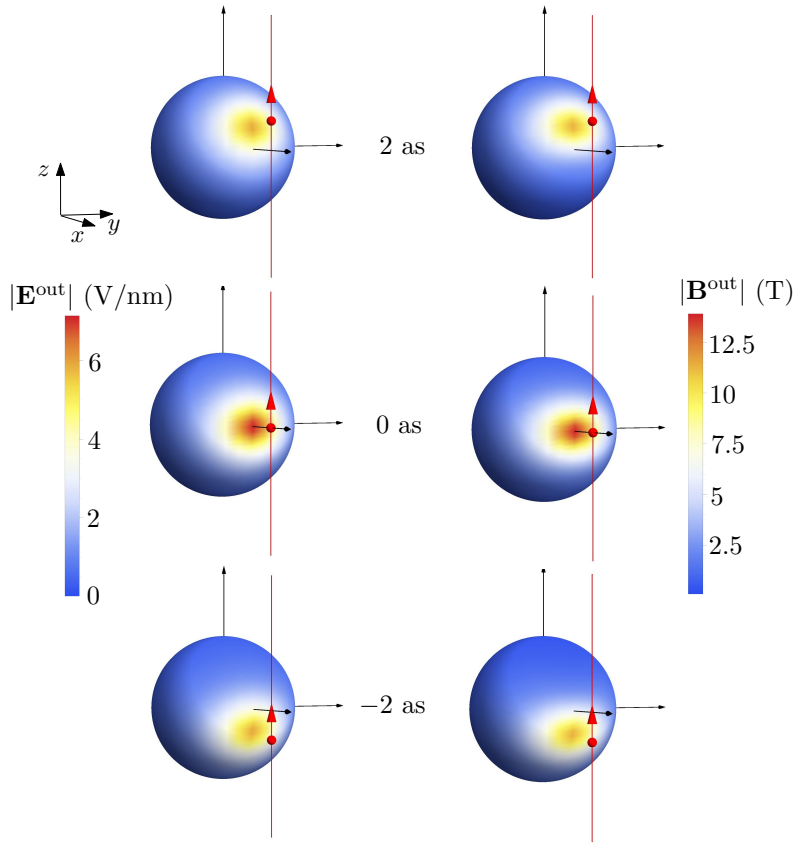


Figure 5.7: Magnitude of the total electric field (left column) and the total magnetic field (right column) outside the aluminium nanoparticle plotted on the spherical surface very close to the nanosphere boundaries ($r = 1.0001$ nm) at three attosecond times denoted between the spheres. The position of the electron in the nanoparticle rest frame is visualized by the small red sphere with the arrow. In the calculations, the parameters $a = 1$ nm, $b = 1.5$ nm were used, the energy of the impinging electron was chosen to be 120 keV.

The total field magnitude at four close femtosecond times is plotted in Fig. 5.9. On the contrary to the total electromagnetic field at attoseconds, we observe a few orders of magnitude lower values. The swift electron carrying the very strong external field is now far away from the sphere and the induced part becomes dominant. In general, different modes take part in the field pattern periodic change, which is completely different behaviour than we observed at attoseconds. Recall that the plasma frequency of aluminium is $\omega_p = 15.1$ eV, the plasmonic oscillatory field is thus formed within tenths of femtoseconds after the electron passage.

Once we have transformed the electromagnetic field in the time domain, it can be used in further calculations. We first calculate the time-dependent total momentum time derivative which is nothing but the Maxwell stress tensor integrated over the spherical surface enclosing the metallic particle. We particularly discuss the transverse component of the total momentum time derivative with split of the electric and magnetic field contribution, which is plotted in Fig. 5.10 (recall that $d\mathbf{p}_{\text{tot}}/dt = d\mathbf{p}_{\mathbf{E}}/dt + d\mathbf{p}_{\mathbf{B}}/dt$).

Fig. 5.10 a) shows that the mostly positive electric part goes against the magnetic one at attoseconds, taking quite large values in order of pN. The curves are asymmetric,

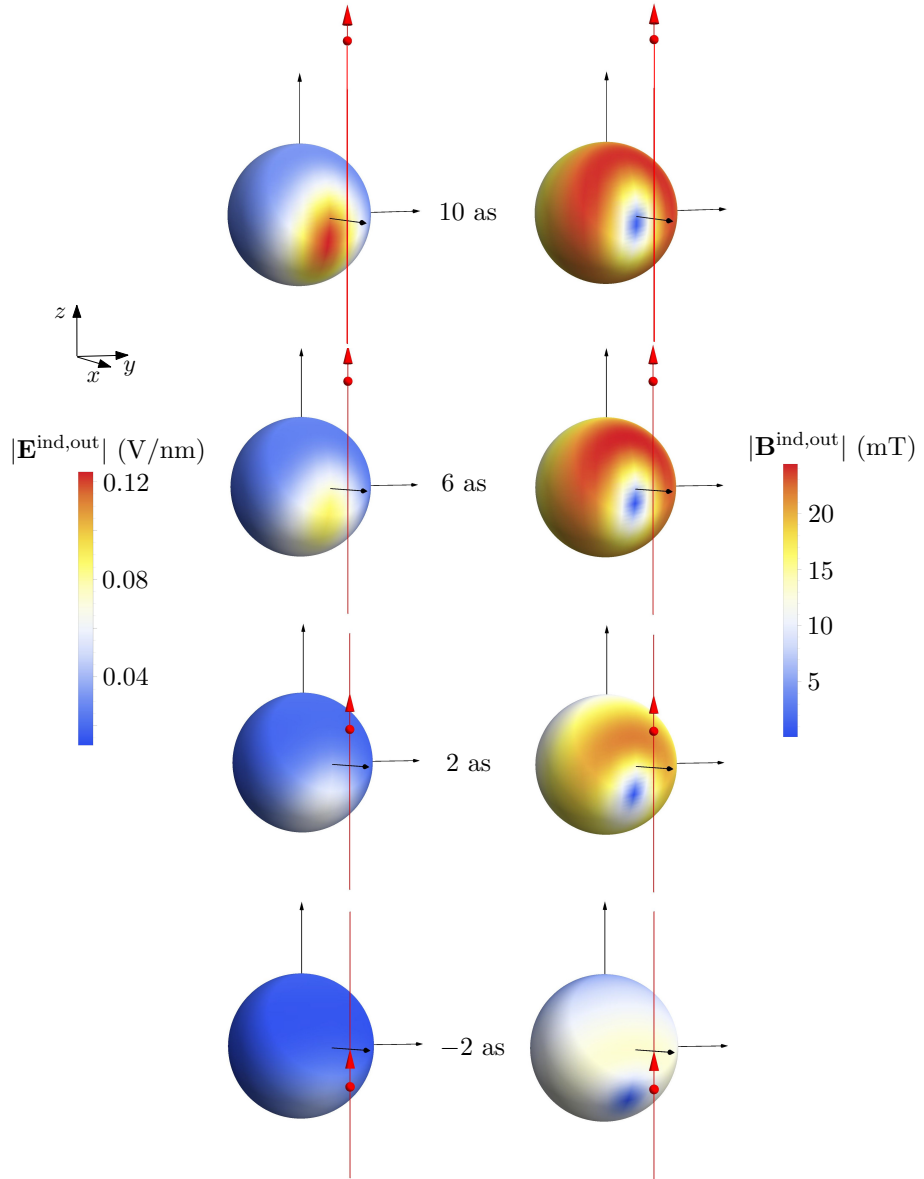


Figure 5.8: Magnitude of the induced electric field in the left column and the magnetic field in the right column, respectively, calculated for the parameters $a = 1 \text{ nm}$, $b = 1.5 \text{ nm}$ and the 120 keV electron just above the aluminium nanosphere surface ($r = 1.0001 \text{ nm}$) at four different attosecond times. The electron in the rest frame of the nanoparticle is schematically depicted by the small red sphere with the arrow denoting the direction of its motion.

which is apparent especially in the electric part and in the sum of the electric and magnetic contribution. The electric part starts to be slightly negative at $t \approx 13 \text{ as}$, which is related to material response. However, as we have shown, the external fields brought by the moving electron are dominant at this time range.

At femtoseconds, the mentioned oscillatory behaviour is observed, whereas visible beats are caused due to the appearance of different plasmonic modes (particularly dipolar, quadrupolar and hexapolar). Now, the calculated values are only in order of tenths of fN

5.2. CALCULATION OF THE FORCE IN THE TIME DOMAIN

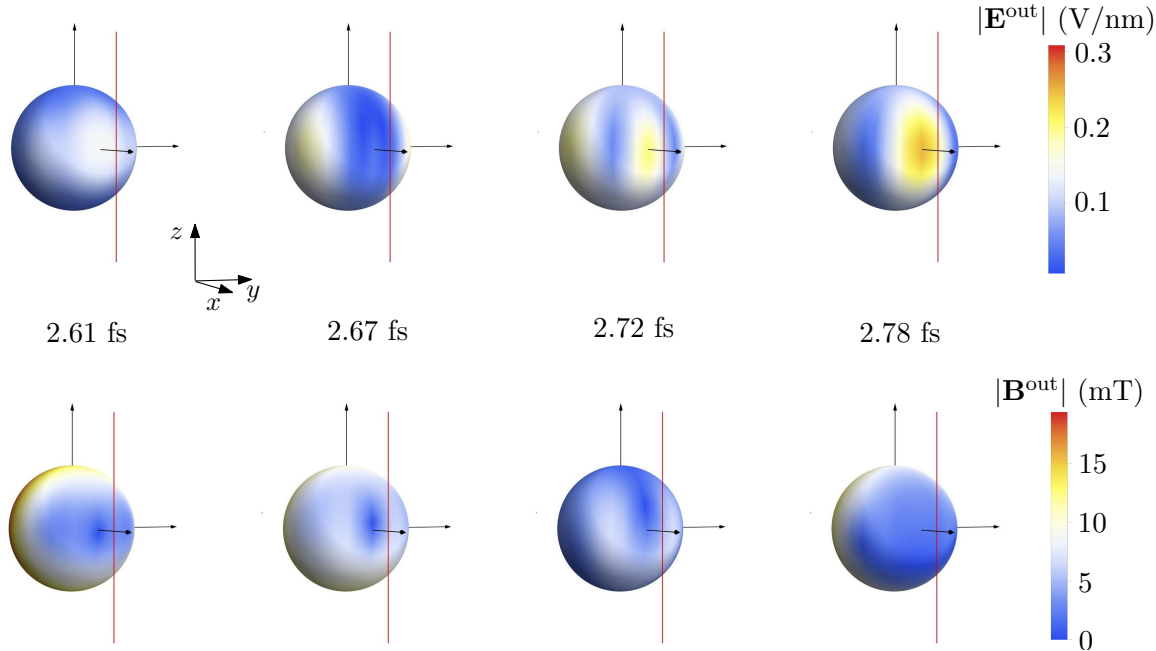


Figure 5.9: Magnitude of the total electromagnetic field evaluated at $r = 1.0001$ nm just above the aluminium nanoparticle boundary plotted on the spherical surface at four femtosecond times denoted between the spheres. The electric field magnitude is plotted in the upper row, whereas the magnitude of the magnetic field in the lower row. The trajectory of the electron, which is now far away, is represented by red lines. We used the parameters $a = 1$ nm, $b = 1.5$ nm and the energy of the impinging electron 120 keV.

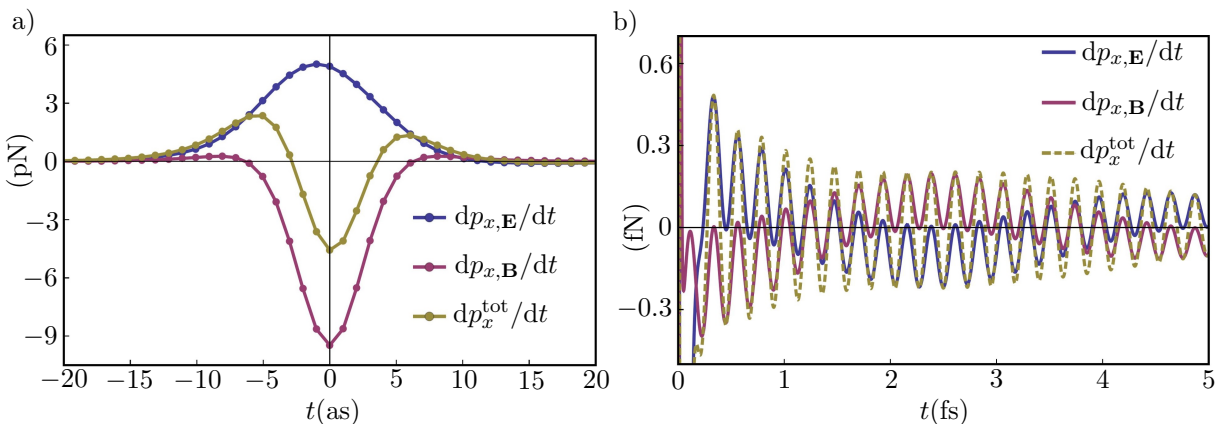


Figure 5.10: The transverse component of the Maxwell stress tensor (yellow) with split of the electric (blue) and magnetic (red) contributions integrated over the spherical surface for the integration sphere radius $r = 1.0001$ nm during attoseconds a) and femtoseconds b) after the electron flyby. The calculation was performed for the aluminium sphere, the 120 keV electron and the parameters $a = 1$ nm, $b = 1.5$ nm. Notice that the values are calculated for the discrete times corresponding to the used time grid, the lines connecting the discrete points during attoseconds serve to guide our eyes. These points are undistinguishable at femtoseconds.

which, as we know, is caused by the fact that compared to the strong external field, only weak field connected to the localized surface plasmons is prevailing.

We were also interested in differences between the total momentum obtained from the integration over the aluminium sphere and the sphere filled with vacuum, which tells us how much the induced fields contribute to the total momentum rate of change. These calculations with split of the electric and magnetic parts are plotted in Fig. 5.11. The magnetic part underwent only negligible changes and remains almost the same (the curves related to the spheres filled with aluminium and vacuum are almost undistinguishable). Hence, we can conclude that the magnetic contribution is given mainly by the external fields. On the contrary, the electric part is obviously more influenced by the induced fields coming from the dielectric response of aluminium since the changes and produced asymmetry are clearly visible. The slight changes in the magnetic part of the integrated Maxwell stress tensor are mostly given by the currents corresponding to the charge rearrangement.

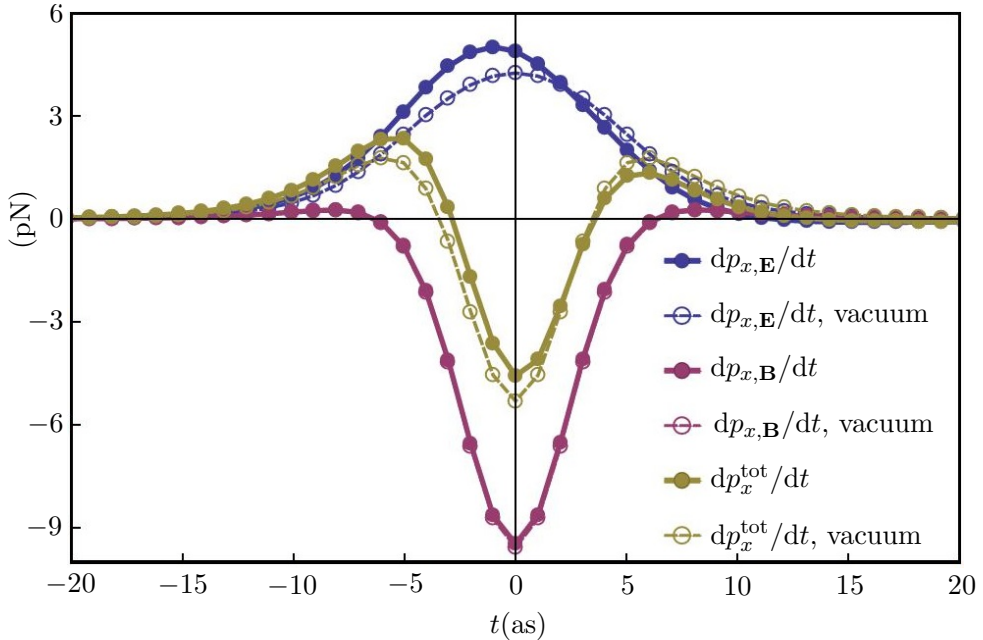


Figure 5.11: Comparison of the Maxwell stress tensor integrated at the radial coordinate $r = 1.0001$ nm over the 1-nm aluminium sphere (solid lines with filled circles) and empty space (dashed lines with empty circles, denoted by "vacuum") with split of the electric and magnetic contributions. The 120 keV electron was passing at the impact parameter $b = 1.5$ nm.

So far, we were plotting and commenting the rate of change of the total momentum. To show that it really does not correspond to the mechanical force, in Fig. 5.12 we plot the transverse component of dp_x^{tot}/dt for different radii of the integration spherical surface. In the attosecond regime illustrated in Fig. 5.12 a) we see that with the increasing radius we get higher values because in larger volume more of the field momentum, mostly given by the external field, is hidden. We are also approaching closer to the electron trajectory where the field is stronger. On the contrary, Fig. 5.12 b) shows that at femtoseconds we obtain higher values when we integrate closer to the nanoparticle surface. This is related to strong near fields around the metallic sphere which decay spatially quite quickly.

5.2. CALCULATION OF THE FORCE IN THE TIME DOMAIN

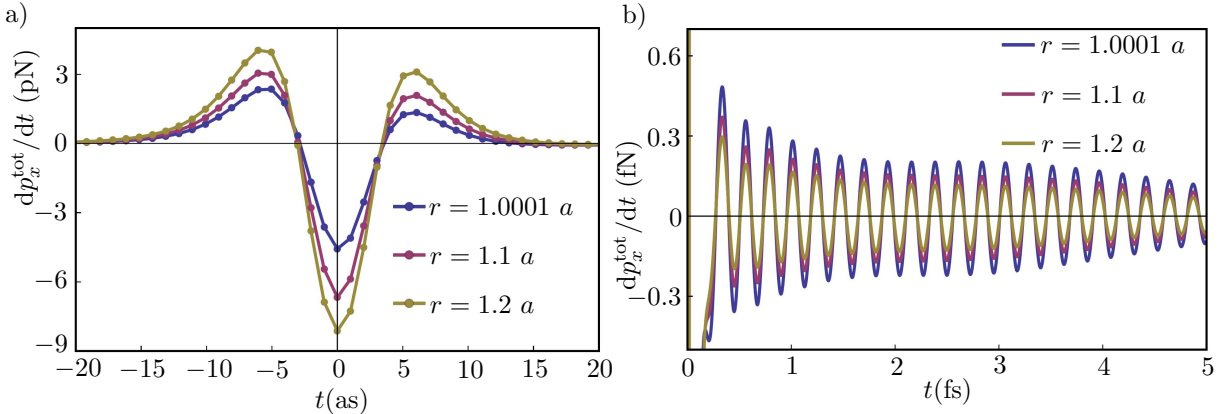


Figure 5.12: The transverse component of the total momentum transfer time derivative, i.e. the Maxwell stress tensor integrated over the spherical surface for three different radii of the integration sphere at attoseconds a) and at femtoseconds b). The aluminium nanoparticle with radius $a = 1$ nm and the 120 keV electron passing at the impact parameter $b = 1.5$ nm were considered in the calculation.

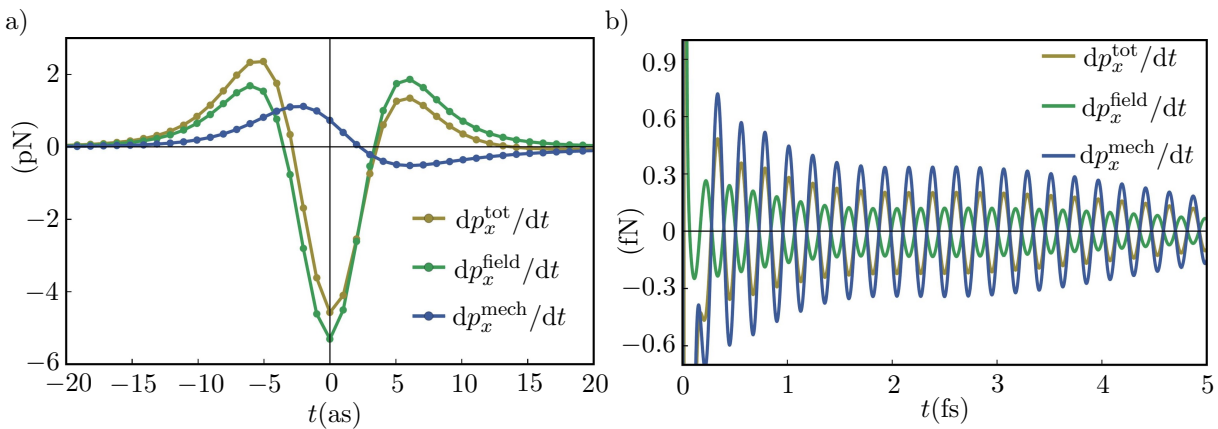


Figure 5.13: The time dependent transverse component of the mechanical force (blue lines), which was obtained by the subtraction of the field momentum time derivative (green) from the total momentum time derivative (yellow) at attoseconds a) and femtoseconds b). Here we considered the aluminium nanoparticle with radius $a = 1$ nm and the 120 keV electron passing at the impact parameter $b = 1.5$ nm.

As we know, to obtain the mechanical force, the field momentum time derivative has to be subtracted from the total momentum derivative as expressed in Eq. (5.14). To calculate the rate of change of the field momentum, we first use the same approach as for the field outside and transform the field inside the sphere in the time domain. Then we evaluate the field momentum density and integrate it over the spherical volume [see Eq. (1.26)]. After that the time dependence of the integrated field momentum is splined and the time derivative is numerically performed at certain time points corresponding to the chosen time grid. The transverse components of the total momentum, field momentum and finally the mechanical momentum time derivatives are shown together in Fig. 5.13 again for attosecond times in subfigure a) and at femtoseconds in b).

During attoseconds, the transverse components of the total and field momentum time derivatives are qualitatively similar, but shifted with respect to each other and exhibit slightly different symmetry. After the subtraction, we get completely different behaviour of the mechanical force: when the electron is approaching the nanosphere it is first being attracted to the electron in the transverse direction and then after approximately two attoseconds it starts to be repelled. The force is in order of piconewtons, which is four orders of magnitude larger than later in the femtosecond regime. At femtoseconds, the field momentum derivative phase is reversed with respect to the total momentum derivative and after the subtraction the resulting force in the x direction is thus larger than the total momentum rate of change.

In the case of the aluminium nanosphere with the chosen parameters, the calculation process was performed for three different energies of the impinging electron, similarly as in the frequency domain in Subsection 5.1.1. Results for the transverse component of the instantaneous mechanical force acting on the sphere are plotted in Fig. 5.14, where we see that the attosecond and femtosecond forces posses the same behaviour for the changing electron energy.

During the approach of the electron at attosecond times [see part 5.14 a)], the attraction is observed. After the electron crosses the plane $z = 0$, the negative contributions become more dominant and later repulsion is obtained. Quantitatively, we observe the same dependence as in the frequency domain: the exerted forces are larger for lower electron velocities. This is again related to larger interaction volume and longer time electron spends in a close vicinity of the nanoparticle. Hence, the nanoparticle material has got more time for the response.

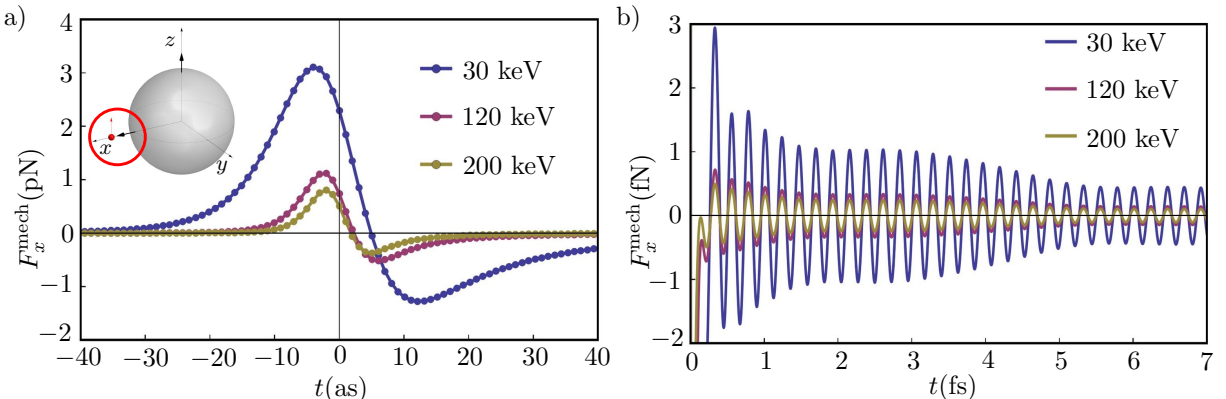


Figure 5.14: The time dependent transverse component of the mechanical force acting on the 1-nm aluminium nanosphere at attoseconds a) and femtoseconds b) for three different energies of the impinging electron. The impact parameter was considered to be $b = 1.5$ nm in all the cases.

The femtosecond forces depicted in Fig. 5.14 b) are oscillating with the same phase and a period $T = 0.23$ fs for all the electron energies, which corresponds to a half of the dipolar plasmonic mode period. Notice that the femtosecond forces are three orders of magnitude smaller than the forces during attoseconds. In real systems where a substrate is present, adhesion forces have to be overcome to manipulate with the nanoparticle. It is rather difficult to estimate a threshold, when the nanoparticle starts to move, as it strongly depends on the atomic structure of the contact surfaces, but we believe that

5.2. CALCULATION OF THE FORCE IN THE TIME DOMAIN

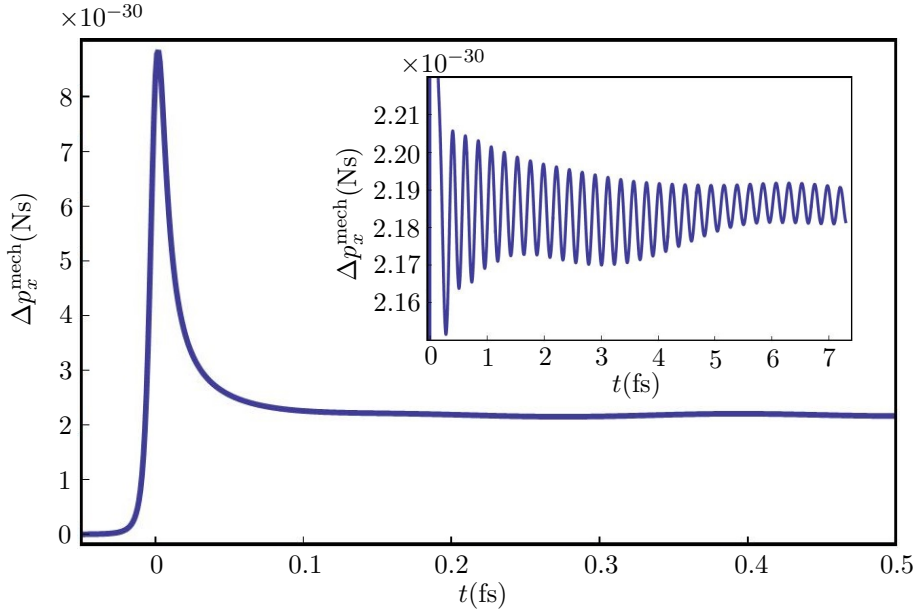


Figure 5.15: The transverse component of the cumulatively summed differential (numerically integrated) mechanical momentum transfer to the aluminium nanosphere with radius $a = 1$ nm from the 120-keV electron passing at the impact parameter $b = 1.5$ nm.

the force in order of piconewtons should be sufficient. On the contrary, the oscillatory femtosecond forces are probably too weak.

Hence, the strong attosecond forces could be the driving mechanism causing a crossover between the attraction and repulsion. Importantly, the ratio between the negative peak corresponding to the repulsion and the positive peak is becoming larger with increasing velocities of the electron. In such cases the dielectric response is quite weak as the electron is moving too fast and the contribution of the external field is more important. As we have discussed, the external electric field contributes positively and the negative contribution is mostly coming from the external magnetic field brought by the swift electron. If the electron was moving closer to the nanoparticle (i.e. with a smaller impact parameter), the external field would be even more dominating and higher multipole orders would have higher weights in the expansion.

It is also interesting to explore the contribution of the attosecond and femtosecond force to the total momentum transfer. The total momentum transfer can be obtained similarly as in the frequency domain by integrating the differential contributions. The integration over the time range should give the same values as we have obtained utilizing the relation (5.6). In Fig. 5.15 we plot the dependence of the mechanical momentum transfer on time (i.e. we sum the differential contributions of p_x^{mech} up to certain time plotted on x axis). It is quite clear that the transferred mechanical momentum is given mainly by the differential contributions during attoseconds.

At femtoseconds (see the inset of Fig. 5.15), we observe only quite small oscillatory variations of the transferred mechanical momentum. Value ≈ 2.2 Ns is slightly lower than the momentum transfer calculated in the frequency domain (2.4 Ns). This is probably caused especially by inaccuracies arising from the numerical surface integration. Some slight variations can also arise due to the discrete Fourier transform. As we expected, the field momentum time derivative integrated over the whole time range gives, again due

to our numerical treatment, negligible values compared to the contributions coming from the Maxwell stress tensor [see Eq. (5.1)].

For completeness, we also plot the longitudinal component of the mechanical force in Fig. 5.16. We can see that during attoseconds the particle is first pushed down to the electron and then, when the electron is closer to the sphere, it is lifted up along the direction of the electron movement. The z component of the femtosecond force oscillates with the same period as the transverse component. In the presence of the substrate, the forces we have calculated will probably be modified, and the longitudinal component would refer to possible "unsticking" from the surface.

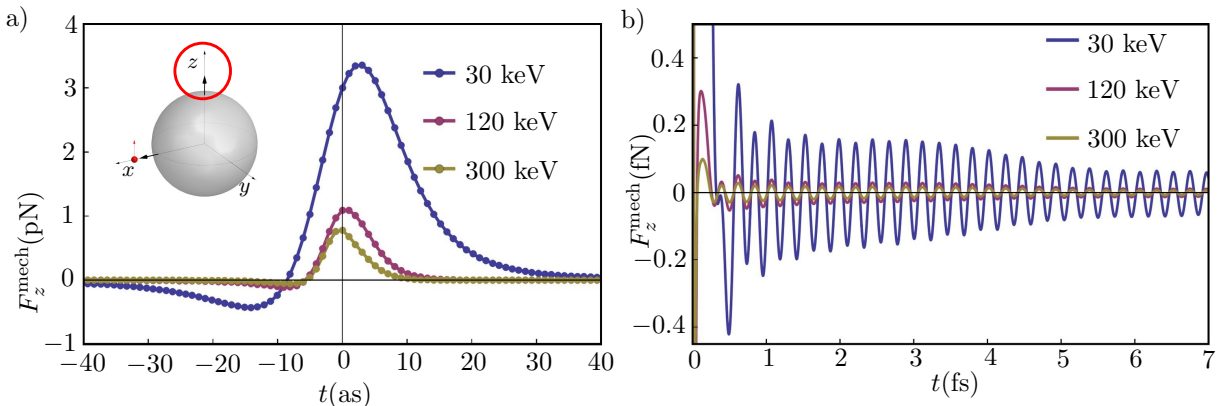


Figure 5.16: The time dependent longitudinal component of the mechanical force acting on the 1-nm aluminum nanosphere at attoseconds a) and femtoseconds b) for three different energies of the impinging electron. The impact parameter was considered to be $b = 1.5$ nm in all the cases.

5.2.2. Gold nanosphere

Now we are going to discuss the time domain force acting on the gold nanosphere characterized with previously used parameters (i.e. the dielectric function of gold modelled by the Drude model supplemented with additional Lorentz oscillators (2.9) and the parameters from tables 2.1 and 2.2), which should nicely describe the response of gold. We have considered an electron with the energy 120 keV again moving at the impact parameter $b = 1.5$ nm near the sphere with radius $a = 1$ nm and used the same approach as in the calculations related to the aluminium nanosphere.

In Fig. 5.17 we plot the resulting instantaneous mechanical force at four different time scales. In part 5.17 a) we plot the time dependence of the mechanical force together with the total and the field momentum time derivatives during attoseconds, when the electron is closely approaching the sphere. Compared to the aluminium sphere interacting with the 120 keV electron [see Fig. 5.13 a)], the total momentum time derivative has become more asymmetric now. As we were discussing, the induced magnetic field almost did not contribute and the external magnetic field was dominant in the Maxwell stress tensor (recall Fig. 5.11) in the case of the aluminium sphere, which is also confirmed for gold nanoparticle.

Hence, more pronounced asymmetry is caused by an increase of the dielectric response at higher energies and thus influencing the short-time events. Qualitatively, the induced

5.2. CALCULATION OF THE FORCE IN THE TIME DOMAIN

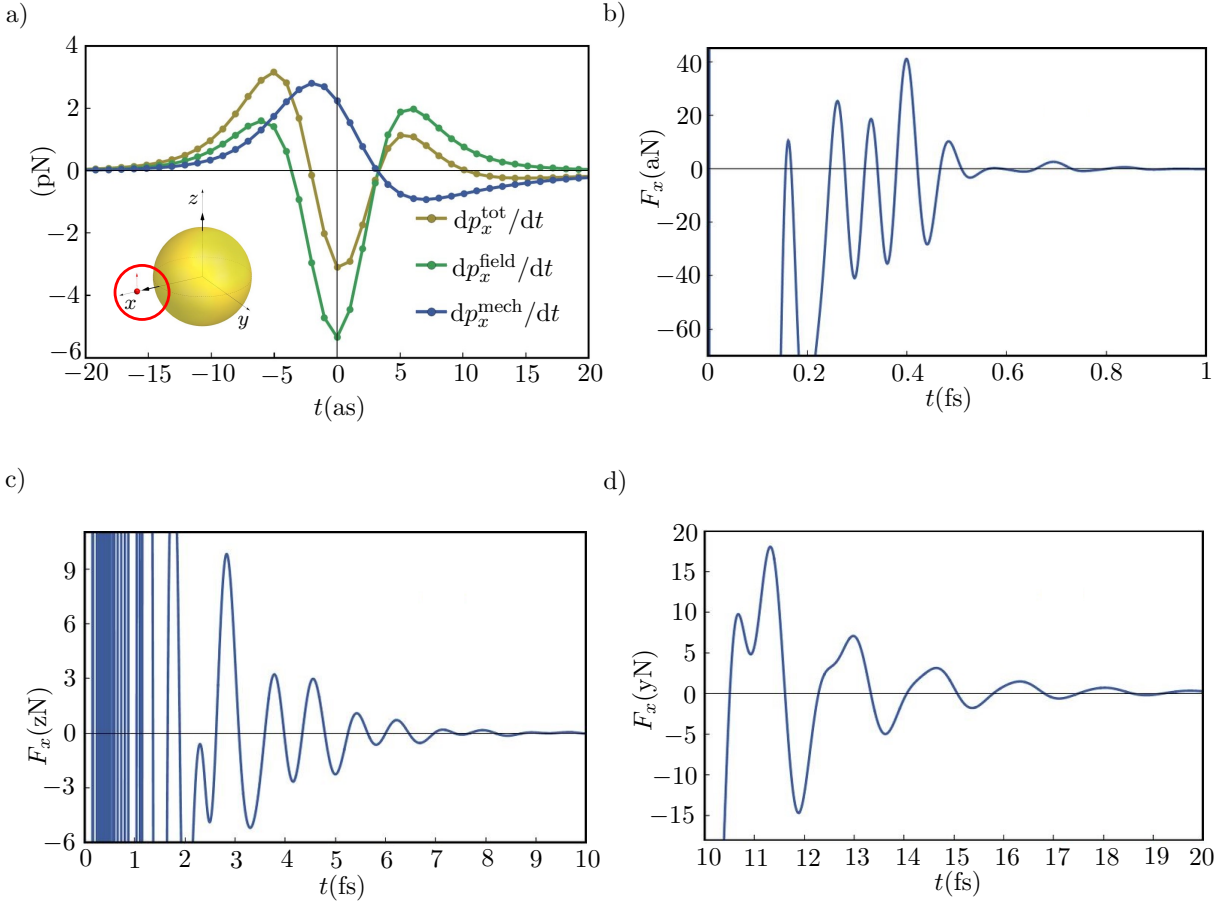


Figure 5.17: The time dependent transverse component of the mechanical force acting on the gold nanosphere with radius $a = 1$ nm due to the interaction with a 120 keV electron passing at the impact parameter $b = 1.5$ nm. At attoseconds a), together with the mechanical force, we show the total momentum and the field momentum time derivative. The transverse component of the force is shown during the transition regime b), and in different femtosecond ranges c) and d), respectively. (1 zN = $1 \cdot 10^{-21}$ N, 1 yN = $1 \cdot 10^{-24}$ N)

electric field outside the gold particle looks very similarly as in Fig. 5.8. After the subtraction of the field momentum rate of change, the mechanical force takes larger values in the transverse direction during the closest approach of the electron. Its time dependence is qualitatively similar as for aluminium: the nanosphere is first attracted towards the electron, after ≈ 3 fs the particle starts to be repelled.

In Fig. 5.17 b) we observe a transition regime between the attosecond and femtosecond times, where mostly negative force in order of tenths of attonewtons appears. A driving mechanism of this force are the oscillators modelling the influence of d -electrons and interband transitions situated at higher energies. This is also the reason why such behaviour was not observed in the case of aluminium, which was modelled only by the single Drude term.

When we have a look at the femtosecond force time dependence plotted in Fig. 5.17 c), we find out that it is damped very quickly and after ≈ 1.5 fs the force is four orders of magnitude lower than in the case of the aluminium nanosphere, which is clearly visible after comparison with Fig. 5.13 b). This is caused by higher damping in the dielectric

response and by an influence of different Lorentz oscillators. A period of the oscillations observed during the first units of femtoseconds was evaluated to be 0.75 fs, which corresponds to energy 5.51 eV. Later, an oscillator with lower energy prevails and after ≈ 10 fs we observe change of the period to 1.8 fs, which is illustrated in Fig. 5.17 d). However, it seems that more oscillators take part as the oscillations are still slightly modulated. The connection to the specific oscillator is thus not straightforward and should be further investigated.

In Fig. 5.18 we plot the transverse momentum transfer integrated up to certain time. Now, it is converged faster than for aluminium (recall Fig. 5.15) which is mainly given by the increased damping. In the smaller graph we see that the variations are negligible from times larger than a few tenths of femtosecond. We got again slightly lower value than from the frequency-domain calculation (10.0 vs. 10.2×10^{-30} Ns)

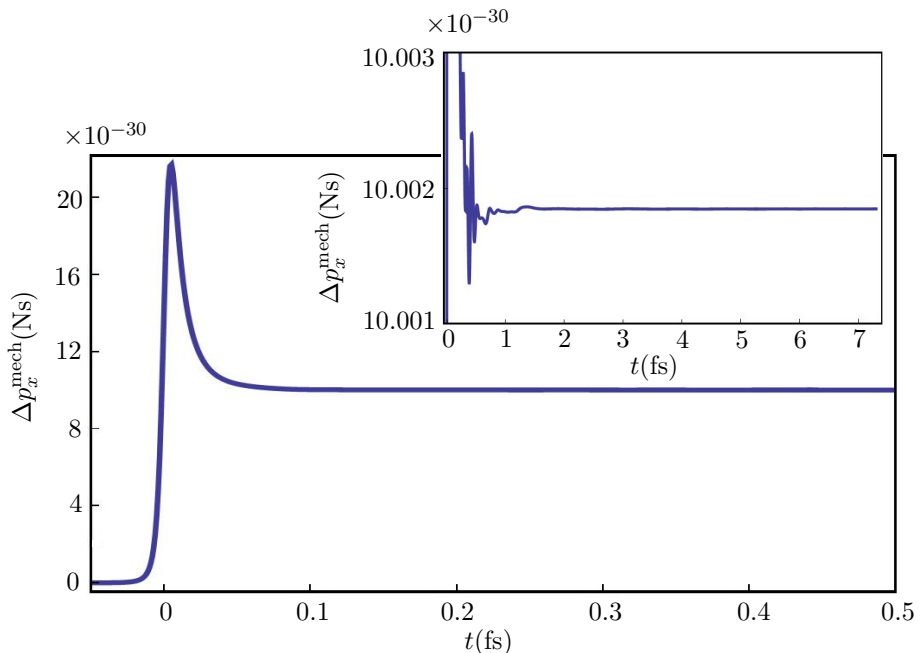


Figure 5.18: The transverse component of the mechanical momentum transfer to the gold nanosphere with radius $a = 1$ nm from the 120-keV electron passing at the impact parameter $b = 1.5$ nm.

We could notice that with both classical dielectric models we used, qualitatively similar behaviour of the force acting on the sphere was observed for attosecond times. Even using more elaborated treatment of this problem, we expect, that strong force given by the external field will always appear during the closest flyby of the electron. The attosecond induced field can differ significantly, depending on the dielectric response model.

After the integration, we obtained only positive values for the transferred mechanical momentum corresponding to the attraction with respect to the electron, but for smaller impact parameters, the repulsion can be achieved [98]. However, the justification of the classical treatment should be provided in such cases. The parameter causing the "switching" between the attraction and repulsion will be not only the impact parameter, but the nanoparticle response is also crucial as well as the impinging electron energy. Moreover, in our model we considered the sphere situated at the static position. In reality, the process is dynamic and the suggested sticking of the particle to the substrate

5.2. *CALCULATION OF THE FORCE IN THE TIME DOMAIN*

will have to be overcome. Hence, not all differential contributions will probably add to the induced motion.

The femtosecond forces attributed to the localized surface plasmon fields are oscillatory and, especially in the case of dielectric function of gold, extremely weak. When we integrated the differential contributions to the mechanical momentum in the time domain, we showed both for the aluminium and gold nanospheres that the plasmonic forces should be negligible with respect to the strong attosecond mechanical kicks.

6. Conclusions

In this diploma thesis we have dealt with the theoretical description of the fields inside and outside of a small metallic sphere induced by a fast electron passing nearby, producing a force acting on the particle. An ambiguous behaviour of the force acting on the nanoparticle has been predicted experimentally, where the particle could experience both the attraction and repulsion with respect to the electron beam, depending on the impact parameter.

First we have briefly introduced the theory of electromagnetic field, discussed the response of metals and particularly focused on possible problem which can arise when we want to describe nanostructured material. Then we have shown the formalism commonly used for description of the spectra in the electron energy loss spectroscopy, which is closely related to our problem. We have also described the boundary element method approach, which can be exploited to solve the problem of the electron energy loss for general geometry.

We continued with the previously developed approach leading to the analytical expressions of the electromagnetic field outside and inside the sphere exploiting a multipole expansion. Afterwards, we discussed a behaviour of the field in the frequency domain. A comparison of the analytical expressions with the numerical calculations based on the boundary element method has also been performed. We then evaluated and discussed both the analytically and numerically calculated EEL spectra for different parameters of the sphere and the probe.

The main part of the thesis was devoted to calculations of the momentum transfer to the spherical nanoparticle in order to provide better understanding of the experiments that were performed using the scanning transmission electron microscope [12], where the possibility to manipulate with the nanoparticles was shown. Interestingly, two different regimes of the nanoparticle movement were observed: the nanoparticles were either attracted or repelled with respect to the electron beam.

We first presented the calculations in the frequency domain for aluminium and gold nanospheres characterized by different dielectric response functions. For all the parameters we have chosen, only attraction was obtained, even for the parameters corresponding to the experiment.

However, the calculations in the frequency domain hide the underlying dynamics of the problem. In order to reveal the dynamics, the analytically calculated electromagnetic field was transformed from the frequency to the time domain as we believed it should provide better insight to the observed phenomenon. The results were discussed at two different time scales: attoseconds and femtoseconds. Attoseconds correspond to times of the closest approach of electron to the particle, when very strong external field in the nanoparticle vicinity appeared. The external field together with a weak induced field produces a strong ultra-fast mechanical "kick" very similar for both considered materials (aluminium and gold). We also observed the competition between the electric and magnetic contribution to the forces, the latter causing the repulsive behaviour. Importantly, the produced force is in order of piconewtons, which could be enough to move the particle.

During femtoseconds after the electron flyby, localized surface plasmons persist, causing the oscillatory and damped forces a few orders of magnitude lower than at attoseconds. In the case of gold, where fit of the realistic response function was used in our model, the forces were extremely weak, in order of 10^{-20} N. We believe that such a small and

furthermore oscillatory force is probably not sufficient to overcome forces between the particle and a substrate. However, an estimate of the particle adhesion has to be made.

As our calculations were made within the framework of Maxwell's equations, they cover the back-recoil effect due to a photon emission associated with the plasmon radiative decay, but not the back-recoil induced by a secondary electron emission, which could also be important [90]. In such a case, not only direction of the emission would be crucial – the particle would be consequently positively charged and a Coulombic interaction with its surroundings could change the resulting movement.

Although plethora of distinct phenomena as a thermal motion, charging of the sample, the secondary electron emission, quantum effects, non-locality or modifications of dielectric function can play some role in the results, we investigated only the influence of the electromagnetically induced forces as we believe that they could be dominant over the other mentioned effects. Hence, we propose the ultra-fast attosecond kick given by the external field to be the possible driving mechanism causing the reported nanoparticle movement. The plasmon induced forces reported in previous works [12, 16, 17] are also present, but probably too weak to overcome the adhesion forces.

Our theoretical proposals and findings, which are going to appear in our publication [98], offer opportunities for further investigation, both theoretical, dealing with different parameters and materials, and experimental towards even better explanation of the phenomena.

Appendix A: Fourier transform

The Fourier transform is a special case of integral transformation and is very important in many fields (e.g. physics, mathematics or electrotechnics). We can define the Fourier transform (FT) and the inverse Fourier transform (FT⁻¹) by expressions [99]

$$\text{FT}\{f(\mathbf{x})\} = A^N \int_{-\infty}^{\infty} \cdots \int f(\mathbf{x}) \exp(-ik\mathbf{X} \cdot \mathbf{x}) d^N \mathbf{x}, \quad (\text{A1})$$

$$\text{FT}^{-1}\{F(\mathbf{X})\} = B^N \int_{-\infty}^{\infty} \cdots \int F(\mathbf{X}) \exp(ik\mathbf{X} \cdot \mathbf{x}) d^N \mathbf{X}, \quad (\text{A2})$$

where constants A , B and k have to fulfill the condition

$$AB = \frac{|k|}{2\pi}, \quad (\text{A3})$$

In points of continuity, the functions $f(\mathbf{x}) = \text{FT}^{-1}\{F(\mathbf{X})\}$ and $F(\mathbf{X}) = \text{FT}\{f(\mathbf{x})\}$ are related via the Fourier transform.

If we want to transform a function dependent on both space variables (in E^3 space) and time variables, we employ the Fourier transform in the form

$$\text{FT}\{f(\mathbf{r}, t)\} = F(\mathbf{k}, \omega) = \iiint_{-\infty}^{\infty} f(\mathbf{r}, t) \exp[-i(\mathbf{k} \cdot \mathbf{r} - \omega t)] d^3 \mathbf{r} dt, \quad (\text{A4})$$

while its inverse transform reads

$$\text{FT}\{F(\mathbf{k}, \omega)\} = f(\mathbf{r}, t) = \left(\frac{1}{2\pi}\right)^4 \iiint_{-\infty}^{\infty} F(\mathbf{k}, \omega) \exp[i(\mathbf{k} \cdot \mathbf{r} - \omega t)] d^3 \mathbf{k} d\omega. \quad (\text{A5})$$

Properties of the Fourier transform

An extensive literature dealing with the properties of Fourier transform exists [99]. We present here a short overview of properties used in our work:

1. Relations for the Fourier transform of derivatives with respect to spatial and time variables

$$\text{FT} \left\{ \frac{\partial f(\mathbf{r}, t)}{\partial t} \right\} = -i\omega \text{FT} \{f(\mathbf{r}, t)\}, \quad \text{FT} \left\{ \frac{\partial f(\mathbf{r}, t)}{\partial x_i} \right\} = ik_i \text{FT} \{f(\mathbf{r}, t)\}. \quad (\text{A6})$$

2. The Fourier transform of a convolution is equal to product of the Fourier transforms

$$\text{FT}\{f(\mathbf{x}) \star g(\mathbf{x})\} = \frac{1}{A^N} \text{FT}\{f(\mathbf{x})\} \text{FT}\{g(\mathbf{x})\}, \quad (\text{A7})$$

where the convolution is defined via

$$f(\mathbf{x}) \star g(\mathbf{x}) = \int_{-\infty}^{\infty} \cdots \int f(\mathbf{y}) g(\mathbf{x} - \mathbf{y}) d^N \mathbf{y} \quad (\text{A8})$$

Fourier transform of real function and the Rayleigh-Parseval theorem

An important theorem states that if the Fourier integral of a function $f(\mathbf{x})$ exists, the function is real if and only if $F(\mathbf{X})$ is hermitian

$$f(\mathbf{x}) = f^*(\mathbf{x}) \iff F(\mathbf{X}) = F^*(-\mathbf{X}) \quad (\text{A9})$$

If we have two functions $f_1(\mathbf{x})$ and $f_2(\mathbf{x})$ and their Fourier transforms $F_1(\mathbf{X}) = \text{FT}\{f_1(\mathbf{x})\}$ and $F_2(\mathbf{X}) = \text{FT}\{f_2(\mathbf{x})\}$, the following equality holds:

$$A^N \int_{-\infty}^{\infty} \cdots \int f_1(\mathbf{x}) f_2^*(\mathbf{x}) d^N \mathbf{x} = B^N \int_{-\infty}^{\infty} \cdots \int F_1(\mathbf{X}) F_2^*(\mathbf{X}) d^N \mathbf{X}. \quad (\text{A10})$$

Now let us consider the special case, when $f_1(t)$ and $f_2(t)$ are real functions of time ($f_1(t) = f_1^*(t)$, $f_2(t) = f_2^*(t)$). If we substitute these functions in Eq. (A10) and use Eq. (A9), we obtain (with our particular choice of coefficients)

$$\int_{-\infty}^{\infty} f_1(t) f_2(t) dt = \frac{1}{2\pi} \int_{-\infty}^{\infty} F_1(\omega) F_2^*(\omega) d\omega = \frac{1}{\pi} \int_0^{\infty} \text{Re}[F_1(\omega) F_2^*(\omega)] d\omega. \quad (\text{A11})$$

Appendix B: Atomic units

The Hartree atomic units are chosen in a way that the following fundamental constants are equal to one atomic unit: $e = m_e = \hbar = 4\pi\epsilon_0 = 1$. In table B1 we summarize values of these quantities both in atomic and SI units. Moreover, some of the derived quantities are shown in the second part of the table.

Table B1: Selected physical quantities in atomic and SI units.

Physical quantity	Atomic units	SI units
Electron charge e	1	1.602×10^{-19} C
Electron mass m_e	1	9.109×10^{-31} kg
Reduced Planck's constant \hbar	1	1.055×10^{-34} J · s
Coulomb force constant $1/(4\pi\epsilon_0)$	1	8.988×10^9 kg · m ³ · s ⁻² · C ⁻²
Fine structure constant α	$e^2/\hbar c = 1/137$	$1/137$
Speed of light c	$1/\alpha = 137$	2.998×10^8 m · s
Bohr radius a_0	$\hbar^2/(m_e e^2) \equiv 1$ Bohr	0.529×10^{-10} m
Hartree energy E_H	$\hbar^2/(m_e a_0^2) \equiv 1$ Hartree	27.211 eV = 4.360×10^{-18} J
Atomic unit of time	$\hbar/E_H = 1$	2.419×10^{-17} s
Electric field E_0	$E_H/(ea_0) = 1$	5.142×10^{11} V · m ⁻¹

Appendix C: Multipole expansion

To express the external and induced fields arising due to the interaction of the electron and the dielectric sphere, we will start from the approach published in Ref. [18]. We first rewrite the incident external field produced by the swift electron by terms of the scalar and vector potentials in real space as

$$\mathbf{E}^{\text{ext,out}}(\mathbf{r}) = \left(\nabla - \frac{ik\mathbf{v}}{c} \right) \int G_0(\mathbf{r} - \mathbf{r}_t) \exp(i\omega t) dt, \quad (\text{C1})$$

where we introduce the Green's function of the wave equation

$$G_0(\mathbf{r} - \mathbf{r}_t) = \frac{\exp(ik|\mathbf{r} - \mathbf{r}_t|)}{|\mathbf{r} - \mathbf{r}_t|} \quad (\text{C2})$$

and where $\mathbf{r}_t = \mathbf{r}_0 + \mathbf{v}t$ is the position of the electron and $k = \omega/c$ is the magnitude of the wave vector in vacuum environment. The induced electromagnetic field can be calculated for general electron trajectory (i.e. electron passing by or crossing a sphere) [100, 101], but here we consider an external trajectory and positions \mathbf{r} , where the field is evaluated, near the surface, when $r < r_t$. The Green's function in Eq. (C2) in free space can be expanded in terms of multipoles as

$$G_0(\mathbf{r}, \mathbf{r}_t) = 4\pi k \sum_{l=0}^{\infty} \sum_{m=-l}^l j_l(kr) h_l^{(+)}(kr_t) Y_{l,m}(\Omega_{\mathbf{r}}) Y_{l,m}^*(\Omega_{\mathbf{r}_t}), \quad (\text{C3})$$

where $h_l^{(+)}(x) = ih_l^{(1)}(x)$, $h_l^{(1)}(x)$ are the spherical Hankel functions of the first kind, $(r, \Omega_{\mathbf{r}})$ and $(r_t, \Omega_{\mathbf{r}_t})$ are the spherical coordinates of \mathbf{r} and \mathbf{r}_t .

Now we can substitute Eq. (C3) into Eq. (C1) and obtain

$$\mathbf{E}^{\text{ext,out}}(\mathbf{r}) = \left(\nabla - \frac{ik\mathbf{v}}{c} \right) \sum_{n=0}^{\infty} \sum_{m=-l}^l j_l(kr) Y_{l,m}(\Omega_{\mathbf{r}}) \phi_{l,m}, \quad (\text{C4})$$

where $j_l(x)$ are the spherical Bessel functions of the first kind, $\phi_{l,m}$ are expressed as

$$\phi_{l,m} = 4\pi k \int h_l^{(+)}(kr_t) Y_{l,m}^*(\Omega_{\mathbf{r}_t}) \exp(i\omega t) dt \quad (\text{C5})$$

and the spherical harmonics $Y_{l,m}(\Omega_{\mathbf{r}})$ are defined as

$$Y_{l,m}(\theta, \phi) = \sqrt{\frac{2l+1}{4\pi} \frac{(l-m)!}{(l+m)!}} P_l^m(\cos\theta) \exp(im\phi) = \alpha_{l,m} P_l^m(\cos\theta) \exp(im\phi), \quad (\text{C6})$$

where $P_l^m(\cos\theta)$ are the associated Legendre polynomials.

It is possible to solve the integral in Eq. (C5) analytically. Now we introduce

$$M_{l,m}(\mathbf{r}_0) = \int h_l^{(+)}(k|\mathbf{r}_0 + \mathbf{v}t|) Y_{l,m}^*(\Omega_{\mathbf{r}_0 + \mathbf{v}t}) \exp(i\omega t) dt. \quad (\text{C7})$$

In our case we assumed \mathbf{v} parallel to the z axis, $\phi_0 = 0$, $z_0 = 0$ and therefore $M_{l,m}(\mathbf{r}_0)$ can be expressed as

$$M_{l,m}(\mathbf{r}_0) = M_{l,m}(b, 0, 0) \quad (\text{C8})$$

and moreover

$$M_{l,-m}(b, 0, 0) = (-1)^m M_{l,m}(b, 0, 0) \quad (\text{C9})$$

holds. For this reason we can consider $m \geq 0$. We first transform the Green's function in Eq. (C2)

$$\int \frac{\exp(i k |\mathbf{r} - (b, 0, vt)|)}{|\mathbf{r} - (b, 0, vt)|} \exp(i \omega t) dt = \frac{2}{v} K_0 \left(\frac{\omega}{v \gamma} \sqrt{(x - b)^2 + y^2} \right) \exp(i \omega z / v), \quad (\text{C10})$$

and recall Eq. (C3) to obtain

$$4\pi k \sum_{l=0}^{\infty} \sum_{m=-l}^l j_l(kr) Y_{l,m}(\Omega_{\mathbf{r}}) M_{l,m}(b, 0, 0) = \frac{2}{v} K_0 \left(\frac{\omega}{v \gamma} \sqrt{(x - b)^2 + y^2} \right) \exp(i \omega z / v). \quad (\text{C11})$$

Now we multiply both sides of Eq. (C11) by $Y_{l,m}^*(\Omega_{\mathbf{r}})$, integrate over $\Omega_{\mathbf{r}} = (\theta, \phi)$ and thanks to the orthogonality of the spherical harmonics we obtain

$$M_{l,m}(b, 0, 0) = \frac{1}{2\pi k v} \frac{1}{j_l(kr)} \int Y_{l,m}^*(\Omega_{\mathbf{r}}) K_0 \left(\frac{\omega}{v \gamma} \sqrt{(x - b)^2 + y^2} \right) \exp(i \omega z / v) d\Omega_{\mathbf{r}}. \quad (\text{C12})$$

If we further use the relationship

$$\int_{-\pi}^{\pi} \exp(-im\phi) K_0 \left(\frac{\omega}{v \gamma} \sqrt{(x - b)^2 + y^2} \right) d\phi = 2\pi I_m \left(\frac{\omega R}{v \gamma} \right) K_m \left(\frac{\omega b}{v \gamma} \right), \quad (\text{C13})$$

where $R = \sqrt{x^2 + y^2}$ and where $\exp(-im\phi)$ comes from the spherical harmonics, we can perform the integration over ϕ , and only the integral over θ remains:

$$M_{l,m}(b, 0, 0) = \frac{\alpha_{l,m}}{kv j_l(kr)} K_m \left(\frac{\omega b}{v \gamma} \right) \int_{-1}^1 I_m \left(\frac{\omega R}{v \gamma} \right) \exp(i \omega z / v) P_l^m(\mu) d\mu. \quad (\text{C14})$$

In Eq. (C14) we used the substitution $\mu = \cos(\theta)$ and the transformation from spherical to cylindrical coordinates ($R = r \sqrt{1 - \mu^2}$, $z = r\mu$). Now we take the limit $kr \rightarrow 0$, $j_l(kr) \rightarrow (kr)^l / (2l + 1)!!$, which must be compensated by the vanishing integral. Considering this limit, we use the Taylor series of the modified Bessel functions and the exponential function centered at zero:

$$I_m(\xi) = \left(\frac{1}{2} \xi \right)^m \sum_{k=0}^{\infty} \frac{\left(\frac{1}{4} \xi^2 \right)^k}{k! \Gamma(m + k + 1)} \quad \text{and} \quad \exp(\xi) = \sum_{k=0}^{\infty} \frac{\xi^k}{k!}. \quad (\text{C15})$$

These expansions can be readily substituted in the integral contained in Eq. (C14) to obtain

$$\begin{aligned}
 & \int_{-1}^1 d\mu I_m \left(\frac{\omega R}{v\gamma} \right) \exp(i\omega z/v) P_l^m(\mu) \\
 &= \int_{-1}^1 d\mu \left(\frac{1}{2} \frac{\omega \sqrt{1-\mu^2} r}{v\gamma} \right)^m \sum_{k=0}^{\infty} \frac{\left(\frac{1}{4}(1-\mu^2) \right)^k \left(\frac{\omega r}{v\gamma} \right)^{2k}}{k! \Gamma(m+k+1)} \sum_{o=0}^{\infty} \frac{\left(i\omega \frac{r}{v} \right)^o}{o!} \mu^o P_l^m(\mu) \\
 &= \int_{-1}^1 d\mu \sum_{q=0}^{\infty} \sum_{p=q}^{\infty} \left(\frac{1}{2\gamma} \right)^{m+2q} \left(\frac{\omega r}{v} \right)^{m+2q} \left(\frac{\omega r}{v} \right)^{p-q} (1-\mu^2)^{\frac{m+2q}{2}} \frac{\mu^{p-q}}{(p-q)!} \frac{i^{p-q} P_l^m(\mu)}{q! \Gamma(m+q+1)} \\
 &= \int_{-1}^1 d\mu \sum_{j=m}^{\infty} \sum_{p=\frac{j-m}{2}}^{\infty} \left(\frac{1}{2\gamma} \right)^j \left(\frac{\omega r}{v} \right)^j \left(\frac{\omega r}{v} \right)^{p-\frac{j-m}{2}} (1-\mu^2)^{\frac{j}{2}} \frac{\mu^{p-\frac{j-m}{2}}}{(p-\frac{j-m}{2})!} \frac{i^{p-\frac{j-m}{2}} P_l^m(\mu)}{\left(\frac{j-m}{2} \right)! \left(\frac{j+m}{2} \right)!} \\
 &= \int_{-1}^1 d\mu \sum_{j=m}^{\infty} \sum_{s=j}^{\infty} \left(\frac{1}{2\gamma} \right)^j \left(\frac{\omega r}{v} \right)^s (1-\mu^2)^{\frac{j}{2}} \frac{\mu^{s-j}}{(s-j)!} \frac{i^{s-j} P_l^m(\mu)}{\left(\frac{j-m}{2} \right)! \left(\frac{j+m}{2} \right)!} \\
 &= \sum_{j=m}^{\infty} \sum_{s=j}^{\infty} \left(\frac{1}{2\gamma} \right)^j \left(\frac{\omega r}{v} \right)^s \frac{i^{s-j}}{(s-j)! \left(\frac{j-m}{2} \right)! \left(\frac{j+m}{2} \right)!} \int_{-1}^1 d\mu \mu^{s-j} (1-\mu^2)^{\frac{j}{2}} P_l^m(\mu). \quad (C16)
 \end{aligned}$$

In Eq. (C16) we used rules for discrete convolution, change of variables and we also reversed the order of summation and integration. The sum over j is restricted to even $j+m$ integers. Now we label

$$I_{i_1, i_2}^{l, m} = \int_{-1}^1 \mu^{i_2} (1-\mu^2)^{\frac{i_1}{2}} P_l^m(\mu) d\mu. \quad (C17)$$

To evaluate Eq. (C17) for different l, m , we can utilize recurrence relationships for the associated Legendre polynomials

$$(l-m)P_l^m(\mu) = (2l-1)\mu P_{l-1}^m(\mu) - (l+m-1)P_{l-2}^m(\mu). \quad (C18)$$

If we insert this relation into Eq. (C17), we obtain similar relation for $I_{i_1, i_2}^{l, m}$ with index $l > m$

$$(l-m)I_{i_1, i_2}^{l, m} = (2l-1)I_{i_1, i_2+1}^{l-1, m} - (l+m-1)I_{i_1, i_2}^{l-2, m}. \quad (C19)$$

Starting values of the recurrence are

$$I_{i_1, i_2}^{m-1, m} = 0 \quad (C20)$$

and

$$I_{i_1, i_2}^{m, m} = \begin{cases} (-1)^m (2m-1)!! B \left(\frac{i_1+m+2}{2}, \frac{i_2+1}{2} \right), & \text{if } i_2 \text{ is even} \\ 0, & \text{if } i_2 \text{ is odd,} \end{cases} \quad (C21)$$

where $B(x, y)$ is the beta function. This can be derived from the starting values of recurrence related to the associated Legendre polynomials

$$P_m^m(\mu) = (-1)^m (2m-1)!! (1-\mu^2)^{m/2}, \quad (\text{C22})$$

which can be inserted into Eq. (C17):

$$I_{i_1, i_2}^{m, m} = (-1)^m (2m-1)!! \int_{-1}^1 \mu^{i_2} (1-\mu^2)^{\frac{i_1+m}{2}} d\mu. \quad (\text{C23})$$

After realizing that $B(x, y) = 2 \int_0^{\pi/2} d\theta (\sin\theta)^{2x-1} (\cos\theta)^{2y-1}$ and performing the substitution $\mu = \sin\theta$, we easily obtain Eq. (C21). We can also find out that $I_{j, s-j}^{l, m} = 0$ for $s < n$ and $j \geq m$, therefore only one summation over j is needed in (C16). The final expression for $M_{l, m}(b, 0, 0)$ then reads

$$M_{l, m}(b, 0, 0) = \int \exp(i\omega t) h_l^{(+)} [k|(b, 0, vt)|] Y_{l, m} [\Omega_{(b, 0, vt)}] dt = \frac{A_{l, m}^+}{\omega} K_m \left(\frac{\omega b}{v\gamma} \right), \quad (\text{C24})$$

where the coefficients take a form

$$A_{l, m}^+ = \frac{1}{\beta^{l+1}} \sum_{j=m}^l \frac{i^{l-j} \alpha_{l, m} (2l+1)!!}{\gamma^j 2^j (l-j)!! [(j-m)/2]!! [(j+m)/2]!!} I_{j, l-j}^{l, m}, \quad (\text{C25})$$

with a restriction of the summation for even $j+m$ integers. The expression for $\phi_{l, m}$ is also recovered:

$$\phi_{l, m} = 4\pi k \frac{A_{l, m}^+}{\omega} K_m \left(\frac{\omega b}{v\gamma} \right). \quad (\text{C26})$$

Now we introduce electric and magnetic scalar functions [31]

$$\psi^{M, \eta} = \frac{1}{L^2} \mathbf{L} \cdot \mathbf{E}^\eta \quad \psi^{E, \eta} = \frac{-ik}{L^2 \nabla^2} (\mathbf{L} \times \nabla) \cdot \mathbf{E}^\eta, \quad (\text{C27})$$

where $\mathbf{L} = -i\mathbf{r} \times \nabla$ is the orbital angular-momentum operator and superscript η can stand either for $^{\text{ext, out}}$ or $^{\text{ind, out}}$, denoting the external or induced fields outside the sphere, respectively. The fields can be reversely expressed from the scalar functions

$$\mathbf{E}^\eta = \mathbf{L} \psi^{M, \eta} - \frac{i}{k} \nabla \times \mathbf{L} \psi^{E, \eta}, \quad (\text{C28})$$

$$\mathbf{B}^\eta = -\mathbf{L} \psi^{E, \eta} - \frac{i}{k} \nabla \times \mathbf{L} \psi^{M, \eta}. \quad (\text{C29})$$

When we insert our external electric field in Eq. (C4) with Eq. (C26) into Eq. (C27) and perform some manipulation with the operators $\mathbf{L} \cdot$ and $\mathbf{L} \times \nabla$, which is outlined in [18], we find out that the scalar functions must take the form

$$\psi^{\text{M,ext,out}}(\mathbf{r}) = \sum_{n=1}^{\infty} \sum_{m=-l}^l i^l j_l(kr) Y_{l,m}(\Omega_{\mathbf{r}}) \psi_{l,m}^{\text{M,ext,out}}, \quad (\text{C30})$$

$$\psi^{\text{E,ext,out}}(\mathbf{r}) = \sum_{l=1}^{\infty} \sum_{m=-l}^l i^l j_l(kr) Y_{l,m}(\Omega_{\mathbf{r}}) \psi_{l,m}^{\text{E,ext,out}}, \quad (\text{C31})$$

with coefficients

$$\psi_{l,m}^{\text{M,ext,out}} = \frac{-4\pi i^{1-l} k v}{c^2} \frac{mA_{l,m}^+}{l(l+1)} K_m \left(\frac{\omega b}{v\gamma} \right), \quad (\text{C32})$$

$$\psi_{l,m}^{\text{E,ext,out}} = \frac{-2\pi i^{1-l} k}{c\gamma} \frac{B_{l,m}}{l(l+1)} K_m \left(\frac{\omega b}{v\gamma} \right), \quad (\text{C33})$$

where the coefficients $B_{l,m}$ are defined as

$$B_{l,m} = A_{l,m+1}^+ \sqrt{(l+m+1)(l-m)} - A_{l,m-1}^+ \sqrt{(l-m+1)(l+m)}. \quad (\text{C34})$$

We can notice that both coefficients $A_{l,m}$ and $B_{l,m}$ are dependent only on multipolar indexes and relative velocity $\beta = v/c$.

With the use of the previous expressions it is possible now to directly calculate the electric and magnetic fields by substituting the scalar functions in Eqs. (C30) and (C31) together with the expansion coefficients to Eqs. (C28) and (C29), respectively:

$$\begin{aligned} \mathbf{E}^{\text{ext,out}} &= -i\mathbf{r} \times \nabla \psi^{\text{M,ext,out}} - \frac{1}{k} \nabla \times (\mathbf{r} \times \nabla \psi^{\text{E,ext,out}}), \\ \mathbf{B}^{\text{ext,out}} &= i\mathbf{r} \times \nabla \psi^{\text{E,ext,out}} - \frac{1}{k} \nabla \times (\mathbf{r} \times \nabla \psi^{\text{M,ext,out}}). \end{aligned} \quad (\text{C35})$$

The most convenient way to compute particular components of the fields outside a spherical particle is to use the spherical coordinate system (r, θ, ϕ) as depicted in figure 4.1¹. We take $\mathbf{r} = (r, 0, 0)$, change the order of summation and differentiation and perform the required operations with vectors and operators in spherical basis:

$$\begin{aligned} \nabla \psi^{\kappa, \text{ext,out}} &= \mathbf{e}_r \sum_{l=1}^{\infty} \sum_{m=-l}^l \psi_{l,m}^{\kappa, \text{ext,out}} i^l Y_{l,m}(\theta, \phi) \frac{\partial j_l(kr)}{\partial r} \\ &+ \mathbf{e}_{\theta} \sum_{l=1}^{\infty} \sum_{m=-l}^l \psi_{l,m}^{\kappa, \text{ext,out}} \frac{1}{r} i^l j_l(kr) \frac{\partial Y_{l,m}(\theta, \phi)}{\partial \theta} \\ &+ \mathbf{e}_{\phi} \sum_{l=1}^{\infty} \sum_{m=-l}^l \psi_{l,m}^{\kappa, \text{ext,out}} \frac{1}{r \sin \theta} i^l j_l(kr) \frac{\partial Y_{l,m}(\theta, \phi)}{\partial \phi}, \end{aligned} \quad (\text{C36})$$

¹Gradient of a scalar function $f = f(r, \theta, \phi)$ in the spherical coordinates is expressed as $\nabla f = \mathbf{e}_r \frac{\partial f}{\partial r} + \mathbf{e}_{\theta} \frac{1}{r} \frac{\partial f}{\partial \theta} + \mathbf{e}_{\phi} \frac{1}{r \sin \theta} \frac{\partial f}{\partial \phi}$, curl or a vector function $\mathbf{u} = (u_r(r, \theta, \phi), u_{\theta}(r, \theta, \phi), u_{\phi}(r, \theta, \phi))$ can be computed via $\nabla \times \mathbf{u} = \mathbf{e}_r \frac{1}{r \sin \theta} \left[\frac{\partial}{\partial \theta} (u_{\phi} \sin \theta) - \frac{\partial u_{\theta}}{\partial \phi} \right] + \mathbf{e}_{\theta} \frac{1}{r} \left[\frac{1}{\sin \theta} \frac{\partial u_r}{\partial \phi} - \frac{\partial}{\partial r} (r u_{\phi}) \right] + \mathbf{e}_{\phi} \frac{1}{r} \left[\frac{\partial}{\partial r} (r u_{\theta}) - \frac{\partial u_r}{\partial \theta} \right]$.

$$\begin{aligned} \mathbf{r} \times \nabla \psi^{\kappa, \text{ext,out}} &= -\mathbf{e}_\theta \sum_{l=1}^{\infty} \sum_{m=-l}^l \psi_{l,m}^{\kappa, \text{ext,out}} \frac{1}{\sin \theta} i^l j_l(kr) \frac{\partial Y_{l,m}(\theta, \phi)}{\partial \phi} \\ &+ \mathbf{e}_\phi \sum_{l=1}^{\infty} \sum_{m=-l}^l \psi_{l,m}^{\kappa, \text{ext,out}} i^l j_l(kr) \frac{\partial Y_{l,m}(\theta, \phi)}{\partial \theta}, \end{aligned} \quad (\text{C37})$$

$$\begin{aligned} \nabla \times (\mathbf{r} \times \nabla \psi^{\kappa, \text{ext,out}}) &= \mathbf{e}_r \sum_{l=1}^{\infty} \sum_{m=-l}^l \psi_{l,m}^{\kappa, \text{ext,out}} \frac{1}{r \sin \theta} \left[\frac{\partial}{\partial \theta} \left(\sin \theta i^l j_l(kr) \frac{\partial Y_{l,m}(\theta, \phi)}{\partial \theta} \right) \right. \\ &+ \left. \frac{\partial}{\partial \phi} \left(\frac{1}{\sin \theta} i^l j_l(kr) \frac{\partial Y_{l,m}(\theta, \phi)}{\partial \phi} \right) \right] \\ &- \mathbf{e}_\theta \sum_{l=1}^{\infty} \sum_{m=-l}^l \psi_{l,m}^{\kappa, \text{ext,out}} \frac{1}{r} \left[\frac{\partial}{\partial r} \left(r i^l j_l(kr) \frac{\partial Y_{l,m}(\theta, \phi)}{\partial \theta} \right) \right] \\ &- \mathbf{e}_\phi \sum_{l=1}^{\infty} \sum_{m=-l}^l \psi_{l,m}^{\kappa, \text{ext,out}} \frac{1}{r} \left[\frac{\partial}{\partial r} \left(\frac{r}{\sin \theta} i^l j_l(kr) \frac{\partial Y_{l,m}(\theta, \phi)}{\partial \phi} \right) \right]. \end{aligned} \quad (\text{C38})$$

In the next step we have to compute the derivatives of special functions, where we use known relationships [102]:

$$\begin{aligned} \frac{\partial j_l(kr)}{\partial r} &= -k j_{l+1}(kr) + \frac{l}{r} j_l(kr), \\ \frac{\partial h_l^{(+)}(kr)}{\partial r} &= -k h_{l+1}^{(+)}(kr) + \frac{l}{r} h_l^{(+)}(kr), \\ \frac{\partial Y_{l,m}(\theta, \phi)}{\partial \theta} &= \left[\frac{(l-m+1)}{\sin \theta} \frac{\alpha_{l,m}}{\alpha_{l+1,m}} Y_{l+1,m}(\theta, \phi) - (l+1) \frac{\cos \theta}{\sin \theta} Y_{l,m}(\theta, \phi) \right], \\ \frac{\partial Y_{l,m}(\theta, \phi)}{\partial \phi} &= i m Y_{l,m}(\theta, \phi), \end{aligned} \quad (\text{C39})$$

and finally we can substitute Eqs. (C37), (C38) and (C39) together with the relationships for the coefficients into Eq. (C35) to get the external fields (4.1) and (4.2).

We analyse now the fields that are induced due to the presence of the sphere situated near electron's trajectory. If we realize that outside the sphere the fields have to be represented by outgoing waves, we can write them as

$$\psi^{\text{M,ind,out}}(\mathbf{r}) = \sum_{l=1}^{\infty} \sum_{m=-l}^l i^l h_l^{(+)}(kr) Y_{l,m}(\Omega_{\mathbf{r}}) \psi_{l,m}^{\text{M,ind,out}}, \quad (\text{C40})$$

$$\psi^{\text{E,ind,out}}(\mathbf{r}) = \sum_{l=1}^{\infty} \sum_{m=-l}^l i^l h_l^{(+)}(kr) Y_{l,m}(\Omega_{\mathbf{r}}) \psi_{l,m}^{\text{E,ind,out}}, \quad (\text{C41})$$

where the coefficients of the induced fields are connected with those for external fields via

$$\psi_{l,m}^{\text{M,ind,out}} = t_l^{\text{M}} \psi_{l,m}^{\text{M,ext,out}}, \quad (\text{C42})$$

$$\psi_{l,m}^{\text{E,ind,out}} = t_l^{\text{E}} \psi_{l,m}^{\text{E,ext,out}}. \quad (\text{C43})$$

We further apply the boundary conditions requiring continuity of ψ^{M} , $\epsilon\psi^{\text{E}}$, $\partial\psi^{\text{M}}/\partial r$ and $(1+r\partial/\partial r)\psi^{\text{E}}$ to obtain the coefficients t_l^{M} (4.5) and t_l^{E} (4.6), that are nothing but the coefficients from Mie theory [59, 103]. Then using the same procedure as in the case of the external fields, we arrive to the complete expressions for the induced fields outside the sphere (4.3) and (4.4).

We also need to find the fields inside the sphere. As we require finiteness of the fields at the origin, the electric and magnetic functions inside will be expressed with help of spherical Bessel functions as

$$\psi^{\text{M,in}}(\mathbf{r}) = \sum_{l=1}^{\infty} \sum_{m=-l}^l i^l j_l(k_{\text{in}} r) Y_{l,m}(\Omega_{\mathbf{r}}) \psi_{l,m}^{\text{M,in}}, \quad (\text{C44})$$

$$\psi^{\text{E,in}}(\mathbf{r}) = \sum_{l=1}^{\infty} \sum_{m=-l}^l i^l j_l(k_{\text{in}} r) Y_{l,m}(\Omega_{\mathbf{r}}) \psi_{l,m}^{\text{E,in}}, \quad (\text{C45})$$

where the scalar functions of the fields inside are again proportional to the external

$$\psi_{l,m}^{\text{M,in}} = s_l^{\text{M}} \psi_{l,m}^{\text{M,ext,out}}, \quad (\text{C46})$$

$$\psi_{l,m}^{\text{E,in}} = s_l^{\text{E}} \psi_{l,m}^{\text{E,ext,out}}. \quad (\text{C47})$$

s_l^{M} (4.10) and s_l^{E} (4.11) are the remaining Mie coefficients, coming from the continuity of the fields on the sphere boundary. By the same approach as in the previous two cases we can easily obtain the complete expressions for the fields inside the sphere (4.8) and (4.9).

Bibliography

- [1] KRIVANEK, O. L., CORBIN, G. J., DELLBY, N., ELSTON, B. F., KEYSE, R. J., MURFITT, M. F., OWN, C. S., SZILAGYI, Z. S., AND WOODRUFF, J. W. An electron microscope for the aberration-corrected era. *Ultramicroscopy* 108 (2008), 179–195.
- [2] KRIVANEK, O. L., LOVEJOY, T. C., DELLBY, N., AOKI, T., CARPENTER, R. W., REZ, P., SOIGNARD, E., ZHU, J., BATSON, P. E., LAGOS, M. J., EGERTON, R. F., AND CROZIER, P. A. Vibrational spectroscopy in the electron microscope. *Nature* 514, 209–212.
- [3] RUTHEMANN, G. Diskrete Energieverluste schneller Elektronen in Festkörpern. *Naturwissenschaften* 29 (1941), 648.
- [4] HILLIER, J., AND BAKER, R. F. Microanalysis by means of electrons. *Journal of Applied Physics* 15, 9 (1944), 663–675.
- [5] RITCHIE, R. H. Plasma losses by fast electrons in thin films. *Physical Review* 106 (1957), 874–881.
- [6] STERN, E. A., AND FERRELL, R. A. Surface plasma oscillations of a degenerate electron gas. *Physical Review* 120 (1960), 130–136.
- [7] MAIER, S. A. *Plasmonics: Fundamentals and Applications*, 1st ed. Springer, 2007.
- [8] PELTON, M., AIZPURUA, J., AND BRYANT, G. Metal-nanoparticle plasmonics. *Laser & Photonics Reviews* 2, 3 (2008), 136–159.
- [9] KOPIAK, M., AND STÉPHAN, O. Mapping plasmons at the nanometer scale in an electron microscope. *Chemical Society Reviews* 43 (2014), 3865–3883.
- [10] KOPIAK, M., STÉPHAN, O., GLOTER, A., ZAGONEL, L. F., TIZEI, L. H., TENCÉ, M., MARCH, K., BLAZIT, J. D., MAHFOUD, Z., LOSQUIN, A., MEURET, S., AND COLLIE, C. Seeing and measuring in colours: Electron microscopy and spectroscopies applied to nano-optics. *Comptes Rendus Physique* 15, 2–3 (2014), 158–175.
- [11] KOH, A. L., FERNÁNDEZ-DOMÍNGUEZ, A. I., McCOMB, D. W., MAIER, S. A., AND YANG, J. K. W. High-resolution mapping of electron-beam-excited plasmon modes in lithographically defined gold nanostructures. *Nano Letters* 11, 3 (2011), 1323–1330.
- [12] BATSON, P. E., REYES-CORONADO, A., BARRERA, R. G., RIVACOBA, A., ECHEIQUE, P. M., AND AIZPURUA, J. Plasmonic nanobilliards: Controlling nanoparticle movement using forces induced by swift electrons. *Nano Letters* 11, 8 (2011), 3388–3393.
- [13] CRETU, O., RODRÍGUEZ-MANZO, J., DEMORTIÈRE, A., AND BANHART, F. Electron beam-induced formation and displacement of metal clusters on graphene, carbon nanotubes and amorphous carbon. *Carbon* 50, 1 (2012), 259–264.

BIBLIOGRAPHY

- [14] ZHENG, H., MIRSAIDOV, U. M., WANG, L.-W., AND MATSUDAIRA, P. Electron beam manipulation of nanoparticles. *Nano Letters* 12, 11 (2012), 5644–5648.
- [15] ZHENG, H. Using molecular tweezers to move and image nanoparticles. *Nanoscale* 5 (2013), 4070–4078.
- [16] REYES-CORONADO, A., BARRERA, R. G., BATSON, P. E., ECHEIQUE, P. M., RIVACOBA, A., AND AIZPURUA, J. Electromagnetic forces on plasmonic nanoparticles induced by fast electron beams. *Physical Review B* 82 (2010), 235429.
- [17] GARCÍA DE ABAJO, F. J. Momentum transfer to small particles by passing electron beams. *Physical Review B* 70 (2004), 115422.
- [18] GARCÍA DE ABAJO, F. J. Relativistic energy loss and induced photon emission in the interaction of a dielectric sphere with an external electron beam. *Physical Review B* 59, 4 (1999), 3095–3107.
- [19] JACKSON, J. D. *Classical Electrodynamics*, 3rd ed. John Wiley & Sons, New York, 1998.
- [20] STRATTON, J. A. *Electromagnetic Theory*. McGraw-Hill, New York, 1941.
- [21] LORENTZ, H. A. *The theory of electrons and its applications to the phenomena of light and radiant heat*. Teubner, Leipzig, 1909.
- [22] NOVOTNY, L., AND HECHT, B. *Principles of Nano-Optics*. Cambridge University Press, 2006.
- [23] LEONHARDT, U. Momentum in an uncertain light. *Nature* 444 (2006), 823–824.
- [24] MANSURIPUR, M. Momentum exchange effect. *Nature Photonics* 7 (2013), 765–766.
- [25] BREVIK, I. Experiments in phenomenological electrodynamics and electromagnetic energy-momentum tensor. *Physics Reports* (1979), 133–201.
- [26] PFEIFER, R. N. C., NIEMINEN, T. A., HECKENBERG, N. R., AND RUBINSZTEIN-DUNLOP, H. *Colloquium: Momentum of an electromagnetic wave in dielectric media*. *Review of Modern Physics* 79 (2007), 1197–1216.
- [27] BARNETT, S. M., AND LOUDON, R. On the electromagnetic force on a dielectric medium. *Journal of Physics B: Atomic, Molecular and Optical Physics* 39, 15 (2006), S671.
- [28] BARNETT, S. M., AND LOUDON, R. The enigma of optical momentum in a medium. *Philosophical Transactions of the Royal Society of London A: Mathematical, Physical and Engineering Sciences* 368, 1914 (2010), 927–939.
- [29] MANSURIPUR, M. Resolution of the Abraham–Minkowski controversy. *Journal of Physics B: Atomic, Molecular and Optical Physics* 39, 10 (2010), 1997–2005.
- [30] MANSURIPUR, M. Radiation pressure and the linear momentum of the electromagnetic field. *Optics Express* 12, 22 (2004), 5375–5401.

BIBLIOGRAPHY

- [31] LOW, F. E. *Classical Field Theory: Electromagnetism and Gravitation*. John Wiley & Sons, New York, 1997.
- [32] DRUDE, P. Zur Elektronentheorie der Metalle. *Annalen der Physik* 306 (1900), 566–613.
- [33] DRUDE, P. Zur Elektronentheorie der Metalle; II. Teil. Galvanomagnetische und thermomagnetische Effecte. *Annalen der Physik* 308 (1900), 369–402.
- [34] SOMMERFELD, A., AND BETHE, H. *Elektronentheorie der Metalle*. 1933.
- [35] MORUZZI, V. L., JANAK, J. F., AND WILLIAMS, A. R. *Calculated electronic properties of metals*, 3 ed. Pergamon, Oxford, 1978.
- [36] ROMANELLO, P., AND DE BOEIJ, P. L. The role of relativity in the optical response of gold within the time-dependent current-density-functional theory. *The Journal of Chemical Physics* 122, 16 (2005), 164303.
- [37] KREIBIG, U., AND VOLLMER, M., Eds. *Optical Properties of Metal Clusters*. Springer, Berlin Heidelberg, 1995.
- [38] HE, Y., AND ZENG, T. First-principles study and model of dielectric functions of silver nanoparticles. *The Journal of Physical Chemistry C* 114, 42 (2010), 18023–18030.
- [39] IDROBO, J. C., WALKOSZ, W., YIP, S. F., ÖĞÜT, S., WANG, J., AND JELLINEK, J. Static polarizabilities and optical absorption spectra of gold clusters (Au_n , $n = 2 – 14$ and 20) from first principles. *Physical Review B* 76 (2007), 205422.
- [40] IIDA, K., NODA, M., ISHIMURA, K., AND NOBUSADA, K. First-principles computational visualization of localized surface plasmon resonance in gold nanoclusters. *The Journal of Physical Chemistry C* 118, 47 (2014), 11317–11322.
- [41] GARCÍA DE ABAJO, F. J. Nonlocal effects in the plasmons of strongly interacting nanoparticles, dimers, and waveguides. *The Journal of Physical Chemistry C* 112, 46 (2008), 17983–17987.
- [42] DAVID, C., AND GARCÍA DE ABAJO, F. J. Spatial nonlocality in the optical response of metal nanoparticles. *The Journal of Physical Chemistry C* 115, 40 (2011), 19470–19475.
- [43] TOWNSEND, E., AND BRYANT, G. W. Plasmonic properties of metallic nanoparticles: The effects of size quantization. *Nano Letters* 12, 1 (2012), 429–434.
- [44] ESTEBAN, R., BORISOV, A. G., NORDLANDER, P., AND AIZPURUA, J. Bridging quantum and classical plasmonics with a quantum-corrected model. *Nature Communications*, 825 (2012).
- [45] SCHOLL, J. A., KOH, A. L., AND DIONNE, J. A. Quantum plasmon resonances of individual metallic nanoparticles. *Nature* 483 (2012), 421–428.

BIBLIOGRAPHY

- [46] SCHOLL, J. A., GARCÍA-ETXARRI, A., KOH, A. L., AND DIONNE, J. A. Observation of quantum tunneling between two plasmonic nanoparticles. *Nano Letters* 13, 2 (2013), 564–569.
- [47] RAZA, S., STENGER, N., KADKHODAZADEH, S., FISCHER, S. V., KOSTESHA, N., JAUHO, A.-P., BURROWS, A., WUBS, M., , AND MORTENSEN, N. A. Blueshift of the surface plasmon resonance in silver nanoparticles studied with EELS. *Nanophotonics* 2 (2013), 131–138.
- [48] ASHCROFT, N. W., AND MERMIN, D. N. *Solid state physics*, 1st ed. Thomson Learning, Toronto, 1976.
- [49] PALIK, E. D. *Handbook of Optical Constants of Solids*. Academic Press, New York, 1985.
- [50] EHRENREICH, H., PHILIPP, H. R., AND SEGALL, B. Optical properties of aluminum. *Physical Review* 132 (1963), 1918–1928.
- [51] HOHENESTER, U., AND TRÜGLER, A. MNPBEM: A Matlab toolbox for the simulation of plasmonic nanoparticles. *Computer Physics Communications* 183, 2 (2012), 370–381.
- [52] FOX, M. *Optical Properties of Solids*. OUP, Oxford, 2010.
- [53] RAKIĆ, A. D., DJURIŠIĆ, A. B., ELAZAR, J. M., AND MAJEWSKI, M. L. Optical properties of metallic films for vertical-cavity optoelectronic devices. *Applied Optics* 37, 22 (1998), 5271–5283.
- [54] ETCHEGOIN, P. G., LE RU, E. C., AND MEYER, M. An analytic model for the optical properties of gold. *The Journal of Chemical Physics* 125, 16 (2006), 164705.
- [55] BRENDEL, R., AND BORMANN, D. An infrared dielectric function model for amorphous solids. *Journal of Applied Physics* 71, 1 (1992).
- [56] MATLAB. <http://www.mathworks.com>. Accessed: 2014-06-12.
- [57] Mathematica. <http://www.wolfram.com/mathematica/?source=nav>. Accessed: 2015-2-23.
- [58] BARCHIESI, D., AND GROSGES, T. Fitting the optical constants of gold, silver, chromium, titanium, and aluminum in the visible bandwidth. *Journal of Nanophotonics* 8, 1 (2014), 083097.
- [59] BOHREN, C. F., AND HUFFMAN, D. R. *Absorption and Scattering of Light by Small Particles*. Wiley-VCH, 1998.
- [60] QUINTEN, M. *Optical properties of nanoparticle systems*. Wiley-VCH, Weinheim, 2011.
- [61] CHRISTENSEN, T., YAN, W., RAZA, S., JAUHO, A.-P., MORTENSEN, N. A., AND WUBS, M. Nonlocal response of metallic nanospheres probed by light, electrons, and atoms. *ACS Nano* 8, 2 (2014), 1745.

BIBLIOGRAPHY

- [62] LIEBSCH, A. Surface-plasmon dispersion and size dependence of mie resonance: Silver versus simple metals. *Physical Review B* 48, 15 (1993), 11317–11328.
- [63] MERMIN, N. D. Lindhard dielectric function in the relaxation-time approximation. *Physical Review B* 1 (1970), 2362–2363.
- [64] RAZA, S., TOSCANO, G., JAUHO, A.-P., WUBS, M., AND MORTENSEN, N. A. Unusual resonances in nanoplasmonic structures due to nonlocal response. *Physical Review B* 84 (2011), 121412.
- [65] MORTENSEN, N. A. Nonlocal formalism for nanoplasmonics: Phenomenological and semi-classical considerations. *Photonics and Nanostructures - Fundamentals and Applications* 11, 4 (2013), 303–309.
- [66] STELLA, L., ZHANG, P., GARCÍA-VIDAL, F. J., RUBIO, A., AND GARCÍA-GONZÁLEZ, P. Performance of nonlocal optics when applied to plasmonic nanostructures. *The Journal of Physical Chemistry C* 117, 17 (2013), 8941–8949.
- [67] RUPPIN, R. Optical properties of small metal spheres. *Physical Review B* 11, 8 (1975), 2871–2876.
- [68] LINDHARD, J. On the properties of a gas of charged particles. *Matematisk-fysiske Meddelelser* 28, 8 (1954).
- [69] FUCHS, R., AND CLARO, F. Multipolar response of small metallic spheres: Non-local theory. *Physical Review B* 35, 8 (1987), 3722–3727.
- [70] RUPPIN, R. Optical properties of a plasma sphere. *Physical Review Letters* 31, 24 (1973), 1434.
- [71] MORTENSEN, N. A., RAZA, S., WUBS, M., SØNDERGAARD, T., AND BOZHEVOLNYI, S. I. A generalized non-local optical response theory for plasmonic nanostructures. *Nature Communications*, 3809 (2014).
- [72] GARCÍA DE ABAJO, F. J. Optical excitations in electron microscopy. *Reviews of Modern Physics* 82, 1 (2010), 209–275.
- [73] EGERTON, R. F. *Electron Energy-Loss Spectroscopy in the Electron Microscope*, 3 ed. Springer, New York, 2011.
- [74] GINZBURG, V. L. Radiation by uniformly moving sources (Vavilov-Cherenkov effect, transition radiation, and other phenomena). *Physics Uspekhi* 39, 10 (1996), 973–982.
- [75] FERMI, E. The ionization loss of energy in gases and in condensed materials. *Physical Review* 57 (1940), 485–493.
- [76] RIVACOBA, A., ZABALA, N., AND AIZPURUA, J. Image potential in scanning transmission electron microscopy. *Progress in Surface Science* 65, 1–2 (2000), 1–64.
- [77] LUCAS, A. A., AND ŠUNJIĆ, M. Fast-electron spectroscopy of surface excitations. *Physical Review Letters* 26 (1971), 229–232.

BIBLIOGRAPHY

- [78] ECHEIQUE, P. M., AND PENDRY, J. B. Absorption profile at surfaces. *Journal of Physics C* 8 (1975), 2936–2942.
- [79] GARCÍA-MOLINA, R., GRAS-MARTI, A., HOWIE, A., AND RITCHIE, R. H. Retardation effects in the interaction of charged particle beams with bounded condensed media. *Journal of Physics C: Solid State Physics* 18, 27 (1985), 5335–5345.
- [80] ENOCH, S., AND BONOD, N., Eds. *Plasmonics*. Springer-Verlag, Berlin Heidelberg, 2012.
- [81] FERRELL, T. L., AND ECHEIQUE, P. M. Generation of surface excitations on dielectric spheres by an external electron beam. *Physical Review Letters* 55 (1985), 1526–1529.
- [82] GARCÍA DE ABAJO, F. J., AND HOWIE, A. Relativistic electron energy loss and electron-induced photon emission in inhomogeneous dielectrics. *Physical Review Letters* 80, 23 (1998), 5180–5183.
- [83] GARCÍA DE ABAJO, F. J., AND AIZPURUA, J. Numerical simulation of electron energy loss near inhomogeneous dielectrics. *Physical Review B* 56, 24 (1997), 15873–15884.
- [84] GARCÍA DE ABAJO, F. J., AND HOWIE, A. Retarded field calculation of electron energy loss in inhomogeneous dielectrics. *Physical Review B* 65, 11 (2002), 115418.
- [85] NELAYAH, J., KOCIAK, M., STÉPHAN, O., GARCÍA DE ABAJO, F. J., TENCE, M., HENRARD, L., TAVERNA, D., PASTORIZA-SANTOS, I., LIZ-MARZÁN, L. M., AND COLLIEX, C. Mapping surface plasmons on a single metallic nanoparticle. *Nature Physics* 3, 5 (2007), 348–353.
- [86] ZHOU, X., HÖRL, A., TRÜGLER, A., HOHENESTER, U., NORRIS, T. B., AND HERZING, A. A. Effect of multipole excitations in electron energy-loss spectroscopy of surface plasmon modes in silver nanowires. *Journal of Applied Physics* 116 (2014), 223101.
- [87] HOHENESTER, U. Simulating electron energy loss spectroscopy with the MNPBEM toolbox. *Computer Physics Communications* 185, 3 (2014), 1177–1187.
- [88] RIVACOBA, A., AND ECHEIQUE, P. M. Deflection of STEM electrons by dielectric spheres. *Ultramicroscopy* 26 (1988), 389.
- [89] GUTURBAY, I. G., PITARKE, J. M., CAMPILLO, I., AND RUBIO, A. Dynamic structure factor of gold. *Computational Materials Science* 22 (2001), 123–128.
- [90] HOWIE, A. Addressing coulomb's singularity, nanoparticle recoil and johnson's noise. *Journal of Physics: Conference Series* 522, 1 (2014), 012001.
- [91] ARIAS-GONZÁLEZ, J. R., AND NIETO-VESPERINAS, M. Optical forces on small particles: attractive and repulsive nature and plasmon-resonance conditions. *Journal of the Optical Society of America* 20, 7 (2003), 1201–1209.

BIBLIOGRAPHY

- [92] HONGXING, X., AND KÄLL, M. Surface-plasmon-enhanced optical forces in silver nanoaggregates. *Physical Review Letters* 89 (2002), 246802.
- [93] ROXWORTHY, B. J., BHUIYA, A. M., YU, X., CHOW, E. K. C., AND TOUS-SAINT JR, K. C. Reconfigurable nanoantennas using electron-beam manipulation. *Nature Communications* 5, 4427 (2014).
- [94] MILJKOVIĆ, V. D., PAKIZEH, T., SEPULVEDA, B., JOHANSSON, P., AND KÄLL, M. Optical forces in plasmonic nanoparticle dimers. *Journal of Physical Chemistry C* 114 (2010), 7472–7479.
- [95] RIVACOBA, A., AND ZABALA, N. Relativistic force between fast electrons and planar targets. *New Journal of Physics* 16, 7 (2014), 073048.
- [96] BARBRY, M., KOVAL, P., MARCHESIN, F., ESTEBAN, R., BORISOV, A. G., AIZPURUA, J., AND SÁNCHEZ-PORTAL, D. Atomistic near-field nanoplasmonics: Reaching atomic-scale resolution in nanooptics. *Nano Letters* 15, 5 (2015), 3410–3419.
- [97] Wolfram documentation center: Discrete fourier transforms. <http://reference.wolfram.com/language/tutorial/FourierTransforms.html>. Accessed: 2015-4-28.
- [98] LAGOS, M. J., REYES-CORONADO, A., KONEČNÁ, A., ECHEIQUE, P. M., AIZPURUA, J., AND BATSON, P. E. Attosecond and femtosecond forces exerted on gold nanoparticles induced by relativistic electrons. In preparation.
- [99] KOMRSKA, J. *Fourierovské metody v teorii difrakce a ve strukturní analýze*. VUTIUM, Brno, 2001.
- [100] MORSE, P. M., AND FESHBACH, H. *Methods of Theoretical Physics*. McGraw-Hill, 1953.
- [101] AIZPURUA, J. *Coupling of electrons and electromagnetic surface modes in scanning transmission electron microscopy*. PhD thesis, Euskal Herriko Unibersitatea, 1998.
- [102] ABRAMOWITZ, M., AND STEGUN, I. A. *Handbook of Mathematical Functions with Formulas, Graphs, and Mathematical Tables*. Dover, New York, 1964.
- [103] MIE, G. Beiträge zur Optik trüber Medien, speziell kolloidaler Metallösungen. *Annalen der Physik* 330, 3 (1908), 377–445.